ABSTRACT

ANALYSIS AND CHARACTERIZATION OF THE INTEGRATED DIELECTRIC SLAB WAVEGUIDE-WEDGE ANTENNA USING ITERATIVE MODE-MATCHING TECHNIQUE

by
Chairat Pinthong

A rigorous solution for the TE and TM polarization to the dielectric wedge antenna fed by a slab waveguide of the same material is presented. The method of solution involves modeling the wedge as a sequence of step discontinuities and using an iterative procedure to track forward and backward partial wave fields, expressed as modal expansions, to obtain the rigorous field solution. Radiation patterns of directive gain are presented. All patterns smoothly decrease from a maximum in the endfire direction and exhibit very low side lobes. Longer length wedges are shown to produce higher directivity and smaller half-power beamwidths (HPBW). For TE polarization, wedges with larger values of dielectric constant yield smaller directivity and broader HPBW. In contrast, for TM polarization, wedges with larger values of dielectric constant have essentially same directivity and HPBW as wedges of smaller dielectric constant material. For TE or TM polarization, slender, gradually tapered wedges, yield a reflection coefficient of the guided surface wave on the feed guide at the base of the antenna that is very small. This indicates that tapered dielectric antennas produce low VSWR values. In addition, there appears to be no gain limitation with antenna length for these antennas. Frequency characteristics are examined to show that the dielectric wedge antenna is a broadband antenna. The method of solution is general and can be applied to a broad class of dielectric antennas having different geometries.

ANALYSIS AND CHARACTERIZATION OF THE INTEGRATED DIELECTRIC SLAB WAVEGUIDE-WEDGE ANTENNA USING ITERATIVE MODE-MATCHING TECHNIQUE

by
Chairat Pinthong

A Dissertation
Submitted to the Faculty of
New Jersey Institute of Technology
in Partial Fulfillment of the Requirements for the Degree of
Doctor of Philosophy in Electrical Engineering

Department of Electrical and Computer Engineering

May 2005

APPROVAL PAGE

ANALYSIS AND CHARACTERIZATION OF THE INTEGRATED DIELECTRIC SLAB WAVEGUIDE-WEDGE ANTENNA USING ITERATIVE MODE-MATCHING TECHNIQUE

Chairat Pinthong

Dr. Gerald M. Whitman, Dissertation Advisor — Date
Professor of Electrical and Computer Engineering, NJIT

Dr. Edip Niver, Committee Member — Date
Associate Professor of Electrical and Computer Engineering, NJIT

Dr. Ali Abdi, Committee Member — Date
Assistant Professor of Electrical and Computer Engineering, NJIT

Dr. Gregory A. Kriegsmann, Committee Member — Date
Professor of Mathematical Sciences, NJIT

Dr. Peter G. Petropoulos, Committee Member — Date
Associate Professor of Mathematical Sciences, NJIT

Dr. Felix K. Schwering, Committee Member — Date
Chief Scientist, U.S. Army CECOM, retired

BIOGRAPHICAL SKETCH

Author: Chairat Pinthong

Degree: Doctor of Philosophy

Date: May 2005

Undergraduate and Graduate Education:

- Doctor of Philosophy in Electrical Engineering,
  New Jersey Institute of Technology, Newark, NJ, 2005
- Master of Engineering in Electrical Engineering,
  Chulalongkorn University, Bangkok, Thailand, 1997
- Bachelor of Engineering in Electrical Engineering,
  Chiang Mai University, Chiang Mai, Thailand, 1992

Major: Electrical Engineering

Presentations and Publications:

Gerald M. Whitman, Chairat Pinthong, Anthony A. Triolo, and Felix Schwering, "An Approximate but Accurate Analysis of the Dielectric Wedge Antenna Fed by a Slab Waveguide Using the Local Mode Theory and Schelkunoff Equivalence Principle," IEEE Transactions on Antennas and Propagation, accepted for publication on March 2005.

Gerald M. Whitman, Chairat Pinthong, Wan-Yu Chen, and Felix Schwering, "Rigorous TE Solution to the Dielectric Wedge Antenna Fed by a Slab Waveguide," IEEE Transactions on Antennas and Propagation, accepted for publication on March 2005.

Gerald M. Whitman, Chairat Pinthong, Wan-Yu Chen, and Felix K. Schwering,
"Rigorous TM Solution to the Dielectric Wedge Antenna Fed by a Slab Waveguide," IEEE International Symposium on Antennas and Propagation and USNC/URSI National Radio Science Meeting, Washington, DC, July 2005, accepted for publication on March 2005.

Chairat Pinthong, Gerald Whitman, and Felix Schwering,
"Rigorous Mode Matching Solution to the Dielectric Wedge Antenna Fed by a Slab Waveguide," NCE Graduate Research Poster Session, NJIT, Newark, NJ, April 2004.

To the memory of my grandfather and my grandmother,
Singto and Kaewmul Pinthong

To my beloved family

ACKNOWLEDGMENT

The preparation of this dissertation was assisted by many people who I gained knowledge, insight and experience. I would like to express my deepest gratitude to Dr. Gerald M. Whitman, my advisor, who has provided valuable guidance of science and life. I am deeply indebted to Dr. Felix K. Schwering for his suggestions in this research. My gratitude is expressed to Dr. Edip Niver, Dr. Ali Abdi, Dr. Gregory A. Kriegsmann and Dr. Peter G. Petropoulos for serving as dissertation committee members, and for providing useful comments. The concerns and help provided by Dr. Ronald S. Kane, the Dean of Graduate Studies, are always appreciated.

I am gratefully acknowledge the assistance of Dr. Methi Wecharatana, a professor of Civil and Environmental Engineering, who introduced me to NJIT under the support of the Memorandum of Understanding between Ministry of University Affairs, Kingdom of Thailand and New Jersey Institute of Technology, the United States of America.

Fellow graduate students in the Center of Microwave and Lightwave Engineering, Michael Wu, Ozgur Ozdemir, and former students at the laboratory, Dr. Keehong Um and Wan-Yu Chen, are deserving of recognition for their help and discussions.

For their sympathetic interest, I wish to thank my relatives, Somchai Kulwatdanaporn, M.D., Samornrat Kulwatdanaporn, Sirichai Venin, Suchitta Kasornboobpa, a student at Kean University-Srikittima Pun-Atit, and former students at NJIT-Jittiphan Pijchig and Peerajak Witoonchart.

I wish to thank my family members: my father, Soonthon Pinthong, my mother Pranee Manobang, my uncles, Sombut Boonyaprapa, M.D., Bandit and Suriyan Pinthong, my aunts, Wilai Boonyaprapa and Chomsri Pinthong, my brother, Chairot Pinthong, my cousins, Sakol and Prasertsak Boonyaprapa and my wife, Wanphen Pinthong (Thepwong), for their boundless love, extraordinary patience and encouragement. Finally, for their desire to inculcate the wealth of knowledge, I am eternally grateful to my grandfather and my grandmother, Singto and Kaewmul Pinthong.

TABLE OF CONTENTS

TABLE OF CONTENTS
(Continued)

Chapter **Page**

LIST OF TABLES

LIST OF TABLES
(Continued)

LIST OF FIGURES

LIST OF FIGURES
(Continued)

Figure **Page**

LIST OF FIGURES
(Continued)

Figure **Page**

LIST OF FIGURES
(Continued)

Figure **Page**

LIST OF FIGURES
(Continued)

Figure **Page**

LIST OF FIGURES
(Continued)

Figure **Page**

LIST OF FIGURES
(Continued)

Figure **Page**

LIST OF SYMBOLS

$A_{i,n}^{f,p}$	Amplitude of the n^{th}-order surface wave mode incident upon step transition plane S_i for the p^{th} forward progression
$A_i^{f,p}(u)$	Amplitude of radiation modes incident upon step transition plane S_i for the p^{th} forward progression
b,p	The p^{th} backward progression
$B_{i,n}^{b,p}$	Amplitude of the n^{th}-order surface wave mode incident upon step transition plane S_i for the p^{th} backward progression
$B_i^{b,p}(u)$	Amplitude of radiation modes incident upon step transition plane S_i for the p^{th} backward progression
CFBEM	Combination of the finite-element and boundary element methods
$D(\theta)$	Directive gain
D_i	Slab half width
$D_{\max}$	Directivity
$E_{j,i}^{b,p}$	The j-component of electric field intensity in region i for p^{th} backward progression
$E_{j,i}^{f,p}$	The j-component of electric field intensity in region i for p^{th} forward progression
f,p	The p^{th} forward progression
$G_N(\theta)$	Normalized gain
HPBW	Half-power beamwidth
$H_{j,i}^{b,p}$	The j-component of magnetic field intensity in region i for p^{th} backward progression

$H_{j,i}^{f,p}$	The j-component of magnetic field intensity in region i for p^{th} forward progression
$i_{i,n}(z)$	Expansion coefficient of the n^{th}-order surface wave mode in region i
$i_i(z,u)$	Expansion coefficient of radiation modes in region i
k	Wavenumber of slab material
k_0	Free space wavenumber
L	Wedge length
L_F	Feed taper length of the antenna with Zucker's profile
L_T	Terminal taper length of the antenna with Zucker's profile
L_U	Uniform section length of the antenna with Zucker's profile
M	Number of regions in staircase model of the antenna
M_S	Number of step transition planes in staircase model of the antenna
N	Number of segments of length Δu in the range of radiation modes
N_b	Number of backward progressions
N_E	Number of segments in the range of evanescent radiation modes
N_f	Number of forward progressions
n_i	Refractive index of slab of medium i
N_m	Number of modes considered at each step discontinuity
N_P	Number of segments in the range of propagating radiation modes
N_S	Numbers of finite slab segments in staircase model of the antenna
N_E^I	Number of intervals in the range of evanescent radiation modes

N_m^{TE}	The highest order of the TE surface wave mode
N_m^{TM}	The highest order of the TM surface wave mode
N_P^I	Number of intervals in the range of propagating radiation modes
N_T^I	Number of intervals in the range of radiation modes
P_{inc}	Incident power of surface wave mode
P^{RAD}	Radiated power
P_{ref}^G	Reflected guided-mode power
P_{trans}^G	Transmitted guided-mode power
P_{ref}^{RAD}	Reflected radiated-mode power
P_{trans}^{RAD}	Transmitted radiated-mode power
$R_{i,n}^{b,p}$	Amplitude of the n^{th}-order reflected surface wave mode scattering at step transition plane S_i for the p^{th} backward progression
$R_{i,n}^{f,p}$	Amplitude of the n^{th}-order reflected surface wave mode scattering at step transition plane S_i for the p^{th} forward progression
$R_i^{b,p}(u)$	Amplitude of reflected radiation modes scattering at step transition plane S_i for the p^{th} backward progression
$R_i^{f,p}(u)$	Amplitude of reflected radiation modes scattering at step transition plane S_i for the p^{th} forward progression
SLL	Side lobe level
S_i	Step transition plane with identification i
$T_{i,n}^{b,p}$	Amplitude of the n^{th}-order transmitted surface wave mode scattering at step transition plane S_i for the p^{th} backward progression

$T_{i,n}^{f,p}$	Amplitude of the n^{th}-order transmitted surface wave mode scattering at step transition plane S_i for the p^{th} forward progression
$T_i^{b,p}(u)$	Amplitude of transmitted radiation modes scattering at step transition plane S_i for the p^{th} backward progression
$T_i^{f,p}(u)$	Amplitude of transmitted radiation modes scattering at step transition plane S_i for the p^{th} forward progression
$U(\theta)$	Radiation intensity
U_{ave}	Average radiation intensity
VSWR	Voltage standing wave ratio
$v_{i,n}(z)$	Expansion coefficient of the n^{th}-order surface wave mode in region i
$v_i(z,u)$	Expansion coefficient of radiation modes in region i
z_i	Location of the step transition plane S_i
$\beta_{i,n}$	Propagation constant of n^{th}-order surface wave mode in slab of region i
$\beta(u)$	Propagation constant of radiation modes
δ_{mn}	Kronecker delta symbol
$\delta(u)$	Dirac delta function
Δz	Slab segment length
ε_0	Permittivity of free space
$\varepsilon_{r,i}(x)$	Relative permittivity of region i
η_0	Free space wave impedance
Γ	Reflection coefficient of the surface wave at the input of antenna
Γ^b	Reflection coefficient for the surface wave incident from the right to a step discontinuity plane

Γ^f	Reflection coefficient for surface wave incident from the left to a step discontinuity plane
λ_0	Free space wavelength
λ_c	Wavelength at center angular frequency ω_c
μ_0	Permeability of free space
ω	Angular frequency
ω_c	Center angular frequency
$\Phi_{i,n}(x)$	The n^{th}-order TE surface wave mode function in region i
$\Phi_i(x,u)$	TE radiation mode function in region i
$\Psi_{i,n}(x)$	The n^{th}-order TM surface wave mode function in region i
$\Psi_i(x,u)$	TM radiation mode function in region i
ρ	Cylindrical coordinate radial distance from the origin
τ^b	Transmission coefficient for the surface wave incident from the right to a step discontinuity plane
τ^f	Transmission coefficient for the surface wave incident from the left to a step discontinuity plane
θ	Elevation angle measured with respective to the z-axis
θ_S	The angle θ where the maximum of side lobe peaks is found

CHAPTER 1

INTRODUCTION

Current interest in tapered dielectric radiators stems from their compatibility with dielectric waveguides and the availability of both lowloss silicon and solid state energy sources, which permit integration for use in millimeter-wave and integrated optical devices [1]-[4]. Such devices usually involve open structures in which the electromagnetic field is not confined by metal walls on all sides. Hence, energy leakage occurs. For a structure to be a waveguide, the leakage has to be minimized. If the structure is an antenna then efficient coupling to the radiation field must be affected. By tapering the end section of a dielectric guide along its axis, a guided surface wave field gets transformed into a radiation field which is characterized by maximum intensity in the forward direction. Tapering the dielectric guide, as opposed to suddenly truncating it, will significantly reduce the VSWR on the uniform section of the guide and improve the radiation characteristics of the tapered section (increased directivity and decreased half-power beamwidth), thus resulting in an antenna of improved performance over a wide frequency band [5]-[7].

Tapered dielectric rod antennas have been known for many years [4]. It is surprising, therefore, that a good antenna theory for these antennas has not become available in the meantime. A possible reason for the absence of an accurate antenna theory is that the geometry of these tapered dielectric antennas, though strikingly simple, does not lend itself to convenient representation in a separable coordinate system. Rigorous theoretical approaches to analyze these antennas, such as, coupled mode theory

or the full wave method [8]-[10] are available. However, they are mathematically very complex and usually require an iterative procedure to obtain a solution of acceptable accuracy.

To simplify somewhat the analysis while still yielding physical insights, the two-dimensional structure of a dielectric wedge antenna fed by a slab waveguide of the same material is examined. A fundamental even TE or TM surface wave mode is assumed to be guided by the dielectric slab that terminates into the wedge antenna. The dielectric wedge is modeled by using the staircase approximation. The field scattered by each step discontinuity is then rigorously formulated as a mode-matching problem and solved numerically. The method of solution is an extension of the step-transition method introduced by Marcuse [11], [12] and improved upon by Suchoski, Jr. and Ramaswamy [13]. Solution of the step discontinuity problem provides the basis for the solution of the overall wedge antenna problem. Suchoski, Jr. and Ramaswamy have applied their method to transitions between uniform optical waveguides of different cross sections. The antenna problem treated in the dissertation requires a higher degree of accuracy. This is achieved by devising an iterative approach to the (overall) problem and by more accurately evaluating certain integrals that resulted from the mode-matching procedure and extend over infinite ranges. Furthermore, by an appropriate renormalization of the modal fields, a conspicuous pattern discontinuity problem occurring in the plane normal to the forward direction is resolved. This problem appeared in the existing theories on dielectric step transitions [11]-[13] as well as in [14]-[16]. The need for higher accuracy derives from the objective to demonstrate the extremely low side lobe capability of tapered dielectric antennas and from the fact

that in the tip region of the antenna strong mode coupling occurs, an effect obviously not present in transitions between uniform waveguides of finite cross section.

Many methods have been developed to study taper transitions between different dielectric guides or fibers. Several approaches, including the coupled mode theory, the step-transition method and the propagating-beam method, are reviewed in [13], which also introduces the so called "exact numerical method". This method is based on Marcuse's step-transition method, but applies orthogonality relations to obtain a sparse, diagonally dominant matrix that allows for repeatable, efficient and accurate numerical solution of the linear system of equations which is obtained at each step discontinuity. The more accurate formulation of this method, which is used here along with the modal field renormalization and the iteration procedure mentioned above, is developed for the TE polarization in Chapter 2. Additionally, the TM formulation is described in Chapter 3, followed by the numerical results in Chapter 4. Since the improved "exact numerical method" depends on the accuracy that is obtained at a single step discontinuity, comparisons are made in Chapter 4 with the published results of Suchoski, Jr. and Ramaswamy, Rozzi, and Hirayama and Koshiba [13]-[16] for the single step discontinuity problem. In Chapter 4, the radiation patterns of directive gain for the integrated slab waveguide/wedge antenna and the reflection coefficient of the surface wave in the slab guide are presented for various wedge lengths and for different dielectric materials. In addition, different antenna geometries are studied to compare their characteristics with those of the linearly wedge antenna. Finally, frequency characteristics of the linearly tapered wedge antenna are examined.

The graphs and data show that linearly tapered dielectric wedge antennas are endfire antennas with the following general characteristics that apply, in particular, to slender wedges of small aperture angle, the practically interesting case:

- A very low reflection coefficient of the surface wave in the slab guide (typically having amplitude $<10^{-3}$ for a wedge length $L>10\lambda_0$) resulting in a low VSWR on the feed guide; λ_0 is the free space wavelength;

- A directivity that increases monotonically with wedge length L, at least up to $L=20\lambda_0$, the maximum length considered here, indicating that wedge antennas with linear profile do not have a gain limitation;

- A directivity that moderately decreases with ε_r for the TE polarization. For wedges with relative lengths of $L/\lambda_0=1,\ldots,$ 20, the maximum directive gain is typically 8-11 dB for $\varepsilon_r=2.56$ and 6-10 dB for $\varepsilon_r=12$;

- A directivity that remains essentially identical with varying ε_r for the TM polarization. For wedges with relative lengths of $L/\lambda_0=1,\ldots,$ 20, the maximum directive gain is typically 7-13 dB;

- A radiation pattern with very low side lobes, a pattern shape very desirable for many applications;

- An extremely low VSWR over a wide range of frequency, indicating that the dielectric wedge antenna is a broadband antenna.

It is assumed here that the antenna is fed by a dielectric slab guide of the same permittivity. While the small reflection coefficient and the decrease (if any) of directivity with ε_r are predictable, the apparent absences of the gain limitation (with antenna length) and the low side lobes of tapered dielectric antennas are results that, to our knowledge, have been demonstrated theoretically for the first time.

CHAPTER 2

TE FORMULATION

The physical geometry under consideration is a lossless, semi-infinite, dielectric slab waveguide of thickness $2D_1$ which, beginning at $z = 0$, is tapered to a point at $z = L$. A model for this tapered dielectric antenna is depicted in Figure 2.1, wherein the smooth tapered portion is replaced by short slab waveguide segments of equal length Δz and uniform cross-sectional areas of progressively smaller widths $2D_i$, i = 2, 3, 4,..., M–1, with $D(z) = 0$, for $z > L' = \Delta z(M-2)$, where $M = 5$ is used in Figure 2.1. In this figure, only $M-1$ uniform slab waveguides are shown and the tapered section is modeled by $M-2$ slab waveguides of successfully smaller widths. The regions of space where the far-zone electromagnetic field is to be found are region M and region 1. The latter region $z \le 0$ is occupied by the semi-infinite slab waveguide. The taper is segmented into $M-2$ regions identified by i = 2, 3, 4,…, $M-1$, while the semi-infinite free space region is identified as region $i = M$. Each region i, i = 1, 2, 3,..., M, is further separated into 3 sub-regions identified by I_i, II_i and III_i where II_i is occupied by the dielectric and sub-regions I_i and III_i are free space above and below the dielectric, respectively. In the last region $i = M$, II_M does not exist since the dielectric is taken to terminate at $z = L'$.

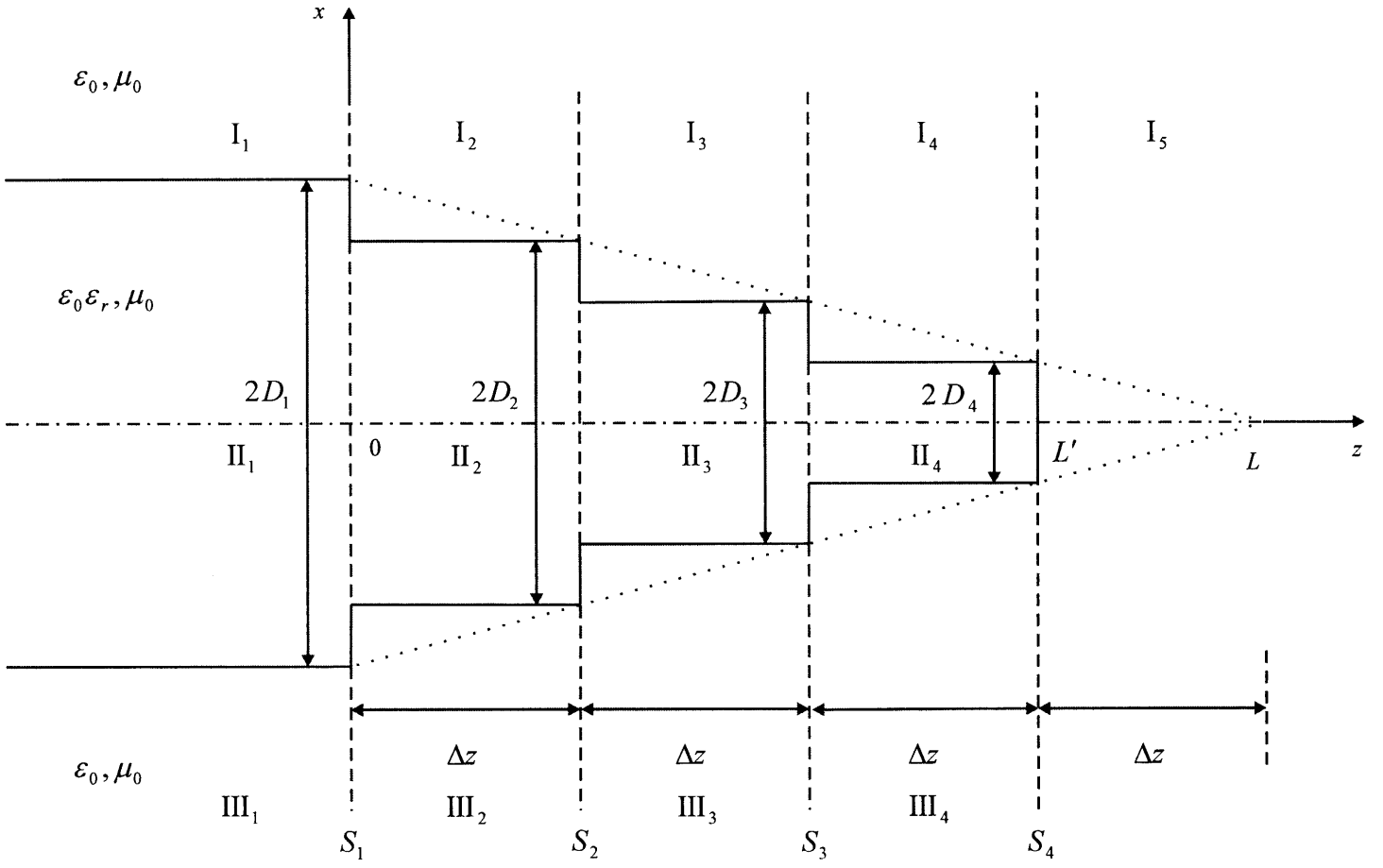

Figure 2.1 Staircase approximation for tapered dielectric antenna with $M = 5$.

2.1 TE Modal Representation

A fundamental, even TE surface wave mode of the uniform dielectric slab waveguide is assumed to be incident in the $+z$ direction from $z \to -\infty$, with unity power. The mode does not experience cutoff and can propagate along very thin slab waveguides. Because of this excitation and the geometry in Figure 2.1, the field in each section i is independent of the y-coordinate and is TE everywhere with field components $E_{y,i}$, $H_{x,i}$ and $H_{z,i}$.

The TE modes of the dielectric slab guide are well known [12], [17], [18]. The complete mode spectrum consists of a finite discrete spectrum of surface wave modes and an infinite continuous spectrum of radiation modes. Due to the antenna geometry and the excitation assumed here, only the even modes need to be considered. Thus, the field in region i can be written as

$$E_{y,i} = \sum_{n=0}^{N_m^{TE}} v_{i,n}(z)\Phi_{i,n}(x) + \int_{u=0}^{\infty} v_i(z,u)\Phi_i(x,u)du \tag{2.1a}$$

$$\eta_0 H_{x,i} = \sum_{n=0}^{N_m^{TE}} i_{i,n}(z)\Phi_{i,n}(x) + \int_{u=0}^{\infty} i_i(z,u)\Phi_i(x,u)du \tag{2.1b}$$

$$\eta_0 H_{z,i} = -\frac{1}{jk_0}\frac{\partial E_{y,i}}{\partial x} \tag{2.1c}$$

where the sum on the right side represents the surface wave modes and the integral identifies the radiation modes. The parameter n is the mode order and N_m^{TE} is the highest one of the TE surface wave modes. The parameters η_0 and k_0 are the free space wave

impedance and wavenumber, respectively. The longitudinal component $H_{z,i}$ will be omitted in the following since the transverse components $E_{y,i}$, $H_{x,i}$ and the boundary conditions characterize the field completely. Assuming a time dependence of $e^{j\omega t}$, the z-dependent expansion coefficients in (2.1) are expressed (with assumed normalization) by

$$v_{i,n}(z) = \frac{k_0}{\beta_{i,n}}[A_{i,n}e^{-j\beta_{i,n}z} + B_{i,n}e^{j\beta_{i,n}z}] \tag{2.2a}$$

$$v_i(z,u) = \frac{k_0}{\beta(u)}[A_i(u)e^{-j\beta(u)z} + B_i(u)e^{j\beta(u)z}] \tag{2.2b}$$

$$i_{i,n}(z) = \frac{1}{jk_0}\frac{dv_{i,n}(z)}{dz}, \quad i_i(z,u) = \frac{1}{jk_0}\frac{\partial v_i(z,u)}{\partial z} \tag{2.2c}$$

where $A_{i,n}$, $A_i(u)$ are the amplitudes of the $+z$ traveling modes and $B_{i,n}$, $B_i(u)$ are those of the $-z$ traveling modes. The TE mode functions $\Phi_i(x)$ and $\Phi_i(x,u)$ in (2.1) determine the x-dependence of the modes and are given by

$$\Phi_{i,n}(x) = \begin{cases} C_{i,n}\cos(k_{x,i,n}x), & |x| \le D_i \\ C_{i,n}\cos(k_{x,i,n}D_i)e^{-\alpha_{x,i,n}(|x|-D_i)}, & |x| > D_i \end{cases} \tag{2.3a}$$

with

$$C_{i,n} = [\frac{2\alpha_{x,i,n}}{1+\alpha_{x,i,n}D_i}]^{\frac{1}{2}} \tag{2.3b}$$

$$k_{x,i,n} = [k^2 - \beta_{i,n}^2]^{\frac{1}{2}}, \quad \alpha_{x,i,n} = [\beta_{i,n}^2 - k_0^2]^{\frac{1}{2}} \tag{2.3c}$$

and

$$\Phi_i(x,u)=\begin{cases} C_i(u)\cos(vx), & |x|\le D_i \\ C_i(u)\{\cos(vD_i)\cos[u(|x|-D_i)]-\dfrac{v}{u}\sin(vD_i)\sin[u(|x|-D_i)]\}, & |x|>D_i \end{cases} \tag{2.4a}$$

with

$$C_i(u)=\{\frac{\pi}{2}[\cos^2(vD_i)+(\frac{v}{u})^2\sin^2(vD_i)]\}^{-\frac{1}{2}} \tag{2.4b}$$

$$v=(k^2-k_0^2+u^2)^{\frac{1}{2}} \tag{2.4c}$$

The parameter $k=k_0\varepsilon_r^{\frac{1}{2}}$ is the wavenumber of the slab material. The propagation constants $\beta_{i,n}$ of the TE surface wave modes depend on the slab width D_i and are determined by the dispersion relation

$$k_{x,i,n}\tan(k_{x,i,n}D_i)=\alpha_{x,i,n} \tag{2.5}$$

For any D_i this equation has a finite number of solutions, which are real and lie within the range $k_0<\beta_{i,n}<k$. The propagation constants $\beta(u)$ of the radiation modes are independent of D_i and given by

$$\beta(u)=\begin{cases} (k_0^2-u^2)^{\frac{1}{2}}, & \text{for } u<k_0 \\ -j(u^2-k_0^2)^{\frac{1}{2}}, & \text{for } u>k_0 \end{cases} \tag{2.6}$$

Obviously for $u<k_0$, the radiation modes are of the propagating type and for $u>k_0$, they are of the evanescent type.

With the expressions (2.3) and (2.4), the modes satisfy the orthogonality relations

$$\int_{x=0}^{\infty} \Phi_{i,m}(x)\Phi_{i,n}(x)dx = \delta_{mn} \tag{2.7a}$$

$$\int_{x=0}^{\infty} \Phi_{i}(x,u)\Phi_{i}(x,u')dx = \delta(u-u') \tag{2.7b}$$

$$\int_{x=0}^{\infty} \Phi_{i,n}(x)\Phi_{i}(x,u)dx = 0 \tag{2.7c}$$

where $\delta(u-u')$ is the Dirac delta function and δ_{mn} is the Kronecker delta symbol.

In the following, it will be assumed that the dielectric guide feeding the antenna supports only one surface wave mode, the fundamental mode ($n=0$), which does not have a cutoff frequency. This assumption requires that the width $2D_1$ of the guide satisfies

$$\frac{D_1}{\lambda_0} < 0.5(\varepsilon_r - 1)^{-\frac{1}{2}} \tag{2.8}$$

Equations (2.1)-(2.6) describe the field in the uniform slab guide sections of the wedge antenna, i.e., in the regions between the step transition planes S_1, S_2, S_3,..., S_{M-1} (where $M=5$ for the antenna of Figure 2.1). The step transitions in these planes are characterized by the boundary conditions

$$E_{y,i}(x,z_i) = E_{y,i+1}(x,z_i), \quad -\infty < x < +\infty, \quad i = 1, 2,\ldots, M-1 \tag{2.9a}$$

and

$$H_{x,i}(x,z_i) = H_{x,i+1}(x,z_i), \quad -\infty < x < +\infty, \quad i = 1, 2,\ldots, M-1 \tag{2.9b}$$

where z_i is the location of the plane S_i. By using these boundary conditions and by subsequently discretizing and truncating the spectrum of radiation modes, a linear system is obtained such that each transition plane S_i links the amplitudes of the modes traveling away from this plane to the amplitudes of the modes incident upon this plane. In other words, the method used here for the characterization of the step discontinuities is akin to a scattering matrix formulation of the problem. However, the matrix coefficients are not calculated explicitly. Instead, an algorithm is used that solves the linear system at each step transition directly.[1] This algorithm will be explained in Section 2.2. As pointed out before, it is a key element of the numerical analysis; its accuracy determines the accuracy of the overall solution.

[1] Calculating the scattering matrix at a given step discontinuity from the corresponding linear system would require certain additional matrix inversions and matrix multiplications requiring more computer time and possibly leading to a reduction in accuracy. The reason for solving the linear system directly at each junction is numerical expediency. Conceptually, there is little difference between this method and an explicit scattering matrix formulation of the problem.

2.2 Higher-Order Partial Fields

With the mode-matching algorithm in place, the overall antenna problem is then solved by an iteration procedure which is outlined here using Figure 2.2. As shown in Figure 2.2,[2] a fundamental surface wave mode is initially guided by a slab waveguide of thickness $2D_1$. When it strikes discontinuity plane S_1, scattering occurs. A forward progression first-order solution at S_1 is obtained by calculating the scattering mode amplitudes R_{10}^{f1}, T_{10}^{f1}, $R_1^{f1}(u)$ and $T_1^{f1}(u)$ established from the amplitude A_{10}^{f1} of the surface wave mode incident from the left while, for the moment, neglecting the effect of the modes incident from the right having amplitudes R_{20}^{f1} and $R_2^{f1}(u)$. The determination of scattering mode amplitudes is repeated at each subsequent step discontinuity S_i, $i = 2, 3, 4, ..., M-1$. The forward progression first-order solution for plane S_i is obtained similarly by calculating the outgoing mode amplitudes $R_{i,0}^{f1}$, $T_{i,0}^{f1}$, $R_i^{f1}(u)$ and $T_i^{f1}(u)$ established from modes incident from the left while again neglecting the effect of the modes incident from the right having amplitudes $R_{i+1,0}^{f1}$ and $R_{i+1}^{f1}(u)$. The incidences upon this plane now include both a single surface wave mode with amplitude $A_{i,0}^{f1}$ and the forward traveling radiation modes with amplitudes $A_i^{f1}(u)$, which are the phase delay versions of forward scattering amplitudes at the prior plane S_{i-1}.

---

[2] Note in Figure 2.2 that the forward progression surface wave and radiation modes incident upon a step transition plane S_i have amplitudes denoted by $A_{i,0}^{f1}$ and $A_i^{f1}(u)$, respectively, while the backward progression surface wave and radiation modes incident upon S_i have amplitudes denoted by $B_{i,0}^{b1}$ and $B_i^{b1}(u)$, respectively. This notation differs from that used in (2.2) where the subscript i on the mode amplitudes A_i and B_i identifies the region i of half-width D_i. In the remainder of this dissertation, the subscript "i" on the mode amplitudes A_i and B_i as well as on the mode amplitudes T_i and R_i, to be defined shortly, is used to refer to the transition plane S_i where scattering occurs.

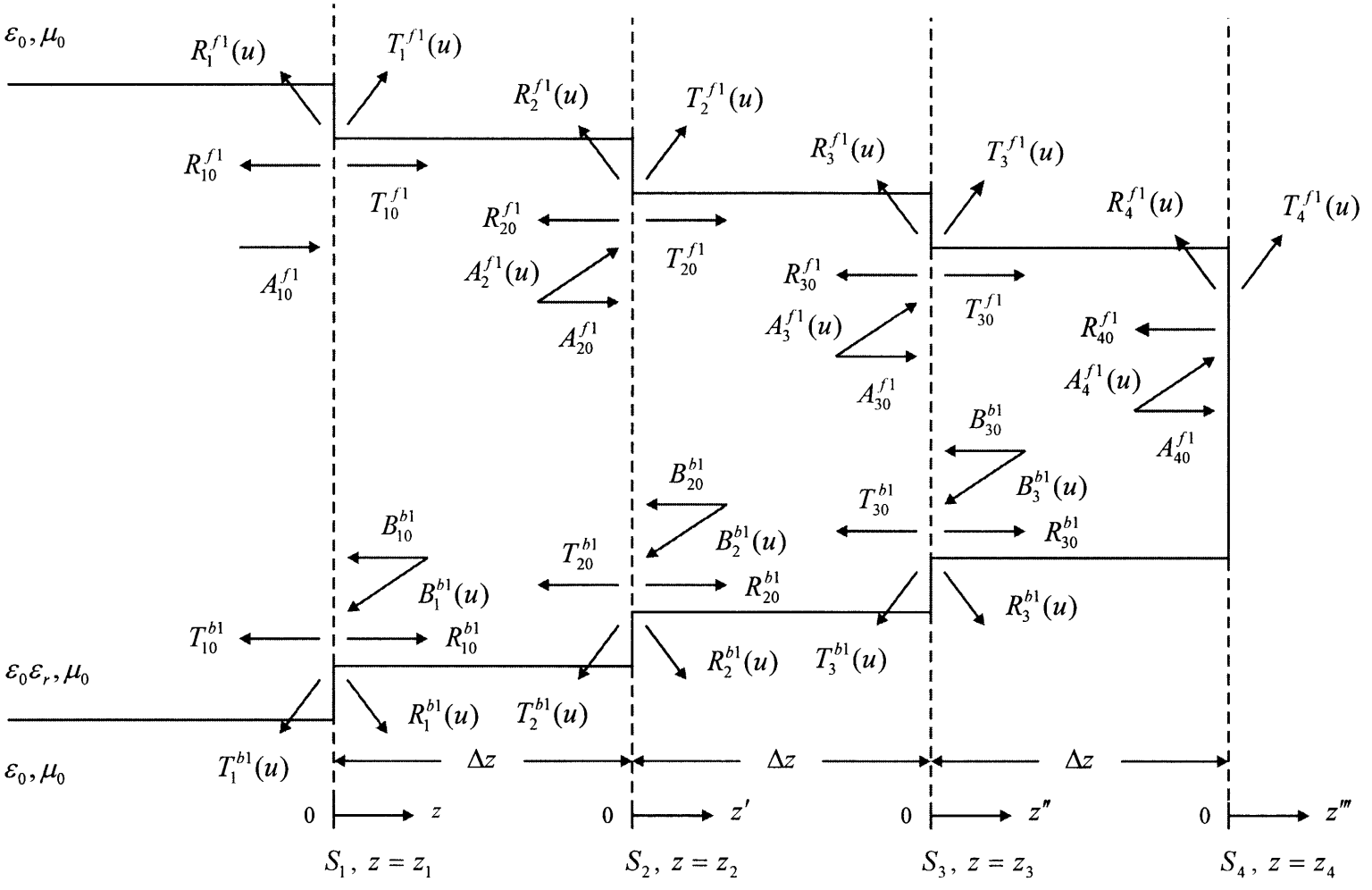

Figure 2.2 First forward and backward partial field wave constituents at each step discontinuity.

By proceeding from the base of the antenna to its tip (in the forward direction), the forward progression first-order solution established due to scattering at each discontinuity plane S_i is obtained. Then, the forward progression first-order partial fields in the region of interest i, i = 1, 2, 3,..., M, can be constructed from the wave constituents due to forward scattering from the boundary plane to the left (S_{i-1}) and backward scattering from the boundary plane to the right (S_i), e.g.,

$$E_{y,i}^{f1} = \begin{cases} E_{y,inc} + E_{y,1}^{f1}\Big|_{S_1}, & \text{for } i = 1 \\ E_{y,i}^{f1}\Big|_{S_{i-1}} + E_{y,i}^{f1}\Big|_{S_i}, & \text{for } i = 2,3,4,...,M-1 \\ E_{y,M}^{f1}\Big|_{S_{M-1}}, & \text{for } i = M \end{cases} \tag{2.10}$$

where $E_{y,i}^{f1}$ is the forward progression first-order partial field in region i and $E_{y,inc}$ is the electric field of the incidence. Subscripts S_{i-1} and S_i identify the discontinuity planes where scattering fields are generated. In the free space region i = M, the field (2.10) is calculated only from the forward scattering from the boundary plane to the left. Meanwhile, in the feed guide region i = 1, it is calculated from backward scattering from the boundary plane to the right. In each region i, the partial fields $H_{x,i}^{f1}$ and $H_{z,i}^{f1}$ are similarly obtained. The subscripts on terms other than the mode amplitudes define the regions where the partial fields exist. The superscript "$f1$" identifies the first forward progression.

To obtain the radiation fields in the backward range ($90^\circ < \theta < 180^\circ$), the waves that progress to the left (in backward direction) that were ignored in the above

formulation of the first forward progression must be considered. For the backward progression, by proceeding from the tip to the base, the situation is reversed. A backward progression first-order solution at plane S_i is obtained by calculating the scattering mode amplitudes $R_{i,0}^{b1}$, $T_{i,0}^{b1}$, $R_i^{b1}(u)$ and $T_i^{b1}(u)$ established from the modes incident upon plane S_i from the right having amplitudes $B_{i,0}^{b1}$ and $B_i^{b1}(u)$ while, for the moment, neglecting the effect of the modes with amplitude $R_{i-1,0}^{b1}$ and $R_{i-1}^{b1}(u)$ incident upon the plane S_i from the left. The incident wave fields at plane S_i are contributed from two scattering events. The first event is that of the "$f1$" wave fields scattered in the backward direction, i.e., $R_{i+1,0}^{f1}$ and $R_{i+1}^{f1}(u)$, which were ignored at S_{i+1} during the first forward progression. The second event is that of the "$b1$" wave fields transferred into region $i+1$ due to scattering at S_{i+1}, i.e., $T_{i+1,0}^{b1}$ and $T_{i+1}^{b1}(u)$, during this (the first) backward progression (For $i = M-2$, $T_{i+1,0}^{b1}$ and $T_{i+1}^{b1}(u)$ are not present). By considering wave progression to the left and performing mode-matching (described in Section 2.3) at each step discontinuity S_{M-2}, S_{M-3}, S_{M-4},..., S_1 successively, the backward progression first-order partial fields in each region i, i = 1, 2, 3,..., $M-1$, can be obtained, which are designated as $E_{y,i}^{b1}$, $H_{x,i}^{b1}$ and $H_{z,i}^{b1}$.

The higher-order wave field solutions can be found by repeating the above process. To find the forward progression second-order solution, one proceeds again from the base of the antenna to the tip. The forward progression second-order solution at plane S_i, i = 2, 3, 4,..., $M-1$, now results from two scattering events occurring at plane S_{i-1}. The first event is that of "$b1$" wave fields scattered at S_{i-1} to the right, i.e., $R_{i-1,0}^{b1}$ and

$R_{i-1}^{b1}(u)$, which were ignored during the first backward progression. The second event is that of wave fields transferred into region i due to scattering at S_{i-1}, i.e., $T_{i-1,0}^{f2}$ and $T_{i-1}^{f2}(u)$, during the second forward progression (For the second and higher forward progression, $p \geq 2$, $T_{1,0}^{f,p}$ and $T_1^{f,p}(u)$ are not present because scattering at S_1 now are established from the backward progression first-order solution, not directly from the surface wave initially incident in the +z direction on the feed guide). The backward progression second-order wave solution at plane S_i can be found in a similar fashion as that of the first backward progression. If this process is repeated, the higher-order partial fields are generated.

The forward progression first-order amplitudes, of course, are preserved, playing the role of "forcing terms" for the backward progression first-order solution. The accuracy of the results can be increased by repeating this process. In this way, the total field in region i is obtained as a superposition of forward and backward traveling partial fields

$$E_{y,i}^{Total} = \begin{cases} E_{y,1}^{f1} + \sum_{p=1}^{N_b} E_{y,1}^{b,p}, & \text{for } i = 1 \\ \sum_{p=1}^{N_f} E_{y,i}^{f,p} + \sum_{p=1}^{N_b} E_{y,i}^{b,p}, & \text{for } i = 2, 3, 4, \ldots, M-1 \\ \sum_{p=1}^{N_f} E_{y,M}^{f,p}, & \text{for } i = M \end{cases} \tag{2.11}$$

where parameters N_f and N_b are the total number of forward and backward progressions, respectively; $E_{y,i}^{f,p}$ and $E_{y,i}^{b,p}$ are, respectively, the forward and backward p^{th}-order partial field in region *i*.

The iteration scheme can be expected to converge well since, in particular for slender wedges of small aperture angle (the practically interesting case), the forward traveling mode amplitudes will dominate over the backward traveling mode amplitudes. A detailed discussion of the mode-matching algorithm and iteration procedure follows.

2.3 Mode-Matching of Partial Wave Fields at a Step Transition Plane

Refer to Figure 2.2. Initially, an incident even TE surface wave mode of order $n = 0$ (labeled A_{10}^{f1}) is guided by a slab waveguide of thickness $2D_1$ in region 1 (z < 0). When this incident wave strikes the step discontinuity at $z = 0$ (boundary plane S_1), transmitted (T_{10}^{f1}) and reflected (R_{10}^{f1}) surface waves as well as forward ($T_1^{f1}(u), 0 \le u < \infty$) and backward ($R_1^{f1}(u), 0 \le u < \infty$) radiation modes are excited.[3] Ignore, for the moment in region 2, both the backward going surface wave (R_{20}^{f1}) and backward going radiation modes ($R_2^{f1}(u), 0 \le u < \infty$) that are established because of the step discontinuities to the right at S_i, i = 2, 3, 4,..., $M-1$. Under these conditions, the unknown parameters are amplitudes of reflected wave ($R_{10}^{f1}, R_1^{f1}(u)$) and amplitudes of transmitted wave (T_{10}^{f1}, $T_1^{f1}(u)$) for the single step discontinuity at $z = 0$. The partial fields E_{y1}^{f1} and H_{x1}^{f1} in region 1 (z < 0) take the forms of

---

[3] The transmission and reflection amplitudes $T_{i,0}^{f1}$, $T_i^{f1}(u)$, $R_{i,0}^{f1}$ and $R_i^{f1}(u)$ as defined here do not have the meaning of scattering matrix coefficients; they are mode amplitudes.

$$E_{y1}^{f1} = \frac{k_0}{\beta_{10}}[A_{10}^{f1}e^{-j\beta_{10}z} + R_{10}^{f1}e^{j\beta_{10}z}]\Phi_{10}(x) + \int_{u=0}^{\infty}\frac{k_0}{\beta(u)}R_1^{f1}(u)e^{j\beta(u)z}\Phi_1(x,u)du \qquad (2.12a)$$

and

$$\eta_0 H_{x1}^{f1} = -[A_{10}^{f1}e^{-j\beta_{10}z} - R_{10}^{f1}e^{j\beta_{10}z}]\Phi_{10}(x) + \int_{u=0}^{\infty}R_1^{f1}(u)e^{j\beta(u)z}\Phi_1(x,u)du \qquad (2.12b)$$

It is assumed that the wedge antenna at $z = 0$ is fed by monomode surface wave with unity power, which yields $A_{10}^{f1} = [\eta_0\beta_{10}/k_0]^{\frac{1}{2}}$. The partial fields in region 2 ($0 < z < \Delta z$) established by scattering at step discontinuity S_1 are given by

$$E_{y2}^{f1} = \frac{k_0}{\beta_{20}}T_{10}^{f1}e^{-j\beta_{20}z}\Phi_{20}(x) + \int_{u=0}^{\infty}\frac{k_0}{\beta(u)}T_1^{f1}(u)e^{-j\beta(u)z}\Phi_2(x,u)du \qquad (2.13a)$$

and

$$\eta_0 H_{x2}^{f1} = -T_{10}^{f1}e^{-j\beta_{20}z}\Phi_{20}(x) - \int_{u=0}^{\infty}T_1^{f1}(u)e^{-j\beta(u)z}\Phi_2(x,u)du \qquad (2.13b)$$

Other than for the mode amplitudes, the subscripts "1" and "2" define the regions where the partial fields exist; whereas the superscript "$f1$" identifies the first forward partial field contributions to the rigorous field solution. The use of the term "forward" signifies that the step discontinuities to the right are considered sequentially. "Backward" partial field contributions are obtained by considering wave progression back from the tip toward the step discontinuities to the left sequentially. The backward going waves that were ignored during the forward progression toward the tip are included in the determination of these "backward" partial fields and hence allow for a rigorous determination of the field solution.

The unknown reflection and transmission mode amplitudes at each step discontinuity are found by following a modified version of the mode-matching procedure discussed in [13]. However, significant differences in the formulation are introduced. Firstly, the parameters $T_i^{f1}(u=0)$, $R_i^{f1}(u=0)$, $T_i^{f1}(u=k_0)$ and $R_i^{f1}(u=k_0)$ are not assumed to be zero as was done in [13]. Secondly, in the numerical evaluation of the infinite integral, truncation is taken to exclude only higher-order evanescent radiation modes[4] that decrease rapidly with z while those of lower order ($k_0 < u \leq 2k_0$, typically) are included in the analysis. Thirdly, certain integrals are evaluated more accurately than was done in [13]. Fourthly, normalized parameters (2.2) are introduced which insure pattern continuity at $\theta = 90^\circ$. Finally, an iteration procedure is implemented which incorporates the backscattered partial fields that were initially ignored when considering propagation in the forward (+z) direction; this permits a rigorous determination of the field since no partial waves are ignored.

The method in [13] as modified above is chosen to solve the problem of scattering at a single step discontinuity because the system of linear equations obtained involves a numerically efficient matrix that is sparse and diagonally dominant and because a similar system of equations is obtained at each subsequent step discontinuity.

The unknown amplitudes R_{10}^{f1}, $R_1^{f1}(u)$, T_{10}^{f1} and $T_1^{f1}(u)$ are determined by requiring that the total tangential components of the electric and magnetic fields, $E_{y,i}$ and $H_{x,i}$, $i = 1, 2$, are continuous at the step discontinuity plane S_1,

---

[4] Evanescent mode coupling was assumed to be a weak effect and was ignored a priori in [13]. This was not done here because (a) mode-matching planes are closely spaced (which occurs also in [13]) so that this type of coupling is present, (b) high accuracy is required in analyzing the wedge antenna so as to obtain the extremely low side lobe levels and (c) evanescent modes are required for pattern continuity at $\theta = 90^\circ$.

$$E_{y1}(x,z=0)=E_{y2}(x,z=0) \text{ and } H_{x1}(x,z=0)=H_{x2}(x,z=0) \tag{2.14}$$

The above continuity requirements yield the following equations:

$$\frac{1}{\beta_{10}}[A_{10}^{f1}+R_{10}^{f1}]\Phi_{10}(x)+\int_{u=0}^{\infty}\frac{1}{\beta(u)}R_1^{f1}(u)\Phi_1(x,u)du$$

$$=\frac{1}{\beta_{20}}T_{10}^{f1}\Phi_{20}(x)+\int_{u=0}^{\infty}\frac{1}{\beta(u)}T_1^{f1}(u)\Phi_2(x,u)du \tag{2.15a}$$

and

$$-[A_{10}^{f1}-R_{10}^{f1}]\Phi_{10}(x)+\int_{u=0}^{\infty}R_1^{f1}(u)\Phi_1(x,u)du=-T_{10}^{f1}\Phi_{20}(x)-\int_{u=0}^{\infty}T_1^{f1}(u)\Phi_2(x,u)du \tag{2.15b}$$

The parameters $(\beta_{10},\beta(u))$ and $(\beta_{20},\beta(u))$ are propagation constants in regions $i=1$ and $i=2$, respectively. The propagation constants β_{10} and β_{20} are determined from the eigenvalue equation (2.5) for D_1 and D_2, respectively, while $\beta(u)$ is given by (2.6).

Multiplying both sides of (2.15a) and (2.15b) by $\Phi_{10}(x)$, integrating over x from 0 to ∞, interchanging the order of integration over u and x and using orthogonality relations in (2.7a) and (2.7c) lead to the following equations, respectively:

$$A_{10}^{f1}+R_{10}^{f1}=\frac{\beta_{10}}{\beta_{20}}Q_{0,0}(D_1,D_2)T_{10}^{f1}+\int_{u=0}^{\infty}\frac{\beta_{10}}{\beta(u)}Q_0(u;D_1,D_2)T_1^{f1}(u)du \tag{2.16a}$$

and

$$A_{10}^{f1}-R_{10}^{f1}=Q_{0,0}(D_1,D_2)T_{10}^{f1}+\int_{u=0}^{\infty}Q_0(u;D_1,D_2)T_1^{f1}(u)du \tag{2.16b}$$

where

$$Q_{0,0}(D_1, D_2) = \int_{x=0}^{\infty} \Phi_{10}(x)\Phi_{20}(x)dx \tag{2.16c}$$

$$Q_0(u; D_1, D_2) = \int_{x=0}^{\infty} \Phi_{10}(x)\Phi_2(x,u)dx \tag{2.16d}$$

The explicit form of overlap integrals $Q_{0,0}(D_i, D_{i+1})$ and $Q_0(u; D_i, D_{i+1})$ are shown in Appendix C.

To solve (2.16a) and (2.16b), the integrals over x are first evaluated explicitly. Next, the remaining integrals over u are truncated at $u = u_{\max}$ and discretized into $N_T^I = N/2$ intervals (N segments); see Appendix E. The value of $u_{\max}$ insures that both propagating and evanescent radiation modes are included. Simpson's one-third rule is used to evaluate integrals in intervals devoid of singularities. Integration across singularities is handled by established method since the singularities encountered are integrable (see Footnote 5). Because of the discretization process, $2N + 4$ unknowns now need to be determined; they are R_{10}^{f1}, T_{10}^{f1}, $R_1^{f1}(u_m)$ and $T_1^{f1}(u_m)$, m = 0, 1, 2, ..., N, where N is an even integer. However, (2.16) constitutes only two equations. Additional equations are obtained by multiplying both sides of (2.15a) and (2.15b) by $\Phi_1(x,u')$, integrating over x from 0 to ∞, interchanging the order of integration over u and x and using orthogonality relations in (2.7b) and (2.7c) to yield the following equations, respectively:

$$R_1^{f1}(u = u') = \frac{\beta(u')}{\beta_{20}} Q_0'(u'; D_1, D_2) T_{10}^{f1} + \int_{u=0}^{\infty} \frac{\beta(u')}{\beta(u)} Q(u', u; D_1, D_2) T_1^{f1}(u)du \tag{2.17a}$$

and

$$-R_1^{f1}(u=u') = Q_0'(u';D_1,D_2)T_{10}^{f1} + \int_{u=0}^{\infty} Q(u',u;D_1,D_2)T_1^{f1}(u)du \qquad (2.17b)$$

where

$$Q_0'(u';D_1,D_2) = \int_{x=0}^{\infty} \Phi_1(x,u')\Phi_{20}(x)dx \qquad (2.17c)$$

$$Q(u',u;D_1,D_2) = \int_{x=0}^{\infty} \Phi_1(x,u')\Phi_2(x,u)dx \qquad (2.17d)$$

$Q(u',u;D_1,D_2)$ can be shown to take the following form (see Appendix C):

$$Q(u',u;D_1,D_2) = Q_1(u';D_1,D_2)\delta(u-u') + \frac{Q_2(u',u;D_1;D_2)}{u'^2-u^2} + Q_3(u',u;D_1,D_2) \qquad (2.18)$$

By using (2.18), (2.17a) and (2.17b) become

$$\frac{\beta(u')}{\beta_{20}} Q_0'(u';D_1,D_2)T_{10}^{f1} + Q_1(u';D_1,D_2)T_1^{f1}(u=u')$$

$$+ \int_{u=0}^{\infty} \frac{\beta(u')}{\beta(u)} \frac{Q_2(u',u;D_1,D_2)}{u'^2-u^2} T_1^{f1}(u)du$$

$$+ \int_{u=0}^{\infty} \frac{\beta(u')}{\beta(u)} Q_3(u',u;D_1,D_2)T_1^{f1}(u)du - R_1^{f1}(u=u') = 0 \qquad (2.19a)$$

and

$$Q_0'(u';D_1,D_2)T_{10}^{f1} + Q_1(u';D_1,D_2)T_1^{f1}(u=u')$$

$$+ \int_{u=0}^{\infty} [\frac{Q_2(u',u;D_1,D_2)}{u'^2-u^2} + Q_3(u',u;D_1,D_2)]T_1^{f1}(u)du + R_1(u=u') = 0 \qquad (2.19b)$$

As before, the integrals over u in (2.19a) and (2.19b) are truncated at $u = u_{\max} > k_0$ and discretized. Again care must be used in numerically evaluating these integrals because of the occurrence of singularities in the integrand. The singularities encountered are of three types, namely, $1/\beta(u)$, $1/(u'^2 - u^2)$ and $\beta(u')/[\beta(u)(u'^2 - u^2)]$. Away from the above singularities, Simpson's one-third rule is used to evaluate the integrals. Thus, a linear system of equations is obtained which permits the determination of the $2N+4$ unknowns R_{10}^{f1}, T_{10}^{f1}, $R_1^{f1}(u = u_m)$ and $T_1^{f1}(u = u_m)$, m = 0, 1, 2,..., N. As before, the integration across the first two singularities can be handled by established methods since both are integrable[5] (the second in the Cauchy Principal Value sense). The third singularity is more of a problem. It combines the first two singularities but in such a way that for u, $u' \to k_0$ both the numerator and the denominator vanish. Of special note is the integral evaluation for $u' = k_0$ given by

$$\mathrm{PV} \int_{u=0}^{\infty} \frac{\beta(u')}{\beta(u)} \frac{F(u',u)}{u'^2 - u^2} du = -j \frac{\pi}{2k_0} F(u' = k_0, u = k_0) \tag{2.20}$$

where the integrand consists of the third singularity multiplied by an arbitrary continuous function $F(u',u)$ that remains finite for $u \to \infty$. The notation PV in front of the integral sign designates the Cauchy Principal Value integral evaluation. By applying (2.20), (2.19a) becomes

---

[5] The integral is evaluated by expanding the non-singular portion of the integrand in a Taylor series over interval(s) of singularity, using finite difference approximation for the first and second derivatives [54], [55], and evaluating the resulting integrals explicitly.

$$T_1^{f1}(u=k_0)e^{j(\zeta_2-\zeta_1)} - R_1^{f1}(u=k_0) = 0, \quad \text{for } u' = k_0 \tag{2.21a}$$

where

$$\zeta_1 = k_0 D_1 - \tan^{-1}[\varepsilon_r^{\frac{1}{2}} \tan(kD_1)],\ \zeta_2 = k_0 D_2 - \tan^{-1}[\varepsilon_r^{\frac{1}{2}} \tan(kD_2)] \tag{2.21b}$$

The $1/(u'^2 - u^2)$ singularity in (2.19a) is removed by subtracting (2.19a) from (2.19b), which is used for $u' \neq k_0$

$$[1-\frac{\beta(u')}{\beta_{20}}]Q_0'(u';D_1,D_2)T_{10}^{f1} + \int_{u=0}^{\infty} \frac{Q_2(u',u;D_1,D_2)}{\beta(u)[\beta(u)+\beta(u')]} T_1^{f1}(u)du$$

$$+ \int_{u=0}^{\infty} [1-\frac{\beta(u')}{\beta(u)}]Q_3(u',u;D_1,D_2)T_1^{f1}(u)du + 2R_1^{f1}(u=u') = 0 \tag{2.22}$$

Subtracting (2.16a) from (2.16b) yields

$$-2R_{10}^{f1} = [1-\frac{\beta_{10}}{\beta_{20}}]Q_{0,0}(D_1,D_2)T_{10}^{f1} + \int_{u=0}^{\infty} [1-\frac{\beta_{10}}{\beta(u)}]Q_0(u;D_1,D_2)T_1^{f1}(u)du \tag{2.23}$$

In summary, the system of equations at S_1 for forward progression given by (2.16b), (2.23), (2.19b) with (2.21) and (2.22) is

$$R_{10}^{f1} + Q_{0,0}(D_1,D_2)T_{10}^{f1} + \int_{u=0}^{\infty} Q_0(u;D_1,D_2)T_1^{f1}(u)du = A_{10}^{f1} \tag{2.24a}$$

$$2R_{10}^{f1} + [1-\frac{\beta_{10}}{\beta_{20}}]Q_{0,0}(D_1,D_2)T_{10}^{f1} + \int_{u=0}^{\infty} [1-\frac{\beta_{10}}{\beta(u)}]Q_0(u;D_1,D_2)T_1^{f1}(u)du = 0 \tag{2.24b}$$

$$Q_0'(u';D_1,D_2)T_{10}^{f1}+Q_1(u';D_1,D_2)T_1^{f1}(u=u')$$

$$+\int_{u=0}^{\infty}[\frac{Q_2(u',u;D_1,D_2)}{u'^2-u^2}+Q_3(u',u;D_1,D_2)]T_1^{f1}(u)du+R_1^{f1}(u=u')=0 \quad (2.24c)$$

$$[1-\frac{\beta(u')}{\beta_{20}}]Q_0'(u';D_1,D_2)T_{10}^{f1}+\int_{u=0}^{\infty}\frac{Q_2(u',u;D_1,D_2)}{\beta(u)[\beta(u)+\beta(u')]}T_1^{f1}(u)du$$

$$+\int_{u=0}^{\infty}[1-\frac{\beta(u')}{\beta(u)}]Q_3(u',u;D_1,D_2)T_1^{f1}(u)du+2R_1^{f1}(u=u')=0,$$

$$\text{for } u'\neq k_0 \quad (2.24d)$$

$$e^{j(\zeta_2-\zeta_1)}T_1^{f1}(u=k_0)-R_1^{f1}(u=k_0)=0, \quad \text{for } u'=k_0 \quad (2.24e)$$

where

$$\zeta_1=k_0D_1-\tan^{-1}[\varepsilon_r^{\frac{1}{2}}\tan(kD_1)],\ \zeta_2=k_0D_2-\tan^{-1}[\varepsilon_r^{\frac{1}{2}}\tan(kD_2)] \quad (2.24f)$$

Before solving (2.24a)-(2.24e), the following normalized parameters are introduced:

$$\bar{\alpha}_{x,i,0}=\frac{\alpha_{x,i,0}}{k_0},\bar{\beta}_{i,0}=\frac{\beta_{i,0}}{k_0},\ \bar{u}=\frac{u}{k_0},\ \bar{v}=\frac{v}{k_0},\bar{\beta}(\bar{u})=\frac{\beta(u)}{k_0} \quad (2.25a)$$

$$\bar{x}=k_0x,\bar{z}=k_0z,\ \bar{T}_i(\bar{u})=\sqrt{k_0}T_i(u),\ \bar{R}_i(\bar{u})=\sqrt{k_0}R_i(u) \quad (2.25b)$$

Adopting normalized parameters (2.25), (2.24) becomes

$$R_{10}^{f1}+\bar{Q}_{0,0}(\bar{D}_1,\bar{D}_2)T_{10}^{f1}+\int_{\bar{u}=0}^{\infty}\bar{Q}_0(\bar{u};\bar{D}_1,\bar{D}_2)\bar{T}_1^{f1}(\bar{u})d\bar{u}=A_{10}^{f1} \quad (2.26a)$$

$$2R_{10}^{f1}+[1-\frac{\bar{\beta}_{10}}{\bar{\beta}_{20}}]\bar{Q}_{0,0}(\bar{D}_1,\bar{D}_2)T_{10}^{f1}+\int_{\bar{u}=0}^{\infty}[1-\frac{\bar{\beta}_{10}}{\bar{\beta}(\bar{u})}]\bar{Q}_0(\bar{u};\bar{D}_1,\bar{D}_2)\bar{T}_1^{f1}(\bar{u})d\bar{u}=0 \quad (2.26b)$$

$$\overline{Q}_0'(\overline{u}';\overline{D}_1,\overline{D}_2)T_{10}^{f1}+\overline{Q}_1(\overline{u}';\overline{D}_1,\overline{D}_2)\overline{T}_1^{f1}(\overline{u}=\overline{u}')$$

$$+\int_{\overline{u}=0}^{\infty}[\frac{\overline{Q}_2(\overline{u}',\overline{u};\overline{D}_1,\overline{D}_2)}{\overline{u}'^2-\overline{u}^2}+\overline{Q}_3(\overline{u}',\overline{u};\overline{D}_1,\overline{D}_2)]\overline{T}_1^{f1}(\overline{u})d\overline{u}+\overline{R}_1^{f1}(\overline{u}=\overline{u}')=0 \quad (2.26c)$$

$$[1-\frac{\overline{\beta}(\overline{u}')}{\overline{\beta}_{20}}]\overline{Q}_0'(\overline{u}';\overline{D}_1,\overline{D}_2)T_{10}^{f1}+\int_{\overline{u}=0}^{\infty}\frac{\overline{Q}_2(\overline{u}',\overline{u};\overline{D}_1,\overline{D}_2)}{\overline{\beta}(\overline{u})[\overline{\beta}(\overline{u})+\overline{\beta}(\overline{u}')]}\overline{T}_1^{f1}(\overline{u})d\overline{u}$$

$$+\int_{\overline{u}=0}^{\infty}[1-\frac{\overline{\beta}(\overline{u}')}{\overline{\beta}(\overline{u})}]\overline{Q}_3(\overline{u}',\overline{u};\overline{D}_1,\overline{D}_2)\overline{T}_1^{f1}(\overline{u})d\overline{u}+2\overline{R}_1^{f1}(\overline{u}=\overline{u}')=0,$$

$$\text{for } \overline{u}'\neq\overline{k}_0 \quad (2.26d)$$

$$e^{j(\overline{\zeta}_2-\overline{\zeta}_1)}\overline{T}_1(\overline{u}=\overline{k}_0)-\overline{R}_1(\overline{u}=\overline{k}_0)=0, \qquad \text{for } \overline{u}'=\overline{k}_0 \quad (2.26e)$$

with

$$\overline{\zeta}_1=\overline{D}_1-\tan^{-1}[\varepsilon_r^{\frac{1}{2}}\tan(\overline{kD}_1)],\ \overline{\zeta}_2=\overline{D}_2-\tan^{-1}[\varepsilon_r^{\frac{1}{2}}\tan(\overline{kD}_2)] \quad (2.26f)$$

$$\overline{k}=k/k_0 \quad (2.26g)$$

where the normalized overlap integrals in (2.26) are related to unnormalized forms as follows:

$$\overline{Q}_{0,0}(\overline{D}_i,\overline{D}_{i+1})=Q_{0,0}(D_i,D_{i+1}) \quad (2.27a)$$

$$\overline{Q}_0(\overline{u};\overline{D}_i,\overline{D}_{i+1})=\sqrt{k_0}Q_0(u;D_i,D_{i+1}) \quad (2.27b)$$

$$\overline{Q}_0'(\overline{u};\overline{D}_i,\overline{D}_{i+1})=\sqrt{k_0}Q_0'(u;D_i,D_{i+1}) \quad (2.27c)$$

$$\overline{Q}_1(\overline{u};\overline{D}_i,\overline{D}_{i+1})=Q_1(u;D_i,D_{i+1}) \quad (2.27d)$$

$$\overline{Q}_2(\overline{u}',\overline{u};\overline{D}_i,\overline{D}_{i+1})=Q_2(u',u;D_i,D_{i+1})/k_0 \quad (2.27e)$$

$$\overline{Q}_3(\overline{u}',\overline{u};\overline{D}_i,\overline{D}_{i+1})=k_0Q_3(u',u;D_i,D_{i+1}) \quad (2.27f)$$

The procedure is repeated at each subsequent step discontinuity. For example, the difference in the formulation at S_2 in Figure 2.2 is that the non-zero wave constituents, assumed to strike the discontinuity at $z = \Delta z$, include now both a single surface wave mode, represented by A_{20}^{f1}, plus the forward traveling radiation modes, represented by $A_2^{f1}(u)$, $0 \le u < \infty$. These wave amplitudes are related to those at plane S_1 by (2.29) for $i = 2$. Observe that phase accumulation takes place over a distance Δz from one boundary plane to the next one. As before, both the reflected surface wave mode (R_{30}^{f1}) and the reflected radiation modes ($R_3^{f1}(u)$, $0 \le u < \infty$) in region 3 are neglected. The boundary conditions (2.9a) and (2.9b) applied at S_i, i = 2, 3,..., $M-2$, then yield the following constraint equations:

$$\frac{1}{\beta_{i,0}}[A_{i,0}^{f1} + R_{i,0}^{f1}]\Phi_{i,0}(x) + \int_{u=0}^{\infty} \frac{1}{\beta(u)}[A_i^{f1}(u) + R_i^{f1}(u)]\Phi_i(x,u)du$$

$$= \frac{1}{\beta_{i+1,0}} T_{i,0}^{f1}\Phi_{i+1,0}(x) + \int_{u=0}^{\infty} \frac{1}{\beta(u)} T_i^{f1}(u)\Phi_{i+1}(x,u)du \qquad (2.28a)$$

and

$$-[A_{i,0}^{f1} - R_{i,0}^{f1}]\Phi_{i,0}(x) - \int_{u=0}^{\infty}[A_i^{f1}(u) - R_i^{f1}(u)]\Phi_i(x,u)du$$

$$= -T_{i,0}^{f1}\Phi_{i+1,0}(x) - \int_{u=0}^{\infty} T_i^{f1}(u)\Phi_{i+1}(x,u)du \qquad (2.28b)$$

The amplitudes of incident surface wave $A_{i,0}^{f1}$ and radiation waves $A_i^{f1}(u)$ incident upon discontinuity plane S_i, i = 2, 3, 4,..., $M-2$ are related to those of plane S_{i-1} by

$$A_{i,0}^{f1} = T_{i-1,0}^{f1} e^{-j\beta_{i,0}\Delta z},\ A_i^{f1}(u) = T_{i-1}^{f1}(u) e^{-j\beta(u)\Delta z},\ \Delta z = z_i - z_{i-1} \tag{2.29}$$

Note the similarity between (2.28) and (2.15). At the last transition plane $S_i = S_{M-1}$, which separates the dielectric from free space (where $S_{M-1} = S_4$ in Figure 2.1), the constraint equations remain the same as in (2.28), except that the terms involving $T_{i,0}^{f1}$ on the right hand sides are not present. Observe that the phase accumulation over a distance Δz from one boundary plane to the next one appears only in the incident mode amplitudes given in (2.29).

It was noted above that at each step discontinuity S_i, $2N+4$ unknowns had to be determined. Further study of the system of equation (2.28) when $D_{i+1} \neq 0$ shows that $R_i^{f1}(u=0) = T_i^{f1}(u=0) = 0$, i = 1, 2, ..., $M-2$, but that when $D_{i+1} = 0$ $(i+1 = M)$, $R_{M-1}^{f1}(u=0) = 0$, $T_{M-1}^{f1}(u=0) \neq 0$. Thus, there remains $2N+2$ unknowns to be found at each step discontinuity; recall that only radiation modes exist in region M, which is the free space region to the right of the last step ($z > L'$), and the system of equations allows for the determination of $R_{M-1,0}^{f1}$, $R_{M-1}^{f1}(u_m)$, $T_{M-1}^{f1}(u=0)$ and $T_{M-1}^{f1}(u_m)$, m = 1, 2, ..., N, which, as noted, consists of $2N+2$ unknowns.

The first forward partial fields in region 2 were found by applying boundary conditions at S_1. The scatter processes involved are approximated in that certain reflected fields were ignored. It was pointed out that the process was repeated and boundary conditions were applied at S_2, S_3, S_4, ..., S_{M-1} in a similar fashion to obtain the remaining first forward partial fields in regions 2, 3, 4,..., M. In all cases,

the backward surface wave and radiation modes were taken to be zero to the right of S_i, $i = 1, 2, 3,\ldots, M-1$ when the forward partial fields $E_{y,i}^{f1}$, $H_{x,i}^{f1}$ and $H_{z,i}^{f1}$, $i = 1, 2, 3,\ldots, M$, were determined. Other than for the mode amplitudes, the subscript "i" identifies the region where the field is located and the superscript "$f1$" identifies each constituent as being the "first forward" partial field contributions to the rigorous field solution. All the amplitudes defined so far are associated with the first forward progression toward the tip of the antenna.

To obtain the field in the backward range ($90^\circ < \theta < 180^\circ$), the waves that progress to the left (in backward direction) that were ignored in the above formulation of the first forward progression must be considered. This is accomplished by initially considering the backward surface wave mode ($R_{M-1,0}^{b1}$) and the backward radiation modes ($R_{M-1}^{b1}(u), 0 \le u < \infty$) scattered by the abrupt termination of the wedge antenna at S_{M-1} to be scattered by the step discontinuity at S_{M-2}; the superscript "$b1$" in Figure 2.2 denotes the first backward progression of wave fields. By considering wave progression to the left and performing mode-matching at each step discontinuity S_{M-2}, S_{M-3}, S_{M-4},..., S_1 successively, the "first backward" partial field components are obtained in each region. They are designated as $E_{y,i}^{b1}$, $H_{x,i}^{b1}$ and $H_{z,i}^{b1}$, $i = 1, 2, 3,\ldots, M-1$. This process of sequentially considering forward progression and backward progression can be repeated as often as needed to approximate the total field to the desired order of accuracy. Using only the first and second forward progressions (identified by the superscripts $f1$ and $f2$, respectively) and the first and second backward progression (identified by

the superscripts $b1$ and $b2$), the total field constituents in each region i, $i = 1, 2, 3,\ldots, M$, can be formally approximated as follows:

In region 1: $$E_{y1}^{Total} \cong E_{y1}^{f1} + E_{y1}^{b1} + E_{y1}^{b2},\ H_{x1}^{Total} \cong H_{x1}^{f1} + H_{x1}^{b1} + H_{x1}^{b2} \tag{2.30a}$$

In region 2, 3, 4, …, $M-1$:

$$E_{y,i}^{Total} \cong E_{y,i}^{f1} + E_{y,i}^{b1} + E_{y,i}^{f2} + E_{y,i}^{b2}, \quad \text{for } i = 2, 3, 4, \ldots, M-1 \tag{2.30b}$$

$$H_{x,i}^{Total} \cong H_{x,i}^{f1} + H_{x,i}^{b1} + H_{x,i}^{f2} + H_{x,i}^{b2}, \quad \text{for } i = 2, 3, 4, \ldots, M-1 \tag{2.30c}$$

In region M: $$E_{y,M}^{Total} \cong E_{y,M}^{f1} + E_{y,M}^{f2},\ H_{x,M}^{Total} \cong H_{x,M}^{f1} + H_{x,M}^{f2} \tag{2.30d}$$

It is understood in the above equations that, for the forward progression, the partial fields in the region of interest contain constituents that are due to forward scattering from the left boundary plane and backward scattering from the right boundary plane, e.g. in region 2, $E_{y2}^{f1} = E_{y2}^{f1}\big|_{S_1} + E_{y2}^{f1}\big|_{S_2}$ and similarly for backward progression $E_{y2}^{b1} = E_{y2}^{b1}\big|_{S_1} + E_{y2}^{b1}\big|_{S_2}$, where the subscripts S_1 and S_2 identify step discontinuities where partial fields are scattered. The accuracy of the total field will depend on how many forward and backward partial fields are included in the final results. The iteration process converges well. The numerical evaluations have shown that the inclusion of the four partial fields, as assumed in (2.30), provides acceptable accuracy in most cases.

To clarify the formulation of the backward partial fields, for example, consider regions 3 ($\Delta z \le z \le 2\Delta z$) located between boundary plane S_2 and S_3 as shown in Figure 2.2. To obtain the incident wave fields at S_2, two contributions from scattering

events that occurred at S_3 are needed. The first event is that of the "$f1$" wave fields scattered in the backward direction, i.e., R_{30}^{f1} and $R_3^{f1}(u)$, which were ignored at S_3 during the first forward progression. The second event is that of the "$b1$" wave fields transferred into region 3 due to scattering at S_3, i.e., T_{30}^{b1} and $T_3^{b1}(u)$, during the first backward progression. On reaching S_2, these two contributions experience phase shifts since they transverse the distance Δz in going from S_3 to S_2. Thus, the total incident backgoing guided mode and radiation modes at S_2 have amplitudes $B_{2,0}^{b1}$ and $B_2^{b1}(u)$ given by (2.32a) and (2.32b) for $i=2$. At S_2, reflected waves of amplitudes R_{20}^{b1} and $R_2^{b1}(u)$ are established in region 3 and transmitted waves of amplitudes T_{20}^{b1} and $T_{20}^{b1}(u)$ enter region 2. The partial fields in region 2 due to scattering at S_2 is then seen to be given by (2.33) for $i=2$ and $p=1$.

For the p^{th} backward progression, the partial fields in region $i+1$ ($z_i < z < z_{i+1}$), $i = 1, 2, 3, \ldots, M-2$, take the forms of

$$E_{y,i+1}^{b,p} = \frac{k_0}{\beta_{i+1,0}}[R_{i,0}^{b,p} e^{-j\beta_{i+1,0}z^{(i-1)}} + B_{i,0}^{b,p} e^{j\beta_{i+1,0}z^{(i-1)}}]\Phi_{i+1,0}(x)$$

$$+ \int_{u=0}^{\infty} \frac{k_0}{\beta(u)}[R_i^{b,p}(u) e^{-j\beta(u)z^{(i-1)}} + B_i^{b,p}(u) e^{j\beta(u)z^{(i-1)}}]\Phi_{i+1}(x,u)du \qquad (2.31a)$$

and

$$\eta_0 H_{x,i+1}^{b,p} = -[R_{i,0}^{b,p} e^{-j\beta_{i+1,0}z^{(i-1)}} - B_{i,0}^{b,p} e^{j\beta_{i+1,0}z^{(i-1)}}]\Phi_{i+1,0}(x)$$

$$- \int_{u=0}^{\infty}[R_i^{b,p}(u) e^{-j\beta(u)z^{(i-1)}} - B_i^{b,p}(u) e^{j\beta(u)z^{(i-1)}}]\Phi_{i+1}(x,u)du \qquad (2.31b)$$

with

$$z^{(i-1)} = z - z_i \qquad (2.31c)$$

where superscript "*b,p*" identifies the p^{th} backward partial field contributions to the rigorous field solution. The amplitudes of incident surface wave and radiation waves for discontinuity plane S_i are given, respectively, by

$$B_{i,0}^{b,p} = \begin{cases} [T_{i+1,0}^{b,p} + R_{i+1,0}^{f,p}]e^{-j\beta_{i+1,0}\Delta z}, & \text{for } i = 1, 2, 3, ..., M-3 \\ R_{i+1,0}^{f,p} e^{-j\beta_{i+1,0}\Delta z}, & \text{for } i = M-2 \end{cases} \tag{2.32a}$$

and

$$B_i^{b,p}(u) = \begin{cases} [T_{i+1}^{b,p}(u) + R_{i+1}^{f,p}(u)]e^{-j\beta(u)\Delta z}, & \text{for } i = 1, 2, 3, ..., M-3 \\ R_{i+1}^{f,p}(u)e^{-j\beta(u)\Delta z}, & \text{for } i = M-2 \end{cases} \tag{2.32b}$$

where

$$\Delta z = z_{i+1} - z_i \tag{2.32c}$$

The partial fields in region i, i = 1, 2, 3,..., $M-2$, established by scattering at step discontinuity S_i are

$$E_{y,i}^{b,p} = \frac{k_0}{\beta_{i,0}} T_{i,0}^{b,p} e^{j\beta_{i,0}z^{(i-1)}} \Phi_{i,0}(x) + \int_{u=0}^{\infty} \frac{k_0}{\beta(u)} T_i^{b,p}(u) e^{j\beta(u)z^{(i-1)}} \Phi_i(x,u)du \tag{2.33a}$$

and

$$\eta_0 H_{x,i}^{b,p} = T_{i,0}^{b,p} e^{j\beta_{i,0}z^{(i-1)}} \Phi_{i,0}(x) + \int_{u=0}^{\infty} T_i^{b,p}(u) e^{j\beta(u)z^{(i-1)}} \Phi_i(x,u)du \tag{2.33b}$$

By utilizing boundary condition (2.9) at plane S_i, multiplying $\Phi_{i+1,0}(x)$ and $\Phi_{i+1}(x,u')$ to both sides of the equations, using orthogonality relations (2.7), arranging equations in the same fashion as that of forward progression and adopting normalized parameters (2.25), the system of equations is obtained for backward progression at S_i, i = 1, 2, 3,..., $M-2$,

$$R_{i,0}^{b,p} + \overline{Q}_{0,0}(\overline{D}_i, \overline{D}_{i+1}) T_{i,0}^{b,p} + \int_{\overline{u}=0}^{\infty} \overline{Q}_0'(\overline{u}; \overline{D}_i, \overline{D}_{i+1}) \overline{T}_i^{b,p}(\overline{u}) d\overline{u} = B_{i,0}^{b,p} \tag{2.34a}$$

$$2R_{i,0}^{b,p} + [1 - \frac{\overline{\beta}_{i+1,0}}{\overline{\beta}_{i,0}}] \overline{Q}_{0,0}(\overline{D}_i, \overline{D}_{i+1}) T_{i,0}^{b,p} + \int_{\overline{u}=0}^{\infty} [1 - \frac{\overline{\beta}_{i+1,0}}{\overline{\beta}(\overline{u})}] \overline{Q}_0'(\overline{u}; \overline{D}_i, \overline{D}_{i+1}) \overline{T}_i^{b,p}(\overline{u}) d\overline{u} = 0 \tag{2.34b}$$

$$\begin{aligned} &\overline{Q}_0(\overline{u}'; \overline{D}_i, \overline{D}_{i+1}) T_{i,0}^{b,p} + \overline{Q}_1(\overline{u}'; \overline{D}_i, \overline{D}_{i+1}) \overline{T}_i^{b,p}(\overline{u} = \overline{u}') \\ &+ \int_{\overline{u}=0}^{\infty} [-\frac{\overline{Q}_2'(\overline{u}', \overline{u}; \overline{D}_i, \overline{D}_{i+1})}{\overline{u}'^2 - \overline{u}^2} + \overline{Q}_3'(\overline{u}', \overline{u}; \overline{D}_i, \overline{D}_{i+1})] \overline{T}_i^{b,p}(\overline{u}) d\overline{u} \\ &+ \overline{R}_i^{b,p}(\overline{u} = \overline{u}') = \overline{B}_i^{b,p}(u = u') \end{aligned} \tag{2.34c}$$

$$\begin{aligned} &[1 - \frac{\overline{\beta}(\overline{u}')}{\overline{\beta}_{i,0}}] \overline{Q}_0(\overline{u}'; \overline{D}_i, \overline{D}_{i+1}) T_{i,0}^{b,p} - \int_{\overline{u}=0}^{\infty} \frac{\overline{Q}_2'(\overline{u}', \overline{u}; \overline{D}_i, \overline{D}_{i+1})}{\overline{\beta}(\overline{u})[\overline{\beta}(\overline{u}) + \overline{\beta}(\overline{u}')]} \overline{T}_i^{b,p}(\overline{u}) d\overline{u} \\ &+ \int_{\overline{u}=0}^{\infty} [1 - \frac{\overline{\beta}(\overline{u}')}{\overline{\beta}(\overline{u})}] \overline{Q}_3'(\overline{u}', \overline{u}; \overline{D}_i, \overline{D}_{i+1})] \overline{T}_i^{b,p}(\overline{u}) d\overline{u} + 2\overline{R}_i^{b,p}(\overline{u} = \overline{u}') = 0, \\ &\qquad \text{for } \overline{u}' \neq \overline{k}_0 \end{aligned} \tag{2.34d}$$

$$e^{-j(\overline{\zeta}_{i+1} - \overline{\zeta}_i)} \overline{T}_i^{b,p}(\overline{u} = \overline{k}_0) - \overline{R}_i^{b,p}(\overline{u} = \overline{k}_0) = \overline{B}_i^{b,p}(\overline{u} = \overline{k}_0), \quad \text{for } \overline{u}' = \overline{k}_0 \tag{2.34e}$$

where

$$\overline{\zeta}_i = \overline{D}_i - \tan^{-1}[\varepsilon_r^{\frac{1}{2}} \tan(\overline{k}\overline{D}_i)], \; \overline{\zeta}_{i+1} = \overline{D}_{i+1} - \tan^{-1}[\varepsilon_r^{\frac{1}{2}} \tan(\overline{k}\overline{D}_{i+1})] \tag{2.34f}$$

$$B_{i,0}^{b,p} = \begin{cases} [T_{i+1,0}^{b,p} + R_{i+1,0}^{f,p}] e^{-j\overline{\beta}_{i+1,0}\Delta\overline{z}}, & \text{for } i = 1, 2, 3, \ldots, M-3 \\ R_{i+1,0}^{f,p} e^{-j\overline{\beta}_{i+1,0}\Delta\overline{z}}, & \text{for } i = M-2 \end{cases} \tag{2.34g}$$

$$\overline{B}_i^{b,p}(\overline{u}) = \begin{cases} [\overline{T}_{i+1}^{b,p}(\overline{u}) + \overline{R}_{i+1}^{f,p}(\overline{u})] e^{-j\overline{\beta}(\overline{u})\Delta\overline{z}}, & \text{for } i = 1, 2, 3, \ldots, M-3 \\ \overline{R}_{i+1}^{f,p}(\overline{u}) e^{-j\overline{\beta}(\overline{u})\Delta\overline{z}}, & \text{for } i = M-2 \end{cases} \tag{2.34h}$$

$$\Delta\overline{z} = \overline{z}_{i+1} - \overline{z}_i \tag{2.34i}$$

$$\overline{Q}_2'(\overline{u}', \overline{u}; \overline{D}_i, \overline{D}_{i+1}) = \overline{Q}_2(\overline{u}, \overline{u}'; \overline{D}_i, \overline{D}_{i+1}) \tag{2.34j}$$

$$\overline{Q}_3'(\overline{u}', \overline{u}; \overline{D}_i, \overline{D}_{i+1}) = \overline{Q}_3(\overline{u}, \overline{u}'; \overline{D}_i, \overline{D}_{i+1}) \tag{2.34k}$$

Similar to forward progression, there is no occurrence of scattering radiation wave for $\bar{u} = 0$ at discontinuity plane S_i, $i = 1, 2, 3, \ldots, M-2$. Hence,

$$\bar{R}_i^{b,p}(\bar{u} = 0) = \bar{T}_i^{b,p}(\bar{u} = 0) = 0, \quad \text{for } i = 1, 2, 3, \ldots, M-2 \tag{2.35}$$

Imposing (2.35) to (2.34a)-(2.34d), the discretization process and singular integral evaluation provide the set of $2N+2$ linear equations with $2N+2$ unknowns, i.e., $R_{i,0}^{b,p}$, $T_{i,0}^{b,p}$, $\bar{R}_i^{b,p}(\bar{u} = \bar{u}_m)$ and $\bar{T}_i^{b,p}(\bar{u} = \bar{u}_m)$, $m = 1, 2, 3, \ldots, N$.

The question may be asked why the above mode-matching and iteration procedure were chosen. As pointed out above, the procedure involves formulation of the mode-matching problem at the step transition planes in terms of a linear system akin to a scatter matrix representation of the problem. An alternate approach would consist in formulating the mode-matching problem in terms of voltage-current transmission matrices which in the overall antenna problem are then interspersed by the (diagonal) transmission line matrices of the uniform dielectric guide sections of the staircase model [19]. The advantage of this approach is that it reduces the antenna problem to the cascading of M_S mode-matching matrices of the relatively moderate size $N_m \times N_m$, where $M_S = M - 1$ is the number of step transition planes in the staircase model of the antenna and $N_m = 2N + 4$ is the number of modes considered at each step. In other words, the antenna problem in this formulation is reduced to a sequence of matrix multiplications. An added advantage is that formulation of the boundary conditions (2.9) in this case provides the coefficients of the voltage-current transmission matrices

explicitly, i.e., without the need for additional matrix operations of the type required in calculating the scattering matrix representation of the step discontinuities; see footnote 1. The method has the advantage of numerical efficiency; but it also has a problem, that of stability.

Despite these advantages the method was not used here because it is likely to lead to a stability problem. It will be stable as long as it can be assumed that the coupling between adjacent transition planes is accomplished solely by the propagating modes traveling on the interconnecting uniform guide sections, which means that in the transmission line matrices all evanescent modes can be neglected. However, for the slab/wedge antenna, the mode-matching planes are in close proximity, coupling by evanescent modes cannot be disregarded a priori, and as a result the procedure is likely to become unstable. This has to do with the fact that on the uniform guide sections, there are two groups of waves, one propagating to the right and the other one to the left. Hence, as one proceeds from boundary plane S_i to plane S_{i+1}, the evanescent modes of one of these groups will exponentially increase in amplitude and any error in the mode-matching procedure in plane S_i is likely to be amplified in plane S_{i+1}, and become even bigger in plane S_{i+2}; hence, the procedure destabilizes.

For this reason, the mode-matching procedure in the step transition planes is formulated in terms of generalized scattering matrices [20], [21]. This has the advantage that as one formulates the coupling between planes S_i and S_{i+1} in terms of the two mode groups traveling on the interconnecting uniform guide sections, one follows either group in its respective direction of propagation and all evanescent modes will exponentially decrease in amplitude, thus eliminating the cause for instability.

In the dissertation, the problem has been resolved by the iteration procedure discussed above. This, in effect, reduces the determination of the cascading of M_S matrices of size $N_m \times N_m$ to solving a single $N_m \times N_m$ matrix equation at each boundary plane whether progressing in the forward or backward direction. The procedure is stable, though it needs to be repeated several times.

2.4 Antenna Characteristics

With the mode amplitudes of the antenna field known in the first and the M^{th} regions of the staircase model, the determination of the antenna characteristics, including its reflection coefficient, radiation intensity, radiated power and directive gain, is straight forward.

The reflection coefficient, which determines the VSWR on the feed guide, is given by

$$\Gamma = [R_{10}^{f1} + \sum_{p=1}^{N_b} T_{10}^{b,p}] \Big/ A_{10}^{f1} \tag{2.36}$$

where $T_{10}^{b,p}$ are the mode amplitudes of the p^{th} order backward going surface waves at the discontinuity plane S_1 in the feed waveguide (region 1). The parameter N_b is the total number of backward progressions.

The radiation intensity is calculated by asymptotic evaluation of the electric fields in the free space region $i = M$ off the tip of the antenna (forward-range pattern) and in

the feed guide region $i = 1$ (backward-range pattern). By using the method of stationary phase [22], [23], the radiation intensity is obtained as follows (see Appendix F):

$$U(\theta) = \begin{cases} \dfrac{1}{2\eta_0}\left|\overline{T}_f(\sin\theta)\right|^2, & \text{for } 0 \le \theta \le \dfrac{\pi}{2} \\ \dfrac{1}{2\eta_0}\left|\overline{R}_b(\sin\theta)\right|^2, & \text{for } \dfrac{\pi}{2} \le \theta \le \pi \end{cases} \tag{2.37}$$

while $U(-\theta) = U(\theta)$. Angle θ is the elevation angle measured with respective to the $+z$ axis. The amplitudes $\overline{T}_f(\sin\theta)$ and $\overline{R}_b(\sin\theta)$ are, respectively, given by the composition of N_f and N_b orders of mode amplitudes

$$\overline{T}_f(\sin\theta) = \sum_{p=1}^{N_f} \overline{T}_{M-1}^{f,p}(\sin\theta) \tag{2.38a}$$

and

$$\overline{R}_b(\sin\theta) = \overline{R}_1^{f1}(\sin\theta) + \sum_{p=1}^{N_b} \overline{T}_1^{b,p}(\sin\theta) \tag{2.38b}$$

where N_f is total number of forward progressions ($N_f = N_b = 2$ in (2.30)).

The radiated power, which is given by integrating the radiation intensity (2.37) over 2π radians (from $-\pi$ to π), can be found from a series approximation

$$P^{RAD} = 2\int_{\theta=0}^{\pi} U(\theta)d\theta = \frac{1}{\eta_0}\left[\int_{\theta=0}^{\pi/2}\left|\overline{T}_f(\sin\theta)\right|^2 d\theta + \int_{\pi/2}^{\pi}\left|\overline{R}_b(\sin\theta)\right|^2 d\theta\right] \tag{2.39a}$$

$$\cong \frac{1}{\eta_0}\left[\sum_{m=0}^{N'}\left|\overline{T}_f(\sin\theta_{f,m})\right|^2 \Delta\theta_{f,m} + \sum_{m=1}^{N'}\left|\overline{R}_b(\sin\theta_{b,m})\right|^2 \Delta\theta_{b,m}\right] \tag{2.39b}$$

where

$$\theta_{f,m} = \sin^{-1}(\bar{u}_m),\ \theta_{b,m} = \pi - \sin^{-1}(\bar{u}_m) \tag{2.39c}$$

$$\bar{u}_{N'} = \bar{k}_0 = 1,\ \sin^{-1}(\bar{u}_{N'}) = \pi/2 \tag{2.39d}$$

$$\Delta\theta_{f,m} = \begin{cases} \theta_{f,m+1}/2, & \text{for } m = 0 \\ \pi/2 - (\theta_{f,m} + \theta_{f,m-1})/2, & \text{for } m = N' \\ (\theta_{f,m+1} - \theta_{f,m-1})/2, & \text{elsewhere} \end{cases} \tag{2.39e}$$

$$\Delta\theta_{b,m} = \begin{cases} (\theta_{f,m-1} + \theta_{f,m})/2 - \pi/2, & \text{for } m = N' \\ (\theta_{f,m-1} - \theta_{f,m+1})/2, & \text{elsewhere} \end{cases} \tag{2.39f}$$

Directive gain is defined as the ratio of the radiation intensity in a given direction to the average radiation intensity [24], [25], or

$$D(\theta) = \frac{U(\theta)}{U_{ave}} = \frac{2\pi U(\theta)}{P^{RAD}} \tag{2.40}$$

while $D(-\theta) = D(\theta)$.

CHAPTER 3

TM FORMULATION

The model for the tapered dielectric antenna fed by a slab waveguide is depicted in Figure 2.1, wherein the smooth tapered portion is replaced by short slab segments of equal length and uniform cross-sectional areas.

3.1 TM Modal Representation

An even TM surface wave mode (of lowest order) of the uniform dielectric slab waveguide is assumed to be incident in the +z direction from $z \to -\infty$ and to excite the dielectric wedge antenna. This mode does not experience cutoff and can propagate along very thin slab waveguides. Due to this excitation and the antenna geometry, the field in each slab region i is everywhere independent of the y-coordinate and is TM polarized with field components $H_{y,i}$, $E_{x,i}$ and $E_{z,i}$.

Using the known even TM mode structure of the dielectric slab waveguide [12], [17], [18], each field component in each region occupied by a slab is represented by a finite, discrete spectrum of allowable surface wave modes and an infinite spectrum of radiation modes

$$\eta_0 H_{y,i} = \sum_{n=0}^{N_m^{TM}} i_{i,n}(z)\Psi_{i,n}(x) + \int_{u=0}^{\infty} i_i(z,u)\Psi_i(x,u)du \tag{3.1a}$$

$$E_{x,i} = \frac{1}{\varepsilon_{r,i}(x)} \sum_{n=0}^{N_m^{TM}} v_{i,n}(z)\Psi_{i,n}(x) + \frac{1}{\varepsilon_{r,i}(x)} \int_{u=0}^{\infty} v_i(z,u)\Psi_i(x,u)du \tag{3.1b}$$

$$E_{z,i} = \frac{1}{\varepsilon_{r,i}(x)} \frac{1}{jk_0} \frac{\partial \eta_0 H_{y,i}}{\partial x} \tag{3.1c}$$

where $\varepsilon_{r,i}(x)$ is unity in free space, but equals ε_r in the dielectric. The numerical index n is the mode order for the TM surface wave modes, with N_m^{TM} being the highest one. Assuming a time dependence of $e^{j\omega t}$, the z-dependent expansion coefficients in (3.1) with prescribed normalizations are taken to be given by

$$i_{i,n}(z) = \frac{k_0}{\beta_{i,n}} [A_{i,n} e^{-j\beta_{i,n} z} - B_{i,n} e^{j\beta_{i,n} z}] \tag{3.2a}$$

$$i_i(z,u) = \frac{k_0}{\beta(u)} [A_i(u) e^{-j\beta(u) z} - B_i(u) e^{j\beta(u) z}] \tag{3.2b}$$

$$v_{i,n}(z) = -\frac{1}{jk_0} \frac{di_{i,n}(z)}{dz}, \quad v_i(z,u) = -\frac{1}{jk_0} \frac{\partial i_i(z,u)}{\partial z} \tag{3.2c}$$

where $A_{i,n}$, $A_i(u)$ are the amplitudes of the $+z$ traveling modes and $B_{i,n}$, $B_i(u)$ are those of the $-z$ traveling modes. The TM mode functions $\Psi_i(x)$ and $\Psi_i(x,u)$ in (3.1) determine the x-dependence of the modes and are given by

$$\Psi_{i,n}(x) = \begin{cases} C_{i,n} \cos(k_{x,i,n} x), & |x| \le D_i \\ C_{i,n} \cos(k_{x,i,n} D_i) e^{-\alpha_{x,i,n}(|x| - D_i)}, & |x| > D_i \end{cases} \tag{3.3a}$$

with

$$C_{i,n} = \left[\frac{2\alpha_{x,i,n}}{\dfrac{k_{x,i,n}^2 + \alpha_{x,i,n}^2}{k_{x,i,n}^2 + \varepsilon_r^2 \alpha_{x,i,n}^2} + \alpha_{x,i,n} \dfrac{D_i}{\varepsilon_r}} \right]^{\frac{1}{2}} \tag{3.3b}$$

and

$$\Psi_i(x,u)=\begin{cases} C_i(u)\cos(vx), & |x|\le D_i \\ C_i(u)\{\cos(vD_i)\cos[u(|x|-D_i)]-\dfrac{v}{\varepsilon_r u}\sin(vD_i)\sin[u(|x|-D_i)]\}, & |x|>D_i \end{cases} \tag{3.4a}$$

with

$$C_i(u)=\{\frac{\pi}{2}[\cos^2(vD_i)+(\frac{v}{\varepsilon_r u})^2\sin^2(vD_i)]\}^{-\frac{1}{2}} \tag{3.4b}$$

$$v=[k^2-k_0^2+u^2]^{\frac{1}{2}} \tag{3.4c}$$

For the TM surface wave modes, the propagation constants $\beta_{i,n}$ depend on the slab width D_i and are determined by the dispersion relation

$$k_{x,i,n}\tan(k_{x,i,n}D_i)=\varepsilon_r\alpha_{x,i,n} \tag{3.5}$$

For any D_i, this equation has a finite number of real solutions that lie within the range $k_0<\beta_{i,n}<k$. The propagation constants $\beta(u)$ of the radiation modes are independent of D_i and are given by (2.6).

With the expressions (3.3) and (3.4), the mode functions satisfy the orthogonality relations

$$\int_{x=0}^{\infty}\frac{1}{\varepsilon_{r,i}(x)}\Psi_{i,m}(x)\Psi_{i,n}(x)dx=\delta_{mn} \tag{3.6a}$$

$$\int_{x=0}^{\infty}\frac{1}{\varepsilon_{r,i}(x)}\Psi_i(x,u)\Psi_i(x,u')dx=\delta(u-u') \tag{3.6b}$$

$$\int_{x=0}^{\infty} \frac{1}{\varepsilon_{r,i}(x)} \Psi_{i,n}(x)\Psi_i(x,u)dx = 0 \tag{3.6c}$$

In the following, D_1 is chosen to satisfy (2.8) to insure that all slabs support only the lowest order TM surface wave mode, which does not have a cutoff frequency. Hence, in the discussion to follow, the summations in (3.1) reduce to single terms with mode index $n = 0$. In addition, the longitudinal component $E_{z,i}$ is not discussed since the transverse components $E_{x,i}$, $H_{y,i}$ and the boundary conditions characterize the field completely. Thus, (3.1)-(3.5) describe the field in each region filled by a dielectric slab segment of the slab waveguide/wedge antenna, i.e., in the regions between the step transition planes S_1, S_2, S_3,..., S_{M-1}, whereas, the step transitions in these planes are characterized by the boundary conditions

$$H_{y,i}(x,z_i) = H_{y,i+1}(x,z_i), \quad -\infty < x < +\infty, \quad i = 1, 2,..., M-1 \tag{3.7a}$$

and

$$E_{x,i}(x,z_i) = E_{x,i+1}(x,z_i), \quad -\infty < x < +\infty, \quad i = 1, 2,..., M-1 \tag{3.7b}$$

Following the procedure developed in Chapter 2, the boundary conditions (3.7) are formulated in terms of the modal representations (3.1) that, after discretizing and truncating the continuous spectrum of radiation modes, yield a linear system at each plane S_i that relates the amplitudes of the incident modes, be the surface or radiation, to the modes scattered from the transition plane. The method is computationally efficient because of a mode-matching algorithm which constructs and solves the linear system at

each transition plane. In this way, the required matrix calculations needed and the size of the matrices involved are minimized. The fields in any slab region are then determined to any order of accuracy by an iterative scheme which involves forward and backward partial wave fields.

3.2 TM Mode-Matching of Partial Wave Fields at a Step Transition Plane

In general, if the scattering event is considered for the p^{th} forward progression at a step discontinuity in the transition plane S_i located at $z = z_i$, the partial transverse field constituents in region i to the left of S_i take the forms

$$\eta_0 H_{y,i}^{f,p} = \frac{k_0}{\beta_{i,0}}[A_{i,0}^{f,p} e^{-j\beta_{i,0} z^{(i-1)}} - R_{i,0}^{f,p} e^{j\beta_{i,0} z^{(i-1)}}]\Psi_{i,0}(x)$$

$$+ \int_{u=0}^{\infty} \frac{k_0}{\beta(u)}[A_i^{f,p}(u) e^{-j\beta(u) z^{(i-1)}} - R_i^{f,p}(u) e^{j\beta(u) z^{(i-1)}}]\Psi_i(x,u)du \qquad (3.8a)$$

and

$$E_{x,i}^{f,p} = \frac{1}{\varepsilon_{r,i}(x)}[A_{i,0}^{f,p} e^{-j\beta_{i,0} z^{(i-1)}} + R_{i,0}^{f,p} e^{j\beta_{i,0} z^{(i-1)}}]\Psi_{i,0}(x)$$

$$+ \frac{1}{\varepsilon_{r,i}(x)} \int_{u=0}^{\infty} [A_i^{f,p}(u) e^{-j\beta(u) z^{(i-1)}} + R_i^{f,p}(u) e^{j\beta(u) z^{(i-1)}}]\Psi_i(x,u)du \qquad (3.8b)$$

where

$$z^{(i-1)} = z - z_i \qquad (3.8c)$$

$$i = \begin{cases} 1, 2, 3, \ldots, M-1, & \text{for } p = 1 \\ 2, 3, 4, \ldots, M-1, & \text{for } p > 1 \end{cases} \qquad (3.8d)$$

The amplitudes of the incident surface wave $A_{i,0}^{f,p}$ and radiation waves $A_i^{f,p}(u)$, $0 \le u < \infty$, at the discontinuity plane S_i are given, respectively, by

$$A_{i,0}^{f,p} = \begin{cases} [\eta_0 \beta_{10}/k_0]^{\frac{1}{2}}, & \text{for } i = 1 \text{ and } p = 1 \\ T_{i-1,0}^{f,p} e^{-j\beta_{i,0}\Delta z}, & \text{for } i = 2, 3, 4, \ldots, M-1 \text{ and } p = 1 \\ R_{10}^{b,p-1} e^{-j\beta_{i,0}\Delta z}, & \text{for } i = 2 \text{ and } p > 1 \\ [T_{i-1,0}^{f,p} + R_{i-1,0}^{b,p-1}] e^{-j\beta_{i,0}\Delta z}, & \text{for } i = 3, 4, 5, \ldots, M-1 \text{ and } p > 1 \end{cases} \tag{3.9a}$$

$$A_i^{f,p}(u) = \begin{cases} 0, & \text{for } i = 1 \text{ and } p = 1 \\ T_{i-1}^{f,p}(u) e^{-j\beta(u)\Delta z}, & \text{for } i = 2, 3, 4, \ldots, M-1 \text{ and } p = 1 \\ R_1^{b,p-1}(u) e^{-j\beta(u)\Delta z}, & \text{for } i = 2 \text{ and } p > 1 \\ [T_{i-1}^{f,p}(u) + R_{i-1}^{b,p-1}(u)] e^{-j\beta(u)\Delta z}, & \text{for } i = 3, 4, 5, \ldots, M-1 \text{ and } p > 1 \end{cases} \tag{3.9b}$$

$$\Delta z = z_i - z_{i-1} \tag{3.9c}$$

It is assumed that the antenna is fed by a single even TM surface wave of unity power; hence, $A_{10}^{f1} = [\eta_0 \beta_{10}/k_0]^{\frac{1}{2}}$. For the p^{th} forward progression, the partial transverse field constituents in the region $i+1$ to the right of S_i, established from scattering at the step discontinuity S_i, are given by

$$\eta_0 H_{y,i+1}^{f,p} = \frac{k_0}{\beta_{i+1,0}} T_{i,0}^{f,p} e^{-j\beta_{i+1,0} z^{(i-1)}} \Psi_{i+1,0}(x) + \int_{u=0}^{\infty} \frac{k_0}{\beta(u)} T_i^{f,p}(u) e^{-j\beta(u) z^{(i-1)}} \Psi_{i+1}(x,u) du \tag{3.10a}$$

and

$$E_{x,i+1}^{f,p} = \frac{1}{\varepsilon_{r,i+1}(x)} T_{i,0}^{f,p} e^{-j\beta_{i+1,0} z^{(i-1)}} \Psi_{i+1,0}(x) + \frac{1}{\varepsilon_{r,i+1}(x)} \int_{u=0}^{\infty} T_i^{f,p}(u) e^{-j\beta(u) z^{(i-1)}} \Psi_{i+1}(x,u) du \tag{3.10b}$$

The subscript "*i*" on the mode amplitudes identifies the transition plane S_i where scattering occurs. Other than for the mode amplitudes, the subscripts "*i*" and "$i+1$"

define the regions where the partial fields exist; the superscript "*f,p*" identifies the p^{th} forward partial field contributions to the rigorous field solution.

The unknown mode amplitudes $R_{i,0}^{f,p}$, $T_{i,0}^{f,p}$, $R_i^{f,p}(u)$ and $T_i^{f,p}(u)$ at each step discontinuity are determined by the mode-matching method. This involves requiring that the total tangential components of the magnetic and electric fields are continuous across the step discontinuity plane S_i,

$$H_{y,i}^{f,p}(x, z^{(i-1)} = 0) = H_{y,i+1}^{f,p}(x, z^{(i-1)} = 0) \tag{3.11a}$$

and

$$E_{x,i}^{f,p}(x, z^{(i-1)} = 0) = E_{x,i+1}^{f,p}(x, z^{(i-1)} = 0) \tag{3.11b}$$

The above continuity requirements yield the following equations:

$$\frac{1}{\beta_{i,0}}[A_{i,0}^{f,p} - R_{i,0}^{f,p}]\Psi_{i,0}(x) + \int_{u=0}^{\infty} \frac{1}{\beta(u)}[A_i^{f,p}(u) - R_i^{f,p}(u)]\Psi_i(x,u)du$$

$$= \frac{1}{\beta_{i+1,0}} T_{i,0}^{f,p}\Psi_{i+1,0}(x) + \int_{u=0}^{\infty} \frac{1}{\beta(u)} T_i^{f,p}(u)\Psi_{i+1}(x,u)du \tag{3.12a}$$

and

$$\frac{1}{\varepsilon_{r,i}(x)}[A_{i,0}^{f,p} + R_{i,0}^{f,p}]\Psi_{i,0}(x) + \frac{1}{\varepsilon_{r,i}(x)} \int_{u=0}^{\infty} [A_i^{f,p}(u) + R_i^{f,p}(u)]\Psi_i(x,u)du$$

$$= \frac{1}{\varepsilon_{r,i+1}(x)} T_{i,0}^{f,p}\Psi_{i+1,0}(x) + \frac{1}{\varepsilon_{r,i+1}(x)} \int_{u=0}^{\infty} T_i^{f,p}(u)\Psi_{i+1}(u)du \tag{3.12b}$$

Multiplying both sides of (3.12a) and (3.12b), respectively, by $[1/\varepsilon_{r,i}(x)]\Psi_{i,0}(x)$ and $\Psi_{i,0}(x)$, integrating over x for 0 to ∞, interchanging the order of integration over u and x

and using the orthogonality relations in (3.6a) and (3.6c) lead to the following equations, respectively:

$$A_{i,0}^{f,p} - R_{i,0}^{f,p} = \frac{\beta_{i,0}}{\beta_{i+1,0}} M_{0,0}^{(i)}(D_i, D_{i+1}) T_{i,0}^{f,p} + \int_{u=0}^{\infty} \frac{\beta_{i,0}}{\beta(u)} M_0^{(i)}(u; D_i, D_{i+1}) T_i^{f,p}(u) du \tag{3.13a}$$

and

$$A_{i,0}^{f,p} + R_{i,0}^{f,p} = M_{0,0}^{(i+1)}(D_i, D_{i+1}) T_{i,0}^{f,p} + \int_{u=0}^{\infty} M_0^{(i+1)}(u; D_i, D_{i+1}) T_i^{f,p}(u) du \tag{3.13b}$$

where

$$M_{0,0}^{(i)}(D_i, D_{i+1}) = \int_{x=0}^{\infty} \frac{1}{\varepsilon_{r,i}(x)} \Psi_{i,0}(x) \Psi_{i+1,0}(x) dx \tag{3.13c}$$

$$M_{0,0}^{(i+1)}(D_i, D_{i+1}) = \int_{x=0}^{\infty} \frac{1}{\varepsilon_{r,i+1}(x)} \Psi_{i,0}(x) \Psi_{i+1,0}(x) dx \tag{3.13d}$$

$$M_0^{(i)}(u; D_i, D_{i+1}) = \int_{x=0}^{\infty} \frac{1}{\varepsilon_{r,i}(x)} \Psi_{i,0}(x) \Psi_{i+1}(x,u) dx \tag{3.13e}$$

$$M_0^{(i+1)}(u; D_i, D_{i+1}) = \int_{x=0}^{\infty} \frac{1}{\varepsilon_{r,i+1}(x)} \Psi_{i,0}(x) \Psi_{i+1}(x,u) dx \tag{3.13f}$$

The explicit form of the overlap integrals $M_{0,0}^{(i)}(D_i, D_{i+1})$, $M_{0,0}^{(i+1)}(D_i, D_{i+1})$, $M_0^{(i)}(u; D_i, D_{i+1})$ and $M_0^{(i+1)}(u; D_i, D_{i+1})$ are shown in Appendix D. Subtracting (3.13a) from (3.13b) gives

$$\begin{aligned} 2R_{i,0}^{f,p} = & [M_{0,0}^{(i+1)}(D_i, D_{i+1}) - \frac{\beta_{i,0}}{\beta_{i+1,0}} M_{0,0}^{(i)}(D_i, D_{i+1})] T_{i,0}^{f,p} \\ & + \int_{u=0}^{\infty} [M_0^{(i+1)}(u; D_i, D_{i+1}) - \frac{\beta_{i,0}}{\beta_{i+1}(u)} M_0^{(i)}(u; D_i, D_{i+1})] T_i^{f,p}(u) du \end{aligned} \tag{3.14}$$

Additional equations are obtained by multiplying both sides of (3.12a) and (3.12b), respectively, by $[1/\varepsilon_{r,i}(x)]\Psi_i(x,u')$ and $\Psi_i(x,u')$, integrating over x from 0 to ∞ and using the orthogonality relations in (3.6b) and (3.6c) to yield

$$A_i^{f,p}(u=u') - R_i^{f,p}(u=u') = \frac{\beta(u')}{\beta_{i+1,0}} M_0'^{(i)}(u'; D_i, D_{i+1}) T_{i,0}^{f,p} + \int_{u=0}^{\infty} \frac{\beta(u')}{\beta(u)} M^{(i)}(u',u; D_i, D_{i+1}) T_i^{f,p}(u)du \tag{3.15a}$$

and

$$A_i^{f,p}(u=u') + R_i^{f,p}(u=u') = M_0'^{(i+1)}(u'; D_i, D_{i+1}) T_{i,0}^{f,p} + \int_{u=0}^{\infty} M^{(i+1)}(u',u; D_i, D_{i+1}) T_i^{f,p}(u)du \tag{3.15b}$$

where

$$M^{(i)}(u',u; D_i, D_{i+1}) = \int_{x=0}^{\infty} \frac{1}{\varepsilon_{r,i}(x)} \Psi_i(x,u')\Psi_{i+1}(x,u)dx \tag{3.15c}$$

$$M^{(i+1)}(u',u; D_i, D_{i+1}) = \int_{x=0}^{\infty} \frac{1}{\varepsilon_{r,i+1}(x)} \Psi_i(x,u')\Psi_{i+1}(x,u)dx \tag{3.15d}$$

$$M_0'^{(i)}(u; D_i, D_{i+1}) = \int_{x=0}^{\infty} \frac{1}{\varepsilon_{r,i}(x)} \Psi_i(x,u)\Psi_{i+1,0}(x)dx \tag{3.15e}$$

$$M_0'^{(i+1)}(u; D_i, D_{i+1}) = \int_{x=0}^{\infty} \frac{1}{\varepsilon_{r,i+1}(x)} \Psi_i(x,u)\Psi_{i+1,0}(x)dx \tag{3.15f}$$

$M^{(i)}(u',u; D_i, D_{i+1})$ and $M^{(i+1)}(u',u; D_i, D_{i+1})$ can be shown to take the following forms (see Appendix D):

$$M^{(i)}(u',u; D_i, D_{i+1}) = M_1(u'; D_i, D_{i+1})\delta(u-u') + \frac{M_2(u',u; D_i, D_{i+1})}{u'^2 - u^2} + M_3^{(i)}(u',u; D_i, D_{i+1}) \tag{3.16a}$$

and

$$M^{(i+1)}(u',u;D_i,D_{i+1}) = M_1(u';D_i,D_{i+1})\delta(u-u') + \frac{M_2(u',u;D_i,D_{i+1})}{u'^2-u^2} + M_3^{(i+1)}(u',u;D_i,D_{i+1}) \tag{3.16b}$$

By using (3.16), (3.15a) and (3.15b) become

$$\frac{\beta(u')}{\beta_{i+1,0}} M_0'^{(i)}(u';D_i,D_{i+1})T_{i,0}^{f,p} + M_1(u';D_i,D_{i+1})T_i^{f,p}(u=u') + \int_{u=0}^{\infty} \frac{\beta(u')}{\beta(u)} \frac{M_2(u',u;D_i,D_{i+1})}{u'^2-u^2} T_i^{f,p}(u)du + \int_{u=0}^{\infty} \frac{\beta(u')}{\beta(u)} M_3^{(i)}(u',u;D_i,D_{i+1})T_i^{f,p}(u)du + R_i^{f,p}(u=u') = A_i^{f,p}(u=u') \tag{3.17a}$$

and

$$M_0'^{(i+1)}(u';D_i,D_{i+1})T_{i,0}^{f,p} + M_1(u';D_i,D_{i+1})T_i^{f,p}(u=u') + \int_{u=0}^{\infty} [\frac{M_2(u',u;D_i,D_{i+1})}{u'^2-u^2} + M_3^{(i+1)}(u',u;D_i,D_{i+1})]T_i^{f,p}(u)du - R_i^{f,p}(u=u') = A_i^{f,p}(u=u') \tag{3.17b}$$

To solve (3.13b), (3.14), (3.17a) and (3.17b), the integrals over x (overlap integral) are first evaluated explicitly. The remaining integrals over u are truncated at $u = u_{\max} > k_0$ and discretized into $N_T^I = N/2$ intervals (N segments). Simpson's one-third rule is used to evaluate integrals in intervals devoid of singularities. The singularities encountered are of three types, namely, $1/\beta(u)$, $1/(u'^2-u^2)$ and

$\beta(u')/[\beta(u)(u'^2-u^2)]$. Similar to the TE case, the integrations across the first two singularities are handled by established methods. The integration over the third singularity, which follows the procedure used to derive (2.20), yields from (3.17a) for $u'=k_0$

$$e^{j(\zeta_{i+1}-\zeta_i)}T_i^{f,p}(u=k_0)+R_i^{f,p}(u=k_0)=A_i^{f,p}(u=k_0),\quad \text{for } u'=k_0 \tag{3.18a}$$

where

$$\zeta_i=k_0D_i-\tan^{-1}[\varepsilon_r^{-\frac{1}{2}}\tan(kD_i)] \tag{3.18b}$$

$$\zeta_{i+1}=k_0D_{i+1}-\tan^{-1}[\varepsilon_r^{-\frac{1}{2}}\tan(kD_{i+1})] \tag{3.18c}$$

The $1/(u'^2-u^2)$ singularity in (3.17a) is removed by subtracting (3.17a) from (3.17b), which is used for $u'\neq k_0$ to give

$$\begin{aligned}
&[M_0'^{(i+1)}(u';D_1,D_2)-\frac{\beta(u')}{\beta_{i+1,0}}M_0'^{(i)}(u';D_i,D_{i+1})]T_{i,0}^{f,p}\\
&+\int_{u=0}^{\infty}\frac{M_2(u',u;D_i,D_{i+1})}{\beta(u)[\beta(u)+\beta(u')]}T_i^{f,p}(u)du\\
&+\int_{u=0}^{\infty}[M_3^{(i+1)}(u',u;D_i,D_{i+1})-\frac{\beta(u')}{\beta(u)}M_3^{(i)}(u',u;D_i,D_{i+1})]T_i^{f,p}(u)du\\
&-2R_i^{f,p}(u=u')=0
\end{aligned} \tag{3.19}$$

In summary, the system of equations at S_i for the p^{th} forward progression is given by (3.13b), (3.14), (3.17b), (3.18a) and (3.19) that is written in normalized form as

$$-R_{i,0}^{f,p}+\overline{M}_{0,0}^{(i+1)}(\overline{D}_i,\overline{D}_{i+1})T_{i,0}^{f,p}+\int_{\overline{u}=0}^{\infty}\overline{M}_0^{(i+1)}(\overline{u};\overline{D}_i,\overline{D}_{i+1})\overline{T}_i^{f,p}(\overline{u})d\overline{u}=A_{i,0}^{f,p} \tag{3.20a}$$

$$-2R_{i,0}^{f,p}+[\overline{M}_{0,0}^{(i+1)}(\overline{D}_i,\overline{D}_{i+1})-\frac{\overline{\beta}_{i,0}}{\overline{\beta}_{i+1,0}}\overline{M}_{0,0}^{(i)}(\overline{D}_i,\overline{D}_{i+1})]T_{i,0}^{f,p}$$

$$+\int_{\overline{u}=0}^{\infty}[\overline{M}_0^{(i+1)}(\overline{u};\overline{D}_i,\overline{D}_{i+1})-\frac{\overline{\beta}_{i,0}}{\overline{\beta}(\overline{u})}\overline{M}_0^{(i)}(\overline{u};\overline{D}_i,\overline{D}_{i+1})]\overline{T}_i^{f,p}(\overline{u})d\overline{u}=0 \tag{3.20b}$$

$$\overline{M}_0'^{(i+1)}(\overline{u}';\overline{D}_i,\overline{D}_{i+1})T_{i,0}^{f,p}+\overline{M}_1(\overline{u}';\overline{D}_i,\overline{D}_{i+1})\overline{T}_i^{f,p}(\overline{u}=\overline{u}')$$

$$+\int_{\overline{u}=0}^{\infty}[\frac{\overline{M}_2(\overline{u}',\overline{u};\overline{D}_i,\overline{D}_{i+1})}{\overline{u}'^2-\overline{u}^2}+\overline{M}_3^{(i+1)}(\overline{u}',\overline{u};\overline{D}_i,\overline{D}_{i+1})]\overline{T}_i^{f,p}(\overline{u})d\overline{u}$$

$$-\overline{R}_i^{f,p}(\overline{u}=\overline{u}')=\overline{A}_i^{f,p}(\overline{u}=\overline{u}') \tag{3.20c}$$

$$[\overline{M}_0'^{(i+1)}(\overline{u}';\overline{D}_i,\overline{D}_{i+1})-\frac{\overline{\beta}(\overline{u}')}{\overline{\beta}_{i+1,0}}\overline{M}_0'^{(i)}(\overline{u}';\overline{D}_i,\overline{D}_{i+1})]T_{i,0}^{f,p}$$

$$+\int_{\overline{u}=0}^{\infty}[\frac{\overline{M}_2(\overline{u}',\overline{u};\overline{D}_i,\overline{D}_{i+1})}{\overline{\beta}(\overline{u})[\overline{\beta}(\overline{u})+\overline{\beta}(\overline{u}')]}+\overline{M}_3^{(i+1)}(\overline{u}',\overline{u};\overline{D}_i,\overline{D}_{i+1})]\overline{T}_i^{f,p}(\overline{u})d\overline{u}$$

$$-\int_{\overline{u}=0}^{\infty}\frac{\overline{\beta}(\overline{u}')}{\overline{\beta}(\overline{u})}\overline{M}_3^{(i)}(\overline{u}',\overline{u};\overline{D}_i,\overline{D}_{i+1})\overline{T}_i^{f,p}(\overline{u})d\overline{u}-2\overline{R}_i^{f,p}(\overline{u}=\overline{u}')=0,$$

$$\text{for } \overline{u}'\neq\overline{k}_0 \tag{3.20d}$$

$$e^{j(\overline{\zeta}_{i+1}-\overline{\zeta}_i)}\overline{T}_i^{f,p}(\overline{u}=\overline{k}_0)+\overline{R}_i^{f,p}(\overline{u}=\overline{k}_0)=\overline{A}_i^{f,p}(\overline{u}=\overline{k}_0),\quad \text{for } \overline{u}'=\overline{k}_0 \tag{3.20e}$$

with

$$\overline{\zeta}_i=\overline{D}_i-\tan^{-1}[\varepsilon_r^{-\frac{1}{2}}\tan(\overline{kD}_i)] \tag{3.20f}$$

$$\overline{\zeta}_{i+1}=\overline{D}_{i+1}-\tan^{-1}[\varepsilon_r^{-\frac{1}{2}}\tan(\overline{kD}_{i+1})] \tag{3.20g}$$

$$A_{i,0}^{f,p}=\begin{cases}[\eta_0\overline{\beta}_{10}]^{\frac{1}{2}}, & \text{for } i=1 \text{ and } p=1\\ T_{i-1,0}^{f,p}e^{-j\overline{\beta}_{i,0}\Delta\overline{z}}, & \text{for } i=2,3,4,\ldots,M-1 \text{ and } p=1\\ R_{10}^{b,p-1}e^{-j\overline{\beta}_{1,0}\Delta\overline{z}}, & \text{for } i=2 \text{ and } p>1\\ [T_{i-1,0}^{f,p}+R_{i-1,0}^{b,p-1}]e^{-j\overline{\beta}_{i,0}\Delta\overline{z}}, & \text{for } i=3,4,5,\ldots,M-1 \text{ and } p>1\end{cases} \tag{3.20h}$$

$$\overline{A}_i^{f,p}(\overline{u}) = \begin{cases} 0, & \text{for } i = 1 \text{ and } p = 1 \\ \overline{T}_{i-1}^{f,p}(\overline{u}) e^{-j\overline{\beta}(\overline{u})\Delta\overline{z}}, & \text{for } i = 2, 3, 4, \ldots, M-1 \text{ and } p = 1 \\ \overline{R}_1^{b,p-1}(\overline{u}) e^{-j\overline{\beta}(\overline{u})\Delta\overline{z}}, & \text{for } i = 2 \text{ and } p > 1 \\ [\overline{T}_{i-1}^{f,p}(\overline{u}) + \overline{R}_{i-1}^{b,p-1}(\overline{u})] e^{-j\overline{\beta}(\overline{u})\Delta\overline{z}}, & \text{for } i = 3, 4, 5, \ldots, M-1 \text{ and } p > 1 \end{cases} \tag{3.20i}$$

$$\Delta\overline{z} = \overline{z}_i - \overline{z}_{i-1} \tag{3.20j}$$

$$i = \begin{cases} 1, 2, 3, \ldots, M-1, & \text{for } p = 1 \\ 2, 3, 4, \ldots, M-1, & \text{for } p > 1 \end{cases} \tag{3.20k}$$

where the normalized overlap integrals in (3.20a)-(3.20d) are related to unnormalized forms as follows:

$$\overline{M}_{0,0}^{(i)(i+1)}(\overline{D}_i, \overline{D}_{i+1}) = M_{0,0}^{(i)(i+1)}(D_i, D_{i+1}) \tag{3.21a}$$

$$\overline{M}_0^{(i)(i+1)}(\overline{u}; \overline{D}_i, \overline{D}_{i+1}) = \sqrt{k_0} M_0^{(i)(i+1)}(u; D_i, D_{i+1}) \tag{3.21b}$$

$$\overline{M}_0'^{(i)(i+1)}(\overline{u}; \overline{D}_i, \overline{D}_{i+1}) = \sqrt{k_0} M_0'^{(i)(i+1)}(u; D_i, D_{i+1}) \tag{3.21c}$$

$$\overline{M}_1(\overline{u}; \overline{D}_i, \overline{D}_{i+1}) = M_1(u; D_i, D_{i+1}) \tag{3.21d}$$

$$\overline{M}_2(\overline{u}', \overline{u}; \overline{D}_i, \overline{D}_{i+1}) = M_2(u', u; D_i, D_{i+1})/k_0 \tag{3.21e}$$

$$\overline{M}_3^{(i)(i+1)}(\overline{u}', \overline{u}; \overline{D}_i, \overline{D}_{i+1}) = k_0 M_3^{(i)(i+1)}(u', u; D_i, D_{i+1}) \tag{3.21f}$$

Note that at each step discontinuity S_i, $2N+4$ unknowns need to be determined. Further study of (3.15a) and (3.15b) when $D_{i+1} \neq 0$ shows that $R_i^{f,p}(u=0) = T_i^{f,p}(u=0) = 0$, i = 1, 2,..., $M-2$, but that when $D_{i+1} = 0$ ($i+1 = M$),

$R_{M-1}^{f,p}(u=0)=0$ and $T_{M-1}^{f,p}(u=0)\neq 0$. Thus, there remains $2N+2$ unknowns to be found at each step discontinuity.

To obtain the field in the backward range ($90^\circ \le \theta \le 180^\circ$), the waves that progress to the left (in the backward direction) that were ignored in the above formulation of the forward progression must be considered. For the p^{th} backward progression, the partial transverse field components in regions $i+1$, i = 1, 2, 3,..., $M-2$, take the forms of

$$\eta_0 H_{y,i+1}^{b,p} = \frac{k_0}{\beta_{i+1,0}}[R_{i,0}^{b,p} e^{-j\beta_{i+1,0}z^{(i-1)}} - B_{i,0}^{b,p} e^{j\beta_{i+1,0}z^{(i-1)}}]\Psi_{i+1,0}(x)$$

$$+ \int_{u=0}^{\infty} \frac{k_0}{\beta(u)}[R_i^{b,p}(u) e^{-j\beta(u)z^{(i-1)}} - B_i^{b,p}(u) e^{j\beta(u)z^{(i-1)}}]\Psi_{i+1}(x,u)du \qquad (3.22a)$$

and

$$E_{x,i+1}^{b,p} = \frac{1}{\varepsilon_{r,i+1}(x)}[R_{i,0}^{b,p} e^{-j\beta_{i+1,0}z^{(i-1)}} + B_{i,0}^{b,p} e^{j\beta_{i+1,0}z^{(i-1)}}]\Psi_{i+1,0}(x)$$

$$+ \frac{1}{\varepsilon_{r,i+1}(x)} \int_{u=0}^{\infty}[R_i^{b,p}(u) e^{-j\beta(u)z^{(i-1)}} + B_i^{b,p}(u) e^{j\beta(u)z^{(i-1)}}]\Psi_{i+1}(x,u)du \qquad (3.22b)$$

where the amplitudes of incident surface wave and radiation waves at discontinuity planes S_i, i = 1, 2, 3,..., $M-2$, are, respectively, given by

$$B_{i,0}^{b,p} = \begin{cases} [T_{i+1,0}^{b,p} + R_{i+1,0}^{f,p}]e^{-j\beta_{i+1,0}\Delta z}, & \text{for } i = 1,2,3,\ldots,M-3 \\ R_{M-1,0}^{f,p} e^{-j\beta_{M-1,0}\Delta z}, & \text{for } i = M-2 \end{cases} \qquad (3.23a)$$

$$B_i^{b,p}(u) = \begin{cases} [T_{i+1}^{b,p}(u) + R_{i+1}^{f,p}(u)]e^{-j\beta(u)\Delta z}, & \text{for } i = 1,2,3,\ldots,M-3 \\ R_{M-1}^{f,p}(u) e^{-j\beta(u)\Delta z}, & \text{for } i = M-2 \end{cases} \qquad (3.23b)$$

where

$$\Delta z = z_{i+1} - z_i \tag{3.23c}$$

The partial transverse fields in region i established by scattering at the step discontinuity S_i are

$$\eta_0 H_{y,i}^{b,p} = -\frac{k_0}{\beta_{i,0}} T_{i,0}^{b,p} e^{j\beta_{i,0} z^{(i-1)}} \Psi_{i,0}(x) - \int_{u=0}^{\infty} \frac{k_0}{\beta(u)} T_i^{b,p}(u) e^{j\beta(u) z^{(i-1)}} \Psi_i(x,u) du \tag{3.24a}$$

and

$$E_{x,i}^{b,p} = \frac{1}{\varepsilon_{r,i}(x)} T_{i,0}^{b,p} e^{j\beta_{i,0} z^{(i-1)}} \Psi_{i,0}(x) + \frac{1}{\varepsilon_{r,i}(x)} \int_{u=0}^{\infty} T_i^{b,p}(u) e^{j\beta(u) z^{(i-1)}} \Psi_i(x,u) du \tag{3.24b}$$

By utilizing boundary condition (3.7a) and (3.7b) at the plane S_i, multiplying $[1/\varepsilon_{r,i+1}(x)]\Psi_{i+1,0}(x)$ and $\Psi_{i+1,0}(x)$ to both sides of the equations, respectively, again multiplying $[1/\varepsilon_{r,i+1}(x)]\Psi_{i+1}(x,u')$ and $\Psi_{i+1}(x,u')$ to both sides of the same equations, respectively, utilizing orthogonality relations (3.6), arranging equations in the same fashion as that of the forward progression and adopting normalized parameters (2.25) yield the system of equations for backward progression at S_i, i = 1, 2, 3,..., $M-2$,

$$-R_{i,0}^{b,p} + \overline{M}_{0,0}^{(i)}(\overline{D}_i, \overline{D}_{i+1}) T_{i,0}^{b,p} + \int_{\overline{u}=0}^{\infty} \overline{M}_0^{\prime(i)}(\overline{u}; \overline{D}_i, \overline{D}_{i+1}) \overline{T}_i^{b,p}(\overline{u}) d\overline{u} = B_{i,0}^{b,p} \tag{3.25a}$$

$$-2R_{i,0}^{b,p}+[\overline{M}_{0,0}^{(i)}(\overline{D}_i,\overline{D}_{i+1})-\frac{\overline{\beta}_{i+1,0}}{\overline{\beta}_{i,0}}\overline{M}_{0,0}^{(i+1)}(\overline{D}_i,\overline{D}_{i+1})]T_{i,0}^{b,p}$$

$$+\int_{\bar{u}=0}^{\infty}[\overline{M}_0'^{(i)}(\bar{u};\overline{D}_i,\overline{D}_{i+1})-\frac{\overline{\beta}_{i+1,0}}{\overline{\beta}(\bar{u})}\overline{M}_0'^{(i+1)}(\bar{u};\overline{D}_i,\overline{D}_{i+1})]\overline{T}_i^{b,p}(\bar{u})d\bar{u}=0 \qquad (3.25b)$$

$$\overline{M}_0^{(i)}(\bar{u}';\overline{D}_i,\overline{D}_{i+1})T_{i,0}^{b,p}+\overline{M}_1(\bar{u}';\overline{D}_i,\overline{D}_{i+1})\overline{T}_i^{b,p}(\bar{u}=\bar{u}')$$

$$+\int_{\bar{u}=0}^{\infty}[-\frac{\overline{M}_2'(\bar{u}',\bar{u};\overline{D}_i,\overline{D}_{i+1})}{\bar{u}'^2-\bar{u}^2}+\overline{M}_3'^{(i)}(\bar{u}',\bar{u};\overline{D}_i,\overline{D}_{i+1})]\overline{T}_i^{b,p}(\bar{u})d\bar{u}$$

$$-\overline{R}_i^{b,p}(\bar{u}=\bar{u}')=\overline{B}_i^{b,p}(\bar{u}=\bar{u}') \qquad (3.25c)$$

$$[\overline{M}_0^{(i)}(\bar{u}';\overline{D}_i,\overline{D}_{i+1})-\frac{\overline{\beta}(\bar{u}')}{\overline{\beta}_{i,0}}\overline{M}_0^{(i+1)}(\bar{u}';\overline{D}_i,\overline{D}_{i+1})]T_{i,0}^{b,p}$$

$$+\int_{\bar{u}=0}^{\infty}[-\frac{\overline{M}_2'(\bar{u}',\bar{u};\overline{D}_i,\overline{D}_{i+1})}{\overline{\beta}(\bar{u})[\overline{\beta}(\bar{u})+\overline{\beta}(\bar{u}')]}+\overline{M}_3'^{(i)}(\bar{u}',\bar{u};\overline{D}_i,\overline{D}_{i+1})]\overline{T}_i^{b,p}(\bar{u})d\bar{u}$$

$$-\int_{\bar{u}=0}^{\infty}\frac{\overline{\beta}(\bar{u}')}{\overline{\beta}(\bar{u})}\overline{M}_3'^{(i+1)}(\bar{u}',\bar{u};\overline{D}_i,\overline{D}_{i+1})\overline{T}_i^{b,p}(\bar{u})du-2\overline{R}_i^{b,p}(\bar{u}=\bar{u}')=0\,,$$

$$\text{for } \bar{u}'\neq\bar{k}_0 \qquad (3.25d)$$

$$e^{-j(\bar{\zeta}_{i+1}-\bar{\zeta}_i)}\overline{T}_i^{b,p}(\bar{u}=\bar{k}_0)+\overline{R}_i^{b,p}(\bar{u}=\bar{k}_0)=\overline{B}_i^{b,p}(\bar{u}=\bar{k}_0)\,,\quad \text{for } \bar{u}'=\bar{k}_0 \qquad (3.25e)$$

where

$$\bar{\zeta}_i=\overline{D}_i-\tan^{-1}[\varepsilon_r^{-\frac{1}{2}}\tan(\bar{k}\overline{D}_i)] \qquad (3.25f)$$

$$\bar{\zeta}_{i+1}=\overline{D}_{i+1}-\tan^{-1}[\varepsilon_r^{-\frac{1}{2}}\tan(k\overline{D}_{i+1})] \qquad (3.25g)$$

$$B_{i,0}^{b,p}=\begin{cases}[T_{i+1,0}^{b,p}+R_{i+1,0}^{f,p}]e^{-j\bar{\beta}_{i+1,0}\Delta\bar{z}}, & \text{for } i=1,2,3,\ldots,M-3\\ R_{M-1,0}^{f,p}e^{-j\bar{\beta}_{M-1,0}\Delta\bar{z}}, & \text{for } i=M-2\end{cases} \qquad (3.25h)$$

$$\overline{B}_i^{b,p}(\bar{u})=\begin{cases}[\overline{T}_{i+1}^{b,p}(\bar{u})+\overline{R}_{i+1}^{f,p}(\bar{u})]e^{-j\bar{\beta}(\bar{u})\Delta\bar{z}}, & \text{for } i=1,2,3,\ldots,M-3\\ \overline{R}_{M-1}^{f,p}(\bar{u})e^{-j\bar{\beta}(\bar{u})\Delta\bar{z}}, & \text{for } i=M-2\end{cases} \qquad (3.25i)$$

$$\Delta\bar{z}=\bar{z}_{i+1}-\bar{z}_i \qquad (3.25j)$$

$$\overline{M}_2'(\overline{u}',\overline{u};\overline{D}_i,\overline{D}_{i+1}) = \overline{M}_2(\overline{u},\overline{u}';\overline{D}_i,\overline{D}_{i+1}) \tag{3.25k}$$

$$\overline{M}_3'^{(i+1)}(\overline{u}',\overline{u};\overline{D}_i,\overline{D}_{i+1}) = \overline{M}_3^{(i+1)}(\overline{u},\overline{u}';\overline{D}_i,\overline{D}_{i+1}) \tag{3.25l}$$

Similar to forward progression, no scattering radiation occurs for $\overline{u} = 0$ at the discontinuity planes S_i, $i = 1, 2, 3, \ldots, M-2$; hence,

$$\overline{R}_i^{b,p}(\overline{u}=0) = \overline{T}_i^{b,p}(\overline{u}=0) = 0, \quad \text{for } i = 1, 2, 3, \ldots, M-2 \tag{3.26}$$

Applying (3.26) to (3.25a)-(3.25d), the discretization process and the singular integral evaluations provide the required set of $2N+2$ linear equations for the $2N+2$ unknowns, i.e., $R_{i,0}^{b,p}$, $T_{i,0}^{b,p}$, $\overline{R}_i^{b,p}(\overline{u}=\overline{u}_m)$ and $\overline{T}_i^{b,p}(\overline{u}=\overline{u}_m)$, $m = 1, 2, 3, \ldots, N$.

3.3 Antenna Characteristics

For TM polarization, the reflection coefficient at the input to the wedge antenna is also given by (2.36). The radiation intensity is determined by asymptotic evaluation of the magnetic fields in the free space region $i = M$ off the tip of the antenna and in the feed guide region $i = 1$ and found to be given by

$$U(\theta) = \begin{cases} \dfrac{\eta_0}{2}\left|\overline{T}_f(\sin\theta)\right|^2, & \text{for } 0 \le \theta \le \dfrac{\pi}{2} \\ \dfrac{\eta_0}{2}\left|\overline{R}_b(\sin\theta)\right|^2, & \text{for } \dfrac{\pi}{2} \le \theta \le \pi \end{cases} \tag{3.27}$$

where $U(-\theta) = U(\theta)$. Amplitudes $\overline{T}_f(\sin\theta)$ and $\overline{R}_b(\sin\theta)$ are, respectively, the composition of N_f and N_b orders of mode amplitudes given by (2.38a) and (2.38b).

CHAPTER 4

NUMERICAL RESULTS

The method presented in Chapter 2 and 3 approximates the dielectric wedge by a sequence of short slab segments of progressively smaller widths. Hence, a more accurate determination of the field scattered by the wedge geometry is obtained by increasing the number of segments used. In theory, the method yields a rigorous solution when the mode-matching at each single step discontinuity is accurately performed. To ascertain this accuracy, comparisons are made with published data for scattering from a single step discontinuity, particularly, in the TE polarization since published data is not readily available for the TM case.

The first example of scattering at a single step discontinuity is shown in Figure 4.1. The refractive index of two dielectric slabs is $n_1 = 1.54$ and that of the surrounding medium is $n_2 = 1.52$. The fundamental TE surface wave mode is assumed to be incident from the left and to carry unity power.

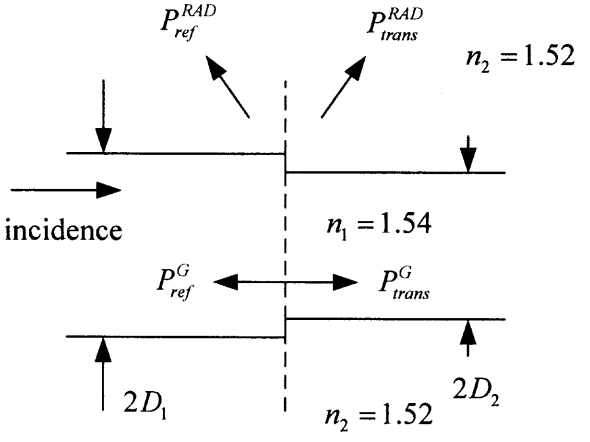

Figure 4.1 Step discontinuity with $n_1 = 1.54$, $n_2 = 1.52$ and incidence from the left.

Tables 4.1 and 4.2 show comparison of results for the structure in Figure 4.1 based on the present theory with the data of Suchoski, Jr. and Ramaswamy [13]. Table 4.1 describes scattering at a step discontinuity that is modest, however not small since $D_2/D_1 = 0.6$, and for dielectric media with indices of refraction that are numerically close, which is of interest in the design of integrated optical devices. Observe that, as far as conservation of power is concerned, the corrections made to [13] that are implemented here yield a significant redistribution of power, although conservation of power is well satisfied in both cases. Note that the power contained in the reflected surface wave mode (P_{ref}^{G}) is over twice as large, the power carried by the transmitted radiation mode (P_{trans}^{RAD}) is about 10% smaller and the power in the reflected radiation modes (P_{ref}^{RAD}) is approximately two orders of magnitude smaller than that of [13]. By definition, P_{trans}^{G} is the power carried by the transmitted surface wave mode. In Table 4.1(a), reproduced from [13], data is presented for truncation at $u_{\max} = k_0$, which excludes evanescent radiation modes, whereas data in Table 4.1(b) includes these modes since $u_{\max} = 2k_0$. Note that N is twice as large for the latter to insure that the discretization step Δu is the same in both cases and the same number of propagating radiation modes is considered. For the same dielectric media, Table 4.2 displays conservation of power at a step discontinuity that is large since $D_2/D_1 = 0.2$. In this case, the results show a significant redistribution of power for all wave constituents, even though conservation of power is again satisfied.

Table 4.1 Comparison of Results with Suchoski, Jr. and Ramaswamy at a Small Step Discontinuity for TE Polarization, $n_1 = 1.54$, $n_2 = 1.52$, $\lambda_0 = 0.6328\ \mu\text{m}$, $D_1 = 0.5\ \mu\text{m}$, $D_2 = 0.3\ \mu\text{m}$, (a) Suchoski, Jr. and Ramaswamy and (b) The Present Method Using $u_{\max} = 2k_0$

N	P_{trans}^{G}	P_{ref}^{G}	P_{trans}^{RAD}	P_{ref}^{RAD}	P^{TOTAL}
50	0.99161766	0.0000011	0.0073938	0.0009793	0.9999919
70	0.99161685	0.0000011	0.0073954	0.0009802	0.9999936
100	0.99161620	0.0000011	0.0073963	0.0009808	0.9999944
120	0.99161626	0.0000011	0.0073967	0.0009812	0.9999953
150	0.99161630	0.0000011	0.0073969	0.0009813	0.9999956

(a)

N	P_{trans}^{G}	P_{ref}^{G}	P_{trans}^{RAD}	P_{ref}^{RAD}	P^{TOTAL}
100	0.99339498	0.00000242	0.00658701	0.00001569	1.00000011
140	0.99339161	0.00000242	0.00659065	0.00001573	1.00000041
200	0.99339014	0.00000242	0.00659202	0.00001576	1.00000034
240	0.99338983	0.00000242	0.00659228	0.00001577	1.00000030
300	0.99338963	0.00000242	0.00659243	0.00001578	1.00000026

(b)

Table 4.2 Comparison of Results with Suchoski, Jr. and Ramaswamy at a Large Step Discontinuity for TE Polarization, $n_1 = 1.54$, $n_2 = 1.52$, $\lambda_0 = 0.6328\,\mu\text{m}$, $D_1 = 0.5\,\mu\text{m}$, $D_2 = 0.1\,\mu\text{m}$, (a) Suchoski, Jr. and Ramaswamy and (b) The Present Method Using $u_{\max} = 2k_0$

N	P_{trans}^{G}	P_{ref}^{G}	P_{trans}^{RAD}	P_{ref}^{RAD}	P^{TOTAL}
50	0.73635	0.000081	0.24162	0.02596	1.00401
70	0.73728	0.000093	0.24199	0.02385	1.00321
100	0.73742	0.000099	0.24262	0.02243	1.00257
120	0.73743	0.000102	0.24300	0.02139	1.00192
150	0.73744	0.000103	0.24310	0.01949	1.00013

(a)

N	P_{trans}^{G}	P_{ref}^{G}	P_{trans}^{RAD}	P_{ref}^{RAD}	P^{TOTAL}
100	0.79132345	0.00001433	0.20700815	0.00001382	0.99835976
140	0.79420232	0.00001433	0.20565740	0.00001382	0.99988787
200	0.79494284	0.00001433	0.20504311	0.00001382	1.00001411
240	0.79507175	0.00001433	0.20491034	0.00001383	1.00001024
300	0.79515462	0.00001433	0.20482278	0.00001383	1.00000555

(b)

Next example of a step discontinuity is shown in Figure 4.2 where the relative permittivity of two dielectric slabs is $\varepsilon_r = 5$, the surrounding media is free space, and $k_0 D_1 = 1$. The fundamental TE surface wave mode with unity power is incident from the right slab waveguide of smaller width $2D_2$.

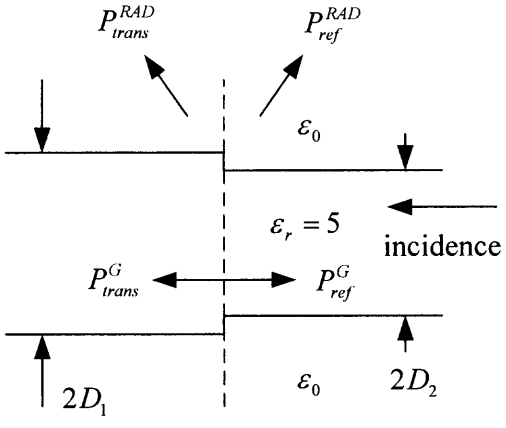

Figure 4.2 Step discontinuity of two slabs with $\varepsilon_r = 5$ surrounded by free space.

Table 4.3 shows the comparison of the power distribution at the step discontinuity obtained from the present theory with data of Hirayama and Koshiba [15], who used a combination of the finite-element and boundary-element methods (CFBEM). Truncation for the mode-matching method presented here is taken at $u_{\max} = 7k_0$ using a total of $N = 910$ discretized segments, which include $N_P = 130$ segments for the propagating radiation modes and $N_E = 780$ segments for the evanescent radiation modes (see Appendix E). In the table, the radiated power is given by $P^{RAD} = P_{trans}^{RAD} + P_{ref}^{RAD}$. Observe that there is very good agreement for the distribution of power among the modes.

Table 4.3 Comparison of Results with Hirayama and Koshiba at a Step Discontinuity for $k_0 D_1 = 1$, $\varepsilon_r = 5$ Surrounded by Free Space, TE Mode Incident from Smaller Slab of Width $2D_2$, Using $u_{\max} = 7k_0$, $N = 910$ ($N_P = 130$, $N_E = 780$)

D_2/D_1	Method	P^G_{trans}	P^G_{ref}	P^{RAD}	P^{TOTAL}
0.2	Present method	0.8866	0.0416	0.0718	1.0000
	CFBEM*	0.8865	0.0416	0.0715	0.9996
0.04	Present method	0.3614	0.0103	0.6279	0.9996
	CFBEM**	0.3620	0.0100	0.6278	0.9998

* : Table I with $d_1/d_2 = 0.2$, Fig. 3(a) in [15].
** : Table I with $d_1/d_2 = 0.04$, Fig. 3(a) in [15].

Many journal publications have treated the problem of scattering from a single step discontinuity [13]-[16], [26]-[42]. Several of these publications compare their results with Rozzi [14], who used a rigorous variational approach to analyze the step discontinuity problem shown in Figure 4.3, where the relative permittivity of two dielectric slabs is $\varepsilon_r = 5$, surrounding media is free space and $k_0 D_1 = 1$. Results for the TE polarization case are shown in Figures 4.4 and 4.5. In Figure 4.4, the radiated power ($P^{RAD} = P^{RAD}_{trans} + P^{RAD}_{ref}$) is plotted versus D_2/D_1 and normalized to the incident power (P_{inc}) that is carried by the fundamental TE surface wave mode incident either from the left in Figure 4.3(a) or from the right in Figure 4.3(b); the larger slab cross-section ($2D_1$) is taken to the left, which differs from that of Rozzi [14] who placed the narrower slab on the left. The magnitudes of the reflection and transmission coefficients for incidence form the left ($|\Gamma^f|$, $|\tau^f|$) and from the right ($|\Gamma^b|$, $|\tau^b|$) are also plotted in Figure 4.4. As is evident, excellent agreement is obtained between the results of the present method and that of Rozzi.

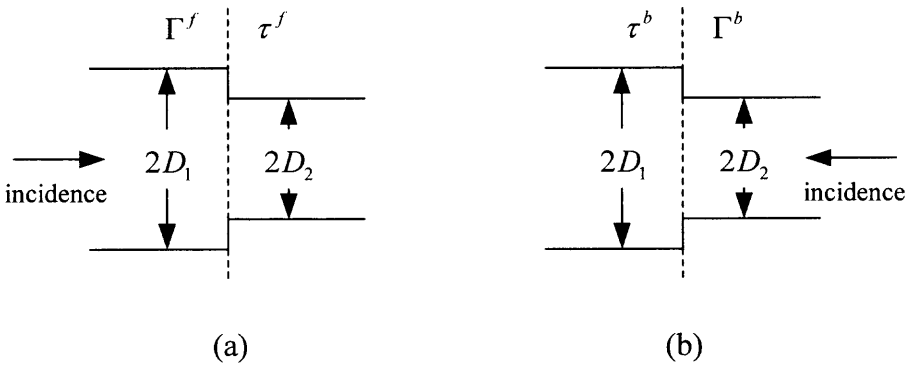

Figure 4.3 Step discontinuities of two slabs with $\varepsilon_r = 5$ surrounded by free space, (a) incidence from the left (b) incidence from the right.

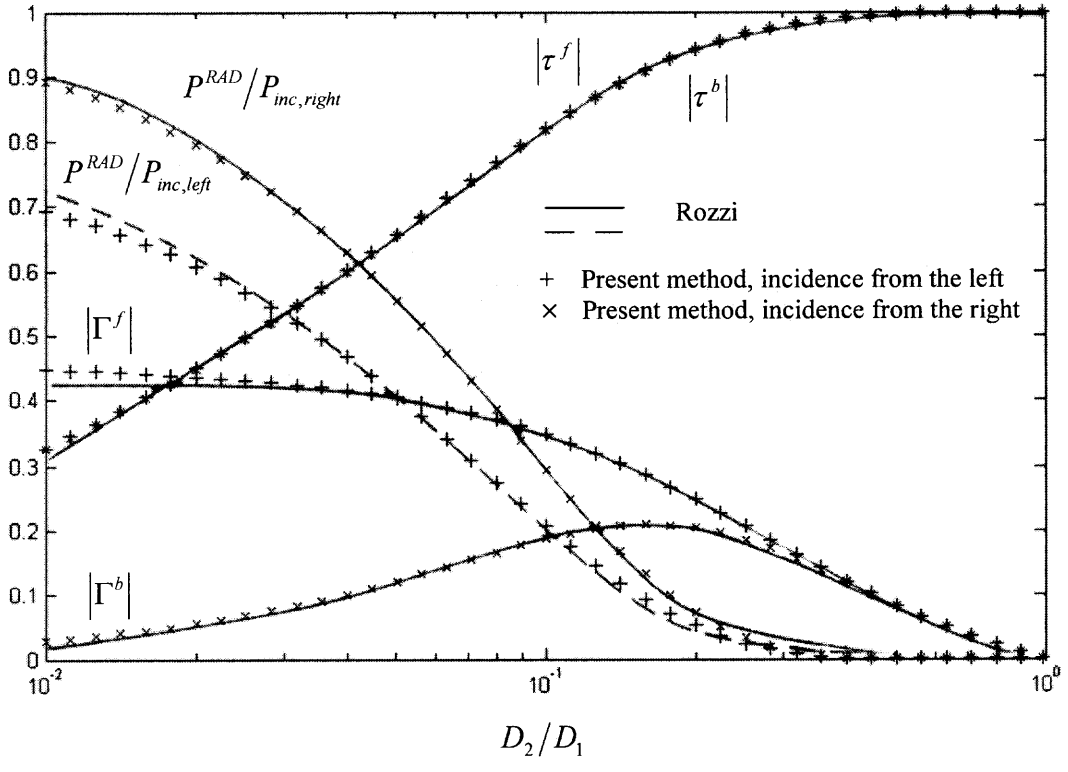

Figure 4.4 Comparison of radiated power and the magnitudes of reflection and transmission coefficients of a step discontinuity between two slab waveguides versus relative step width for $k_0 D_1 = 1$, $\varepsilon_r = 5$, using $u_{\max} = 7k_0$ and $N = 910$ ($N_P = 130$, $N_E = 780$), TE polarization.

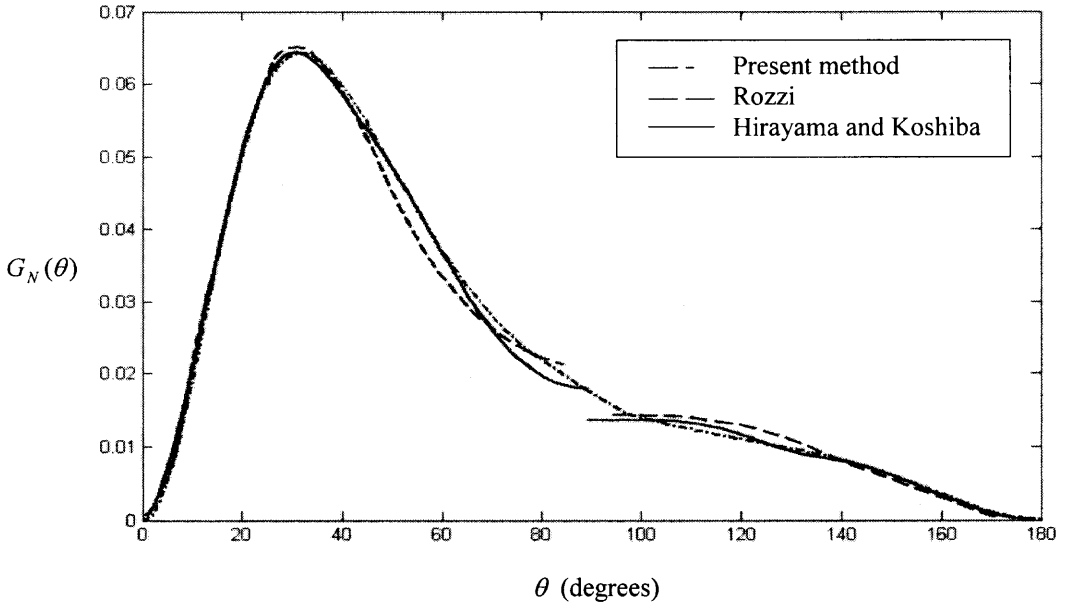

Figure 4.5 Comparison of radiation patterns of normalized power gain $G_N(\theta)$ for single step discontinuity for $\varepsilon_r = 5$, $k_0 D_1 = 1$ and $D_2/D_1 = 0.2$, TE mode incident from the right, using $u_{\max} = 7k_0$ and $N = 910$ ($N_P = 130$, $N_E = 780$).

Figure 4.5 is a plot of the normalized power gain $G_N(\theta) = U(\theta)/P_{inc}$ versus elevation angle θ for TE polarization, where $U(\theta)$ is the radiation intensity, θ is the angle measured from the +*z*-axis in the *xz*-plane shown in Figure 2.1. Note that in the curves taken from the literature [14], [16] a discontinuity appears in the region near $\theta = 90^\circ$. In the present theory, this problem has been eliminated by the appropriate normalization (2.2), resulting in pattern continuity at 90°. Results in Figure 4.5 show good agreement between the three methods plotted.

In Figures B.1-B.18 (Appendix B), the radiation patterns of directive gain $D(\theta)$ versus elevation angle θ for different dielectric wedge antennas for TE and TM polarization are presented. The patterns are endfire, as expected. In Figures B.1-B.12,

results are shown for increasing number of finite slab segments $N_S = M - 2$ (which decreases Δz) while keeping all other parameters fixed. In this way, the step geometry in Figure 2.1 approaches that of the wedge. As shown in all the curves, the radiation patterns converge to limiting smooth shapes over the forward directional range $0^\circ < \theta < 90^\circ$ and backward directional range $90^\circ < \theta < 180^\circ$. Subsequently, results are presented in Figures B.13-B.18 that characterize the wedge radiator for different dielectric constants ε_r and relative lengths L/λ_0, where λ_0 is the free space wavelength.

A Pentium 4-2.8 GHz PC was used to obtain numerical results. The CPU time used to obtain the second-order partial fields ($N_f = N_b = 2$ in (2.30)) for a typical curve of directive gain versus elevation angle in the TE case was 185 minutes for 40 slab segments ($N_S = 40$); this assumes $N = 300$.

To insure that as ε_r increases only one surface wave mode is above cutoff for both TE and TM cases, D_1/λ_0 is chosen to satisfy the relationship

$$\frac{D_1}{\lambda_0} = 0.25(\varepsilon_r - 1)^{-\frac{1}{2}} \tag{4.1}$$

In the TE case, (4.1) insures that the incident surface waves for different values of ε_r have identical wavenumbers $\alpha_{x10}D_1$ in the free space and $k_{x10}D_1$ in the dielectric feed slab region. In the TM case, however, ε_r appears in the dispersion relation (3.5), then normalized wavenumbers do not remain constant as ε_r varies.

All data depicted in Figures B.1-B.36 is obtained using first and second-order partial fields. For the wedge antennas in the TE case with $\varepsilon_r \geq 8$ and $L/\lambda_0 \geq 5$,

the first-order solution is used; the first-order solution appears more accurate for such cases since it does not generate any irregularities near 90° that do appear when the second-order solution is used.

The materials chosen for Figures B.1-B.16 are lucite ($\varepsilon_r = 2.56$) and silicon ($\varepsilon_r = 12$). In Figures B.1 and B.2, the wedge parameters are $\varepsilon_r = 2.56$, $D_1/\lambda_0 = 0.2$, $L/\lambda_0 = 1$, $u_{\max} = 2k_0$ and $N = 300$ with $N_P = 150$ and $N_E = 150$. For this relatively short wedge, the directive gains are obtained for four different numbers of slab segments N_S, namely, 10, 20, 40 and 60. Figures B.1 and B.2 show that even a small number of slab segments (10-20) is sufficient to secure convergence in the forward and backward angular ranges.

In Figures B.3 and B.4, ε_r is taken to be 12 and the slab/wedge width D_1/λ_0 is adjusted in accordance with (4.1) while the antenna length L/λ_0 remains identical to the one used in Figures B.1 and B.2. Again it is evident that even a small number of segments can guarantee the convergence in all angular ranges.

Radiation patterns for wedge antennas with $L/\lambda_0 = 5$ and 10 are shown in Figures B.5-B.12. In calculating these patterns, $u_{\max} = 2k_0$ is assumed. It is evident from the figures that the patterns converge well as the number of slab segments N_S in the staircase model is increased (so that the staircase more accurately models the wedge). Clearly, all patterns are endfire. In the TE case, the directivity ($D_{\max}$) is typically 9-10 dB for $\varepsilon_r = 2.56$ and 8-9 dB for $\varepsilon_r = 12$. In the TM, the directivity for $\varepsilon_r = 2.56$ and $\varepsilon_r = 12$ for the same lengths is effectively unchanged, i.e., 11-12 dB. It is seen in both TE and TM cases (also see Tables A.5 and A.6 in Appendix A) that a longer

taper leads to the (moderately) higher directivity and narrower half-power beamwidth (HPBW). These trends were expected. Only for the TE case, it appears that larger values of dielectric constant (ε_r) produce smaller directivity and broader beamwidths (see Table A.5(c)).

An interesting result in the TE case is that the radiation patterns are essentially free of side lobes for both dielectric constant materials. The patterns do, however, exhibit undulating characteristics [43], as suggested by Figures B.5 and B.9. As the relative wedge length L/λ_0 increases from $L/\lambda_0 = 5$ to $L/\lambda_0 = 10$, the pattern undulations become more numerous. This trend is also valid up to $L/\lambda_0 = 20$ as shown in Figure B.13. In the TM case, all the patterns display small side lobes. Their Side Lobe Level (SLL) and θ_S, the angle where the maximum side lobe peak occurs, are shown in Table A.7. An important conclusion from this study is this occurs for dielectric wedge antennas fed by a uniform dielectric waveguide of the same dielectric constant.

The low side lobe level of dielectric wedge antennas and, by implication, tapered rod antennas is not obvious. Experimental results for the latter tend to show high side lobes [44]-[48]. However, the antennas used in these experiments typically were fed by a dielectric guide extending into a metal waveguide that served as the overall feed. Based on the patterns shown in Figures B.5-B.12 and extrapolation to tapered rod antennas, the measured high side lobe level is attributed to radiation from the metal waveguide-to-dielectric guide transition and is not a feature of the antenna itself. It is confirmed by measurements in [49] that using a tapered rod antenna whose metal-to-dielectric waveguide transition was carefully designed can minimize scattering. Thus, low side lobes resulted.

Tables A.1-A.4 show the power radiated by the antennas of Figures B.5-B.12 in the forward region ($z > L$) and backward region ($z < 0$), as well as the power of the reflected surface wave on the feed guide P_{ref}^{G} . These powers are normalized by assuming that the power of the incident surface wave is unity. Note that P_{ref}^{G} in both TE and TM cases, which is proportional to the magnitude of the reflection coefficient squared of the antenna, is very small, i.e., $< 10^{-4}$ for $L/\lambda_0 = 10$.

Figures B.13-B.18 provide a more comprehensive examination of the dependence of pattern shape and directivity on the wedge length and the value of its dielectric constant. Figures B.13-B.16 examine the length dependence and confirm that a longer wedge increases the directivity of the antenna and narrows the HPBW. Tables A.5(a), (b) and A.6(a), (b) specify the directivity and HPBW, also SLL for the TM case, for the wedge lengths depicted in Figures B.13-B.16. It is seen from Table A.6(a) and A.6(b) that SLL for the TM case is very small (less than -35 and -31 dB for $\varepsilon_r = 2.56$ and 12, respectively).

In Figures B.17 and B.18, the radiation patterns of directive gain for the $5\lambda_0$ wedge length are shown for $\varepsilon_r = 2.56$, 5, 8 and 12. Again it is observed from Figure B.17 that, for the TE case, directivity is less and the HPBW is broader when ε_r is larger. However, in the TM case, this trend is not observed. Figure B.18 shows for the TM case that wedges of higher dielectric constant produce essentially the same directivity and HPBW as identical wedges of smaller dielectric constant material. Tables A.5(c) and A.6(c) list the values of directivity and HPBW, also SLL for the TM case, for the wedges

considered in Figures B.17 and B.18. It is seen from Table A.6(c) that SLL for the TM case is very small.

Figures B.19-B.24 compare directive gain patterns obtained from the present method and the equivalent current-local mode method[6] [50], [51]. Figures B.19 and B.20 depict TE polarization directive gain patterns for wedge antennas having dielectric constants $\varepsilon_r = 2.56$ and 12, respectively, and relative lengths $L/\lambda_0 = 1$, 5 and 10. Figure B.21 compares TE polarization directive gain patterns for $L/\lambda_0 = 5$ and $\varepsilon_r = 2.56$, 8 and 12. For the worst case in these figures ($\varepsilon_r = 2.56$ and $L/\lambda_0 = 10$), curves with identical parameters show excellent agreement in the physically important forward angular range $0^\circ < \theta < 90^\circ$. Even in the backward angular range $90^\circ < \theta < 160^\circ$, where the directive gain is small (less than -35 dB), the two methods yield results that follow one another. In the range $160^\circ < \theta < 180^\circ$, the patterns continue to decrease for both methods. The local mode patterns converge to finite small values in the backward direction ($\theta = 180^\circ$) while the patterns from the mode-matching method decrease to zero rapidly. All patterns have their maxima in the endfire direction and show extremely low side lobes.

Figures B.22-B.24 depict directive gain patterns for the TM case. Figures B.22 and B.23 show the patterns for wedge antennas of different lengths for $\varepsilon_r = 2.56$ and

---

[6] The equivalent current-local mode is an alternative and much simpler approach for analyzing two-dimensional tapered dielectric radiators. This method uses a local mode theory to determine the polarization current distribution in the dielectric region and applies vector potential functions to calculate the far-field pattern. The local mode theory assumes that the incident wave in each slab segment continues to propagate as a surface wave. The reflected surface wave modes generated by the sloped boundary surfaces of the dielectric wedge do not significantly contribute to the current distribution and can be neglected. This method results in a simple formula, thereby significantly simplifying the computational effort time.

$\varepsilon_r = 12$, respectively. Figure B.24 shows a comparison of directive gain patterns for $L/\lambda_0 = 5$ and different dielectric constant materials. In these figures, the patterns show excellent agreement over the range $0 < \theta < 50^\circ$ for $\varepsilon_r = 2.56$ and over the range $0 < \theta < 30^\circ$ for $\varepsilon_r = 12$, occupying the most significant portion of the major lobe. Over the remaining range, the patterns from both methods diverge from one another more strongly than those in the TE case. Similar to the TE case, as θ approaches to 180°, the local mode patterns approach to finite values while the patterns from the present method go to zero.

From the conceptual viewpoint, one may expect a gain limitation for tapered dielectric rod and wedge antennas [4]; see also the discussion in [52], [53] on rod antennas shaped for maximum gain. Tapered dielectric antennas are surface wave antennas and the phase velocity of a guided wave traveling down the antenna is always smaller than the free space wave velocity so that the contributions of the various antenna cross-sections (or step discontinuities in the staircase model) to the radiation pattern do not add in phase in the forward direction (main beam direction) or any other direction. Hence, if a certain antenna length L is exceeded, destructive interference will occur which is likely to result in a limitation on the attainable directivity and in increased side lobes since part of the radiated energy is now directed away from the main beam. The limitation should be significant, in particular, for antennas made from high-ε_r materials. A rough criterion for the useful length of a tapered dielectric antenna would be

that $\Delta\phi$, the difference between the accumulated phase of the surface wave traveling down the antenna and a forward traveling free space wave, should remain below π,[7] i.e.,

$$\Delta\phi = \int_{z=0}^{L} [\beta_0(z) - k_0]dz = \Delta z \sum_{i=2}^{M-1} (\beta_{i,0} - k_0) \leq \pi \tag{4.2}$$

where $\beta_0(z)$ is the (local) propagation constant of the surface wave and the second (sum) expression for $\Delta\phi$ applies to the staircase model of the antenna.

However, tables A.5(a), (b) and A.6(a), (b) show that the gain for the linear tapered wedge antenna does not suffer a limitation. The directivity increases gradually and continuously with the antenna's length up to $20\lambda_0$[8] for both $\varepsilon_r = 2.56$ and $\varepsilon_r = 12$. For $L/\lambda_0 = 20$, the phase difference (4.2) is 8.88π for $\varepsilon_r = 2.56$ and is as large as 42.51π for $\varepsilon_r = 12$, while in the TM case, it is 4.39π and 5.35π for $\varepsilon_r = 2.56$ and 12, respectively. In all cases, 180 slab segments ($N_S = 180$) are used. Furthermore, the corresponding radiation patterns maintain very low side lobes. This indicates that antennas with a linear taper profile do not have a gain limitation. Since based on limited values for the parameters L and ε_r, this conclusion is not definitive, of course. A conclusive answer would require an asymptotic theory valid for very large parameter values and is beyond the scope of the dissertation. It is also not of great interest from the application viewpoint since tapered dielectric antenna with a length exceeded $20\lambda_0$

---

[7] The contribution of the base and the tip region of the antenna to the radiation pattern in the endfire direction (main beam) should not differ in phase by more than 180°.

[8] The antenna length of $20\lambda_0$ is the largest one used here to calculate the gain.

would be rather fragile and not very practical in the first place. The use of arrays of tapered dielectric antennas would be a better approach to raise directivity.

It is a relatively simple task to study different symmetrical geometries to obtain their radiation patterns. In Figures B.25 and B.26, for both TE and TM cases, the directive gain patterns of two non-uniform, dielectric antennas are compared to the pattern of the linearly tapered wedge antenna. The non-uniform antennas have two-dimensional, geometric profiles of an ellipse and a circle. The circle antenna has radius D_1 given by (4.2). The ellipse and wedge antennas have the same length $L/\lambda_0 = 10$. All three antennas have relative permittivity $\varepsilon_r = 2.56$. Figures B.25 and B.26 show that all patterns have their maxima in the endfire direction. It is evident that there is no occurrence of side lobes in the patterns generated from the circle profile in both TE and TM cases and from elliptic profile in the TE case. Table A.8 lists the values of directivity, HPBW and $|\Gamma|$ for the profiles under discussion. It shows that, for both TE and TM cases, the circle antenna yields the lowest directivity and the highest values for HPBW and $|\Gamma|$, whereas the wedge antenna yields the highest directivity and the lowest values for HPBW and $|\Gamma|$. These trends were expected.

An interesting structure of non-uniform antennas was proposed by Zucker [52], [53], who introduced a uniform section in a tapered dielectric rod antenna fed by a circular metal waveguide. The Zucker's profile for rod antennas has been extrapolated to the two-dimensional structure shown in Figure 4.6. The profile has a total length of L, consisting of three parts: a feed taper, a uniform section, and a terminal taper with lengths

L_F, L_U and L_T, respectively. In this analysis, the feed and terminal tapers are assumed to be linear.

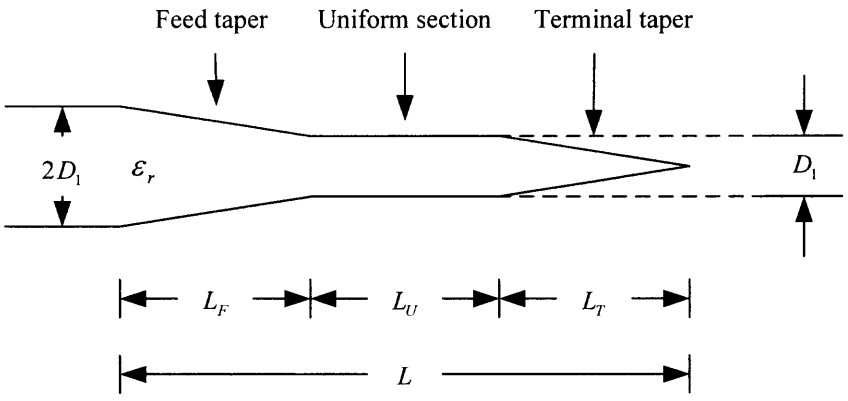

Figure 4.6 Linearly tapered antenna with a uniform section (Zucker's profile).

Figures B.27-B.30 compare the gain patterns of Zucker antennas for different uniform section lengths to the pattern of a linearly tapered wedge antenna. In these comparisons, the Zucker and wedge antennas have the same relative length $L/\lambda_0 = 10$. For the Zucker type, the length of the feed taper is assumed to be equal to that of the terminal taper ($L_F = L_T$). In Figures B.27-B.30, all patterns for both TE and TM cases are endfire. For the TE case, the patterns of the wedge antenna display smooth curves in all angular ranges for $\varepsilon_r = 12$ but display slightly undulating characteristics for $\varepsilon_r = 2.56$. With a uniform section introduced, the patterns exhibit more pronounced fluctuations. Comparisons show that as the uniform section is made longer, the fluctuation extrema increase, the directivity diminishes, and the HPBW becomes broader (see also Table A.9). For the TM case, it is seen that as the length L_U increases,

fluctuation extrema in the main beam and side lobes increase. Additionally, for $\varepsilon_r = 12$, side lobe levels become significant.

Figures B.31-B.34 show the comparisons when the feed and terminal taper lengths are held constant by assuming that $L_F/\lambda_0 = L_T/\lambda_0 = 5$ and L_U/λ_0 increases. For the TE case, fluctuation extrema increase (more pronounced for $\varepsilon_r = 2.56$ than for $\varepsilon_r = 12$), while the values of the directivity and HPBW remain nearly identical when the uniform section length varies; see also Table A.11. For the TM case, Figures B.33-B.34 show that as the length L_U increases, the SLL increases. Again, for $\varepsilon_r = 12$, side lobe levels increase significantly, particularly in the forward angular range, compared to the pattern for $\varepsilon_r = 2.56$. Tables A.9-A.12 list associated parameters suggested in Figures B.27-B.34. In these tables, θ_S is the angle where SLL or the level of fluctuation is determined. It can be concluded that to reduce side lobes, tapers that extend over a substantial part of the antenna are needed. This conclusion agrees with Zucker in [53] for designing low side lobe surface-wave antennas.

The frequency characteristics of a linearly tapered wedge antenna was examined as shown in Figures B.35 and B.36. The antenna examined had a wedge length of $10\lambda_c$ and a feed guide width of $2D_1 = 0.5\lambda_c(\varepsilon_r - 1)^{-\frac{1}{2}}$, where λ_c is the wavelength at the center angular frequency (ω_c). The VSWR, directivity and HPBW versus relative frequency (ω/ω_c) are plotted in Figure B.35 for the TE case and in Figure B.36 for the TM case. The relative frequency ω/ω_c is varied from 0.05 to 1.98; $\omega/\omega_c = 1.98$ is the maximum used to maintain the single surface wave mode criterion (4.1). The ratio of

the maximum to minimum frequency is 39.6. For both TE and TM cases, the VSWR is significantly less than 2.0 over the frequency range (as high as 39.6:1), thereby indicating that the dielectric wedge antenna can be classified as a broadband antenna, as expected. In these figures, when ω/ω_c varies from slightly below 1 to 1.98, the directivity and the HPBW are approximately constants.

CHAPTER 5

CONCLUSION

An accurate theory for a dielectric wedge antenna fed by a dielectric slab has been formulated and evaluated using a staircase model for the wedge geometry. In this model, the wedge region is approximated by short, uniform slab waveguide segments. Using the rigorous solution to scattering from a single step discontinuity, the field scattered by multiple steps is found in terms of partial fields. The partial fields are determined by first considering waves progressing toward the tip, then back from the tip toward the semi-infinite slab waveguide region, toward the tip a second time, and so on until sufficient accuracy is reached. In this way, the total field is found as a superposition of partial fields. The result is approximate only in that infinite integrals are truncated and numerically determined.

TE and TM polarization are considered. For both cases, the radiation pattern is shown to have its maximum in the endfire direction, as expected, with very low side lobes. Longer wedges are shown to have higher directivity and to possess narrower HPBW; no gain limitation was encountered, at least not up to a wedge length $L/\lambda_0 = 20$. For TE polarization, wedges of higher dielectric constant have smaller directivity and broader HPBW than identical wedges of smaller dielectric constant material. For TM polarization, wedges of higher dielectric constant have essentially the same directivity and HPBW as those of smaller dielectric constant material. The reflection coefficient of the surface wave on the feed guide was shown to be very small, in particular, for slender wedges of small aperture angles, indicating a low VSWR for

tapered dielectric antennas. The low VSWR over a wide range of operating frequency signifies that the dielectric wedge antenna is a broadband antenna. These results have not been previously proved theoretically [4]. The numerical analysis procedure developed can be applied to a broad class of different shaped dielectric antennas.

APPENDIX A

TABLES FROM NUMERICAL RESULTS

The tables from numerical results in Chapter 4 are shown as follows.

Table A.1 Power Distribution and Magnitude of Reflection Coefficient of the Slab Waveguide/Wedge Antenna in the Region $z<0$ and $z>L$ for $L/\lambda_0 = 5$, TE Polarization, (a) $\varepsilon_r = 2.56$, $D_1/\lambda_0 = 0.2$ and (b) $\varepsilon_r = 12$, $D_1/\lambda_0 = 0.0754$

	Number of slab segments (N_S)			
	10	30	60	90
P_{trans}^{RAD}	0.986187	1.000863	1.000605	1.000389
P_{ref}^{RAD}	7.28×10^{-4}	1.02×10^{-4}	9.22×10^{-5}	9.05×10^{-5}
P_{ref}^{G}	0.015245	7.11×10^{-6}	5.89×10^{-6}	5.68×10^{-6}
P^{TOTAL}	1.002160	1.000972	1.000703	1.000485
$\lvert\Gamma\rvert$	0.123469	0.002667	0.002426	0.002383

(a)

	Number of slab segments (N_S)			
	10	30	60	90
P_{trans}^{RAD}	0.955037	0.997234	1.002474	1.003777
P_{ref}^{RAD}	0.018666	0.001543	0.001450	0.001430
P_{ref}^{G}	0.026814	4.67×10^{-4}	1.75×10^{-4}	1.63×10^{-4}
P^{TOTAL}	1.000516	0.999245	1.004099	1.005370
$\lvert\Gamma\rvert$	0.163749	0.021615	0.013217	0.012786

(b)

Table A.2 Power Distribution and Magnitude of Reflection Coefficient of the Slab Waveguide/Wedge Antenna in the Region $z<0$ and $z>L$ for $L/\lambda_0 = 5$, TM Polarization, (a) $\varepsilon_r = 2.56$, $D_1/\lambda_0 = 0.2$ and (b) $\varepsilon_r = 12$, $D_1/\lambda_0 = 0.0754$

	Number of slab segments (N_S)			
	10	30	60	90
P_{trans}^{RAD}	0.989358	0.997031	0.999595	1.002559
P_{ref}^{RAD}	4.44×10^{-4}	1.75×10^{-5}	1.48×10^{-5}	1.44×10^{-5}
P_{ref}^{G}	0.001992	8.00×10^{-7}	6.66×10^{-7}	6.49×10^{-7}
P^{TOTAL}	0.991793	0.997049	0.999611	1.002574
$\lvert\Gamma\rvert$	0.044627	8.94×10^{-4}	8.16×10^{-4}	8.06×10^{-4}

(a)

	Number of slab segments (N_S)			
	10	30	60	90
P_{trans}^{RAD}	0.986379	1.001650	1.004729	1.003229
P_{ref}^{RAD}	0.016578	3.27×10^{-4}	2.51×10^{-4}	2.40×10^{-4}
P_{ref}^{G}	3.98×10^{-4}	1.34×10^{-4}	5.53×10^{-5}	4.79×10^{-5}
P^{TOTAL}	1.003354	1.002110	1.005036	1.003517
$\lvert\Gamma\rvert$	0.019941	0.011555	0.007436	0.006924

(b)

Table A.3 Power Distribution and Magnitude of Reflection coefficient of the Slab Waveguide/Wedge Antenna in the Region $z<0$ and $z>L$ for $L/\lambda_0=10$, TE Polarization, (a) $\varepsilon_r=2.56$, $D_1/\lambda_0=0.2$ and (b) $\varepsilon_r=12$, $D_1/\lambda_0=0.0754$

	Number of slab segments (N_S)			
	30	60	90	120
P_{trans}^{RAD}	1.000895	1.000707	1.000471	1.000575
P_{ref}^{RAD}	2.95×10^{-5}	1.78×10^{-5}	1.63×10^{-5}	1.58×10^{-5}
P_{ref}^{G}	4.29×10^{-5}	3.23×10^{-6}	2.48×10^{-6}	2.27×10^{-6}
P^{TOTAL}	1.000967	1.000728	1.000490	1.000593
$\lvert\Gamma\rvert$	0.006549	0.001797	0.001573	0.001505

(a)

	Number of slab segments (N_S)			
	30	60	90	120
P_{trans}^{RAD}	0.990417	0.999043	1.000875	1.001626
P_{ref}^{RAD}	5.65×10^{-4}	1.98×10^{-4}	1.85×10^{-4}	1.80×10^{-4}
P_{ref}^{G}	0.013551	4.56×10^{-5}	2.09×10^{-5}	1.95×10^{-5}
P^{TOTAL}	1.004533	0.999287	1.001080	1.001825
$\lvert\Gamma\rvert$	0.116410	0.006753	0.004575	0.004417

(b)

Table A.4 Power Distribution and Magnitude of Reflection Coefficient of the Slab Waveguide/Wedge Antenna in the Region $z<0$ and $z>L$ for $L/\lambda_0=10$, TM Polarization, (a) $\varepsilon_r=2.56$, $D_1/\lambda_0=0.2$ and (b) $\varepsilon_r=12$, $D_1/\lambda_0=0.0754$

	Number of slab segments (N_S)			
	30	60	90	120
P_{trans}^{RAD}	0.997147	0.999979	1.003537	1.004585
P_{ref}^{RAD}	9.90×10^{-6}	4.21×10^{-6}	3.68×10^{-6}	3.52×10^{-6}
P_{ref}^{G}	4.36×10^{-7}	1.35×10^{-7}	1.12×10^{-7}	1.06×10^{-7}
P^{TOTAL}	0.997157	0.999983	1.003541	1.004589
$\lvert\Gamma\rvert$	6.60×10^{-4}	3.67×10^{-4}	3.35×10^{-4}	3.26×10^{-4}

(a)

	Number of slab segments (N_S)			
	30	60	90	120
P_{trans}^{RAD}	0.993121	1.006354	1.004325	1.000130
P_{ref}^{RAD}	2.95×10^{-4}	7.29×10^{-5}	5.84×10^{-5}	5.42×10^{-5}
P_{ref}^{G}	0.008999	3.35×10^{-5}	1.59×10^{-5}	1.26×10^{-5}
P^{TOTAL}	1.002415	1.006460	1.004399	1.000197
$\lvert\Gamma\rvert$	0.094864	0.005785	0.003992	0.003553

(b)

Table A.5 $D_{\max}$, HPBW, P_{ref}^{G} and $|\Gamma|$ of the Slab Waveguide/Wedge Antenna for TE Polarization, (a) $\varepsilon_r = 2.56$, (b) $\varepsilon_r = 12$ and (c) $L/\lambda_0 = 5$

L/λ_0	$D_{\max}$ (dB)	HPBW (degrees)	P_{ref}^{G}	$\|\Gamma\|$
1	7.5190	56.15	0.001849	0.042999
5	9.3470	39.10	5.68×10^{-6}	0.002383
10	10.2542	32.08	2.27×10^{-6}	0.001505
15	10.8825	27.99	9.50×10^{-7}	9.75×10^{-4}
20	11.3382	25.32	1.74×10^{-7}	4.18×10^{-4}

(a)

L/λ_0	$D_{\max}$ (dB)	HPBW (degrees)	P_{ref}^{G}	$\|\Gamma\|$
1	5.6489	88.74	0.020679	0.143803
5	7.7639	56.51	1.63×10^{-4}	0.012786
10	8.7451	45.53	1.95×10^{-5}	0.004417
15	9.2776	40.32	4.75×10^{-6}	0.002179
20	9.7088	36.63	4.35×10^{-6}	0.002085

(b)

ε_r	$D_{\max}$ (dB)	HPBW (degrees)	P_{ref}^{G}	$\|\Gamma\|$
2.56	9.3470	39.10	5.68×10^{-6}	0.002383
5	8.5237	47.43	2.90×10^{-5}	0.005389
8	8.1183	52.16	8.97×10^{-5}	0.009473
12	7.7639	56.51	1.63×10^{-4}	0.012786

(c)

Table A.6 $D_{\max}$, HPBW, SLL, θ_S, P_{ref}^G and $|\Gamma|$ of the Slab Waveguide/Wedge Antenna for TM Polarization, (a) $\varepsilon_r = 2.56$, (b) $\varepsilon_r = 12$ and (c) $L/\lambda_0 = 5$

L/λ_0	$D_{\max}$ (dB)	HPBW (degrees)	SLL (dB)	θ_S (degrees)	P_{ref}^G	$\|\Gamma\|$
1	8.2496	48.69	-	-	7.24×10^{-5}	0.008511
5	10.7165	29.83	-35.9562	54.52	6.49×10^{-7}	8.06×10^{-4}
10	11.6163	24.07	-35.2055	41.76	1.06×10^{-7}	3.26×10^{-4}
15	12.3087	20.54	-35.7266	36.52	3.43×10^{-8}	1.85×10^{-4}
20	12.6140	19.17	-36.4618	33.60	1.42×10^{-8}	1.19×10^{-4}

(a)

L/λ_0	$D_{\max}$ (dB)	HPBW (degrees)	SLL or note below* (dB)	θ_S (degrees)	P_{ref}^G	$\|\Gamma\|$
1	6.5050	71.38	-	-	0.007331	0.085619
5	10.6365	31.25	-35.2723	43.01	4.79×10^{-5}	0.006924
10	11.6670	24.20	-31.5224	31.44	1.26×10^{-5}	0.003553
15	12.3247	20.58	-31.0956	27.41	7.01×10^{-6}	0.002647
20	12.8259	18.33	-31.9879*	25.09	3.94×10^{-6}	0.001985

(b)

*: Shoulder level relative to the main beam maximum.

Table A.6 (Continued) $D_{\max}$, HPBW, SLL, θ_S, P_{ref}^G and $|\Gamma|$ of the Slab Waveguide/Wedge Antenna for TM Polarization, (a) $\varepsilon_r = 2.56$, (b) $\varepsilon_r = 12$ and (c) $L/\lambda_0 = 5$

ε_r	$D_{\max}$ (dB)	HPBW (degrees)	SLL (dB)	θ_S (degrees)	P_{ref}^G	$\|\Gamma\|$
2.56	10.7165	29.83	-35.9562	54.52	6.49×10^{-7}	8.06×10^{-4}
5	10.6670	30.42	-32.9571	52.79	3.43×10^{-6}	0.001851
8	10.6786	30.69	-33.4531	52.79	1.66×10^{-5}	0.004076
12	10.6365	31.25	-35.2723	43.01	4.79×10^{-5}	0.006924

(c)

Table A.7 SLL of the Slab Waveguide/Wedge Antenna for TM Polarization

L/λ_0	ε_r	SLL (dB)	θ_S (degrees)
5	2.56	-35.96	54.52
	12	-35.02	43.01
10	2.56	-35.21	41.76
	12	-31.52	31.44

Table A.8 $D_{\max}$, HPBW, P_{ref}^{G} and $|\Gamma|$ of Antennas Having Profiles Described by a Circle, an Ellipse and a Wedge for $\varepsilon_r = 2.56$ and $D_1/\lambda_0 = 0.2$, for the Ellipse and Wedge $L/\lambda_0 = 10$, (a) TE Polarization and (b) TM Polarization

Profile	$D_{\max}$ (dB)	HPBW (degrees)	P_{ref}^{G}	$\|\Gamma\|$
Circle	7.1555	58.26	0.061764	0.248524
Ellipse	8.5352	44.64	0.002229	0.047210
Wedge	10.2542	32.08	2.27×10^{-6}	0.001505

(a)

Profile	$D_{\max}$ (dB)	HPBW (degrees)	P_{ref}^{G}	$\|\Gamma\|$
Circle	7.8353	50.48	0.015161	0.123128
Ellipse	10.2598	31.66	9.17×10^{-5}	0.009575
Wedge	11.6163	24.07	1.06×10^{-7}	3.26×10^{-4}

(b)

Table A.9 $D_{\max}$, HPBW, P_{ref}^{G} and $|\Gamma|$ of Zucker's Profile Antenna for $L/\lambda_0 = 10$, $L_F/\lambda_0 = L_T/\lambda_0$, TE Polarization, (a) $\varepsilon_r = 2.56$ and (b) $\varepsilon_r = 12$

L_U/λ_0	$D_{\max}$ (dB)	HPBW (degrees)	P_{ref}^{G}	$\|\Gamma\|$
0	10.2542	32.08	2.27×10^{-6}	0.001505
2	9.8853	35.60	3.44×10^{-6}	0.001854
4	9.5348	37.47	1.06×10^{-5}	0.003263

(a)

L_U/λ_0	$D_{\max}$ (dB)	HPBW (degrees)	P_{ref}^{G}	$\|\Gamma\|$
0	8.7451	45.53	1.95×10^{-5}	0.004417
2	8.4047	49.27	7.74×10^{-5}	0.008797
4	8.0211	53.26	1.41×10^{-4}	0.011892

(b)

Table A.10 $D_{\max}$, HPBW, SLL, θ_S, P_{ref}^G and $|\Gamma|$ of Zucker's Profile Antenna for $L/\lambda_0 = 10$, $L_F/\lambda_0 = L_T/\lambda_0$, TM Polarization, (a) $\varepsilon_r = 2.56$ and (b) $\varepsilon_r = 12$

L_U/λ_0	$D_{\max}$ (dB)	HPBW (degrees)	SLL or note below* (dB)	θ_S	P_{ref}^G	$\|\Gamma\|$
0	11.6163	24.07	-35.2055	41.76	1.06×10^{-7}	3.26×10^{-4}
2	11.6851	21.72	-31.9610	43.80	6.82×10^{-7}	8.26×10^{-4}
4	11.3321	20.54	-20.7825*	38.87	1.96×10^{-6}	0.001399

(a)

* : Fluctuation relative to the main beam maximum.

L_U/λ_0	$D_{\max}$ (dB)	HPBW (degrees)	SLL (dB)	θ_S	P_{ref}^G	$\|\Gamma\|$
0	11.6670	24.20	-31.5224	31.44	1.26×10^{-5}	0.003553
2	12.2341	21.07	-15.7491	29.98	2.07×10^{-5}	0.004547
4	12.6090	18.39	-10.8439	26.54	3.38×10^{-5}	0.005818

(b)

Table A.11 $D_{\max}$, HPBW, P_{ref}^{G} and $|\Gamma|$ of Zucker's Profile Antenna for $L_F/\lambda_0 = L_T/\lambda_0 = 5$, TE Polarization, (a) $\varepsilon_r = 2.56$ and (b) $\varepsilon_r = 12$

L_U/λ_0	$D_{\max}$ (dB)	HPBW (degrees)	P_{ref}^{G}	$\|\Gamma\|$
0	10.2542	32.08	2.27×10^{-6}	0.001505
2.5	10.3285	31.24	5.36×10^{-6}	0.002315
5	10.2239	32.83	6.20×10^{-6}	0.002490
7.5	10.2966	32.24	3.39×10^{-6}	0.001842

(a)

L_U/λ_0	$D_{\max}$ (dB)	HPBW (degrees)	P_{ref}^{G}	$\|\Gamma\|$
0	8.7451	45.53	1.95×10^{-5}	0.004417
2.5	8.7277	45.52	1.98×10^{-5}	0.004449
5	8.7288	45.48	2.02×10^{-5}	0.004490
7.5	8.7289	45.62	2.07×10^{-5}	0.004550

(b)

Table A.12 $D_{\max}$, HPBW, SLL, θ_S, P_{ref}^G and $|\Gamma|$ of Zucker's Profile Antenna for $L_F/\lambda_0 = L_T/\lambda_0 = 5$, TM Polarization, (a) $\varepsilon_r = 2.56$ and (b) $\varepsilon_r = 12$

L_U/λ_0	$D_{\max}$ (dB)	HPBW (degrees)	SLL (dB)	θ_S (degrees)	P_{ref}^G	$\|\Gamma\|$
0	11.6163	24.07	-35.2055	41.76	1.06×10^{-7}	3.26×10^{-4}
2.5	11.7531	21.19	-30.6676	41.26	9.58×10^{-7}	9.79×10^{-4}
5	11.2601	26.04	-28.2660	41.86	6.30×10^{-7}	7.94×10^{-4}
7.5	11.0081	29.27	-27.4508	43.05	3.81×10^{-7}	6.17×10^{-4}

(a)

L_U/λ_0	$D_{\max}$ (dB)	HPBW (degrees)	SLL (dB)	θ_S (degrees)	P_{ref}^G	$\|\Gamma\|$
0	11.6670	24.20	-31.5224	31.44	1.26×10^{-5}	0.003553
2.5	12.5125	19.32	-14.4575	25.74	1.32×10^{-5}	0.003633
5	12.9205	16.15	-9.6744	21.43	1.35×10^{-5}	0.003676
7.5	12.9656	14.20	-6.9008	17.86	1.32×10^{-5}	0.003628

(b)

APPENDIX B

FIGURES FROM NUMERICAL RESULTS

The figures from numerical results in Chapter 4 are shown as follows.

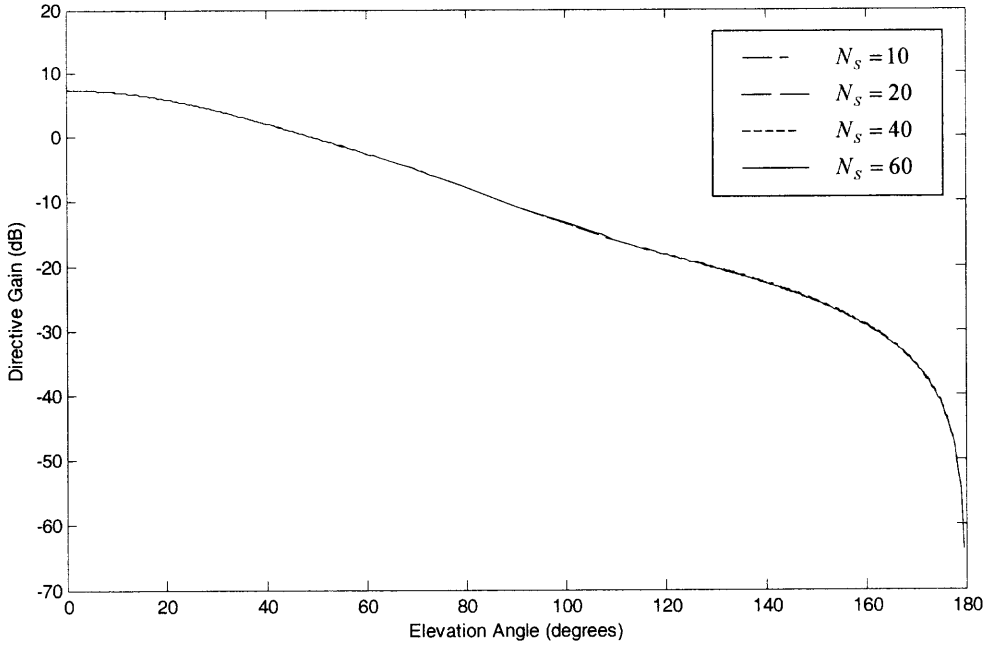

Figure B.1 Directive gain versus elevation angle (θ) of the slab waveguide/wedge antenna for $\varepsilon_r = 2.56$, $D_1/\lambda_0 = 0.2$, $L/\lambda_0 = 1$, for different number of slab segments (N_S), using $u_{\max} = 2k_0$ and $N = 300$ ($N_P = 150$, $N_E = 150$), TE polarization.

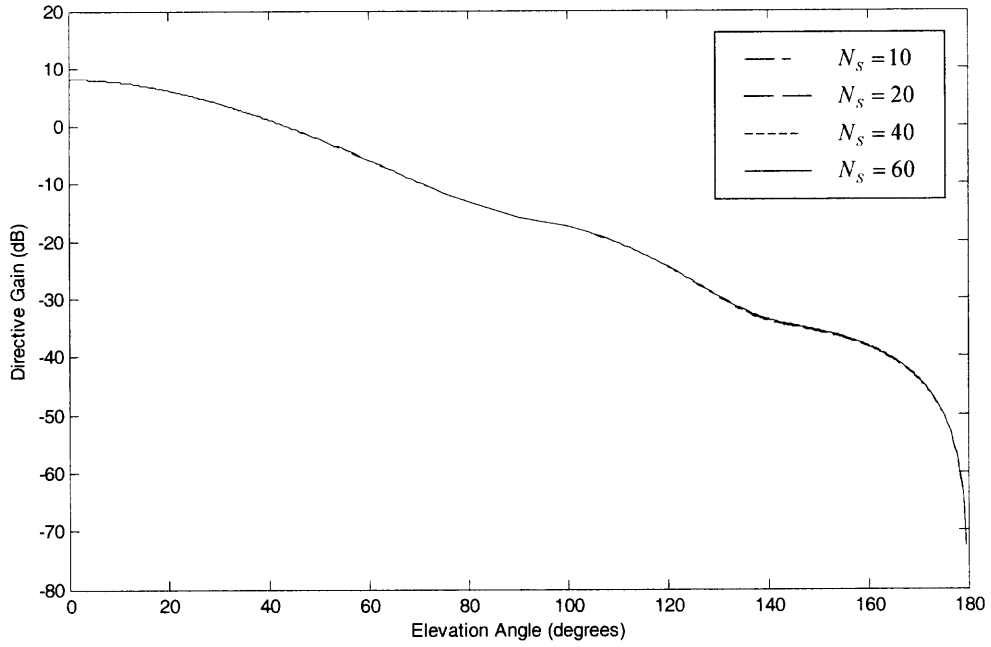

Figure B.2 Directive gain versus elevation angle (θ) of the slab waveguide/wedge antenna for $\varepsilon_r = 2.56$, $D_1/\lambda_0 = 0.2$, $L/\lambda_0 = 1$, for different number of slab segments (N_S), using $u_{\max} = 2k_0$ and $N = 300$ ($N_P = 150$, $N_E = 150$), TM polarization.

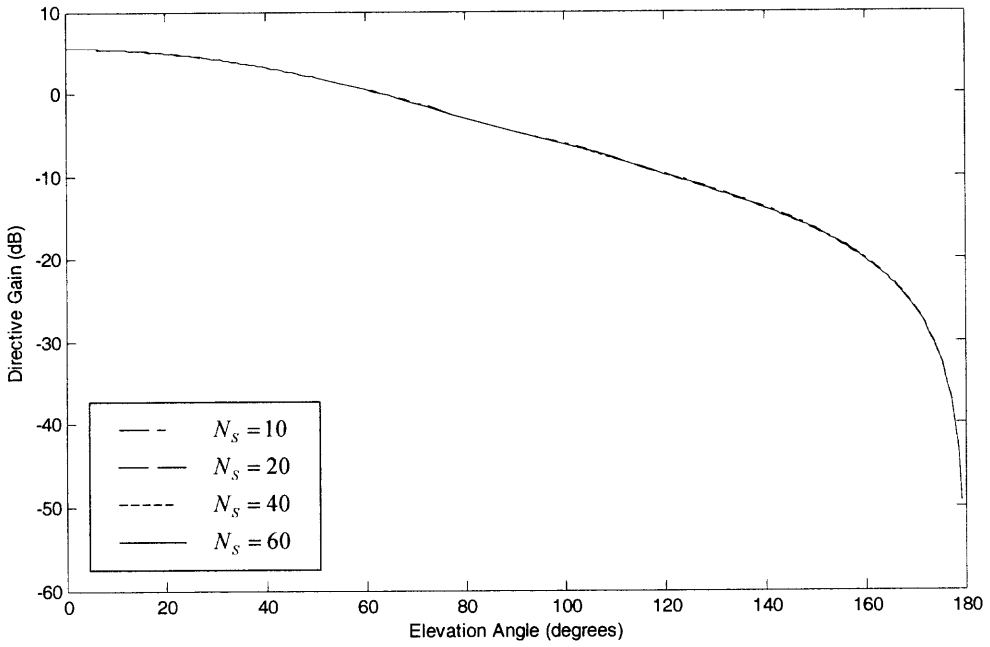

Figure B.3 Directive gain versus elevation angle (θ) of the slab waveguide/wedge antenna for $\varepsilon_r = 12$, $D_1/\lambda_0 = 0.0754$, $L/\lambda_0 = 1$, for different number of slab segments (N_S), using $u_{\max} = 2k_0$ and $N = 230$ ($N_P = 80$, $N_E = 150$), TE polarization.

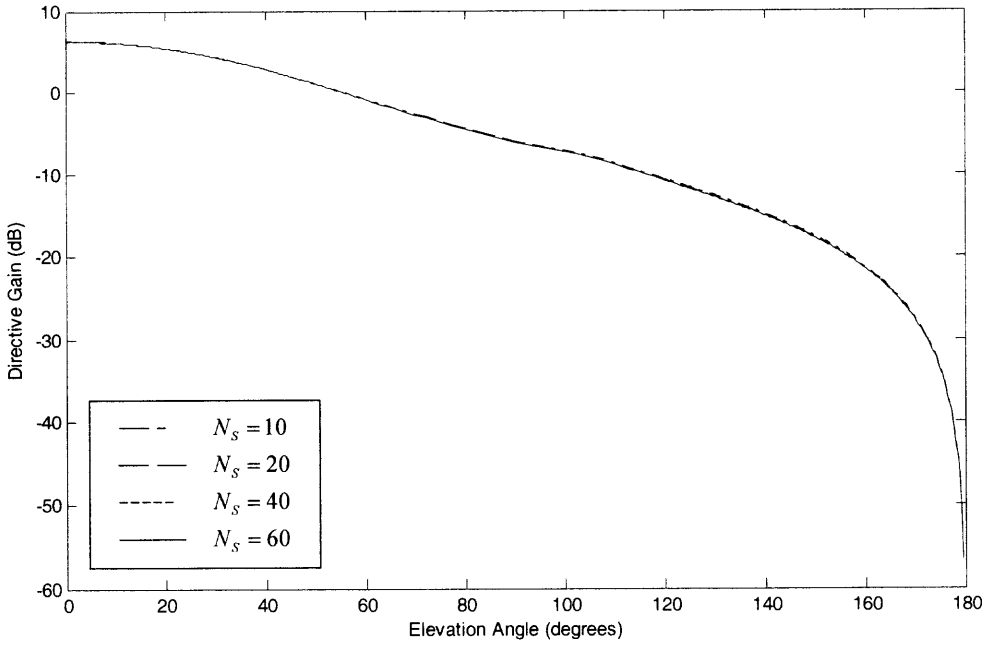

Figure B.4 Directive gain versus elevation angle (θ) of the slab waveguide/wedge antenna for $\varepsilon_r = 12$, $D_1/\lambda_0 = 0.0754$, $L/\lambda_0 = 1$, for different number of slab segments (N_S), using $u_{\max} = 2k_0$ and $N = 300$ ($N_P = 150$, $N_E = 150$), TM polarization.

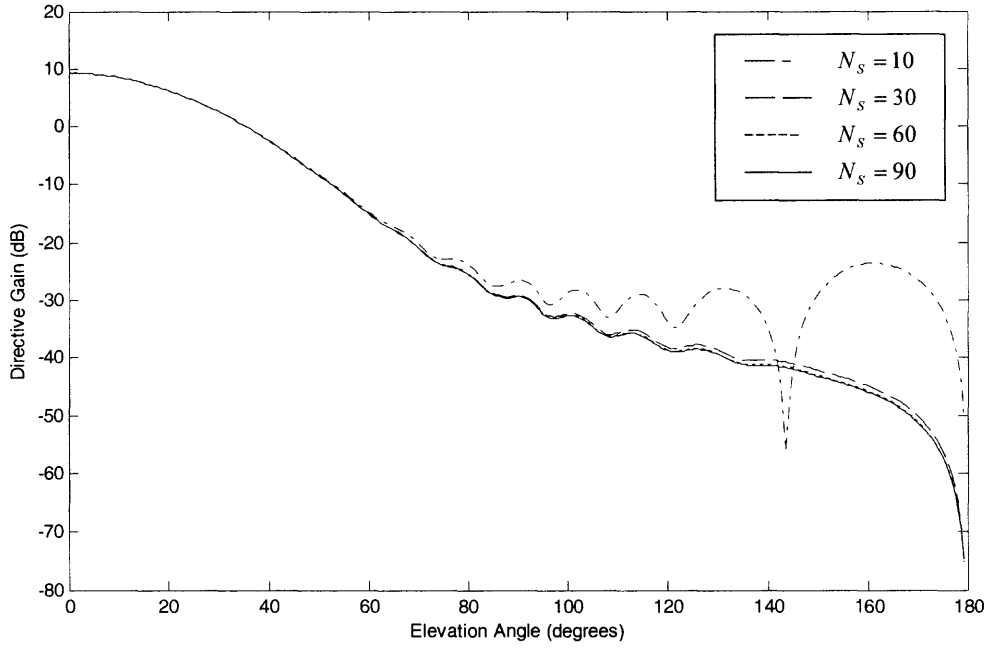

Figure B.5 Directive gain versus elevation angle (θ) of the slab waveguide/wedge antenna for $\varepsilon_r = 2.56$, $D_1/\lambda_0 = 0.2$, $L/\lambda_0 = 5$, for different number of slab segments (N_S), using $u_{\max} = 2k_0$ and $N = 300$ ($N_P = 150$, $N_E = 150$), TE polarization.

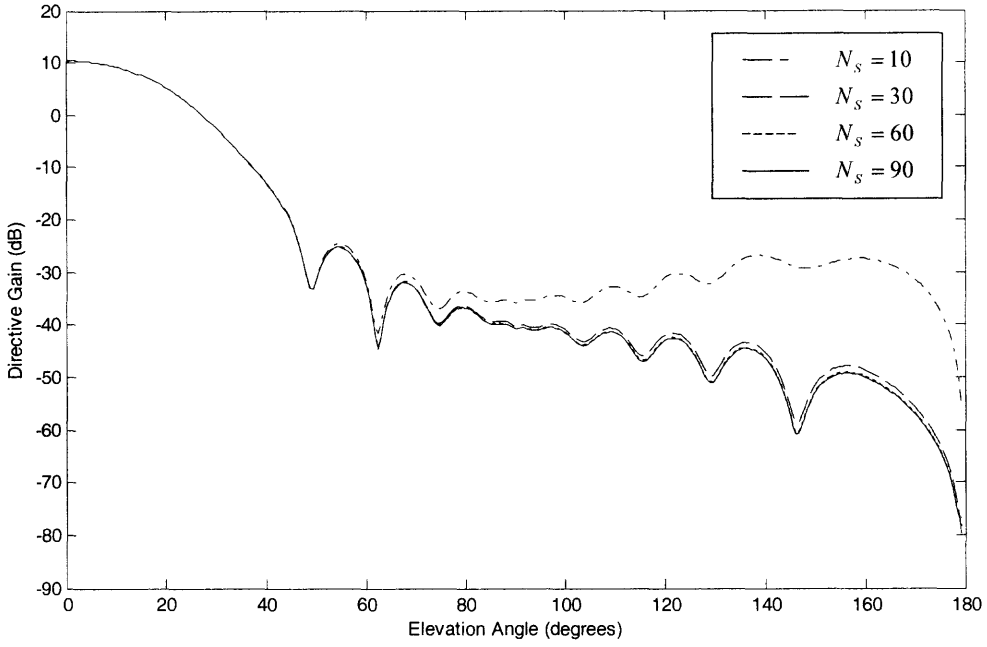

Figure B.6 Directive gain versus elevation angle (θ) of the slab waveguide/wedge antenna for $\varepsilon_r = 2.56$, $D_1/\lambda_0 = 0.2$, $L/\lambda_0 = 5$, for different number of slab segments (N_S), using $u_{\max} = 2k_0$ and $N = 300$ ($N_P = 150$, $N_E = 150$), TM polarization.

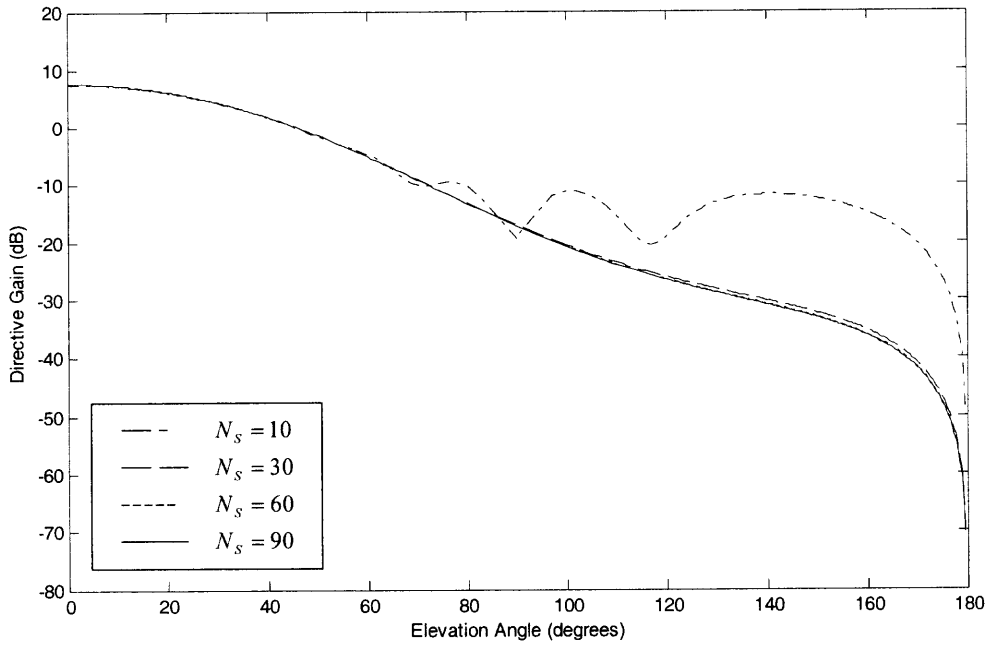

Figure B.7 Directive gain versus elevation angle (θ) of the slab waveguide/wedge antenna for $\varepsilon_r = 12$, $D_1/\lambda_0 = 0.0754$, $L/\lambda_0 = 5$, for different number of slab segments (N_S), using $u_{\max} = 2k_0$ and $N = 300$ ($N_P = 150$, $N_E = 150$), TE polarization.

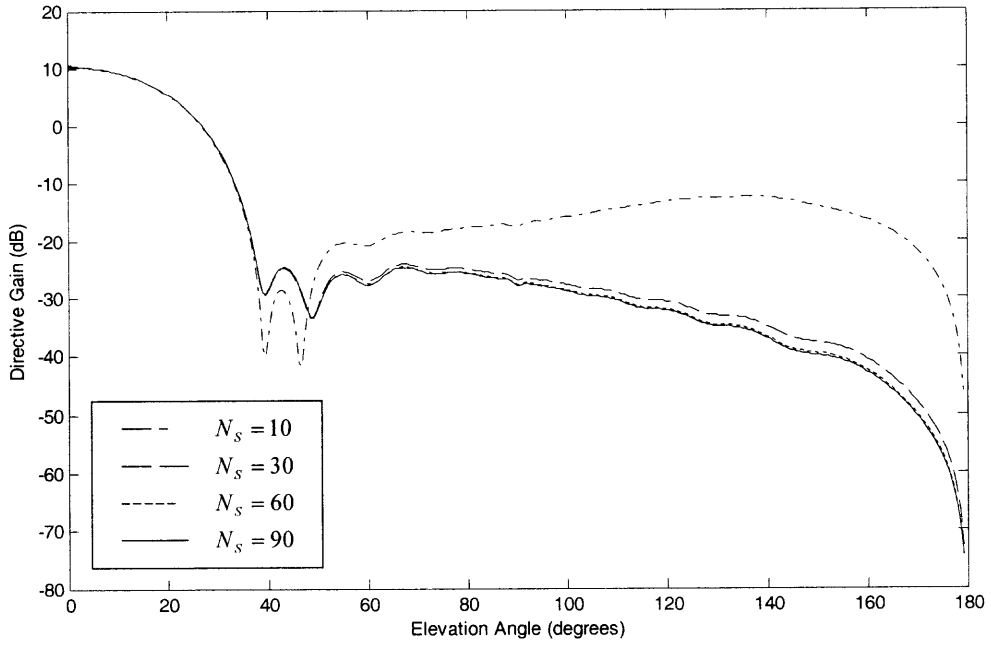

Figure B.8 Directive gain versus elevation angle (θ) of the slab waveguide/wedge antenna for $\varepsilon_r = 12$, $D_1/\lambda_0 = 0.0754$, $L/\lambda_0 = 5$, for different number of slab segments (N_S), using $u_{\max} = 2k_0$ and $N = 300$ ($N_P = 150$, $N_E = 150$), TM polarization.

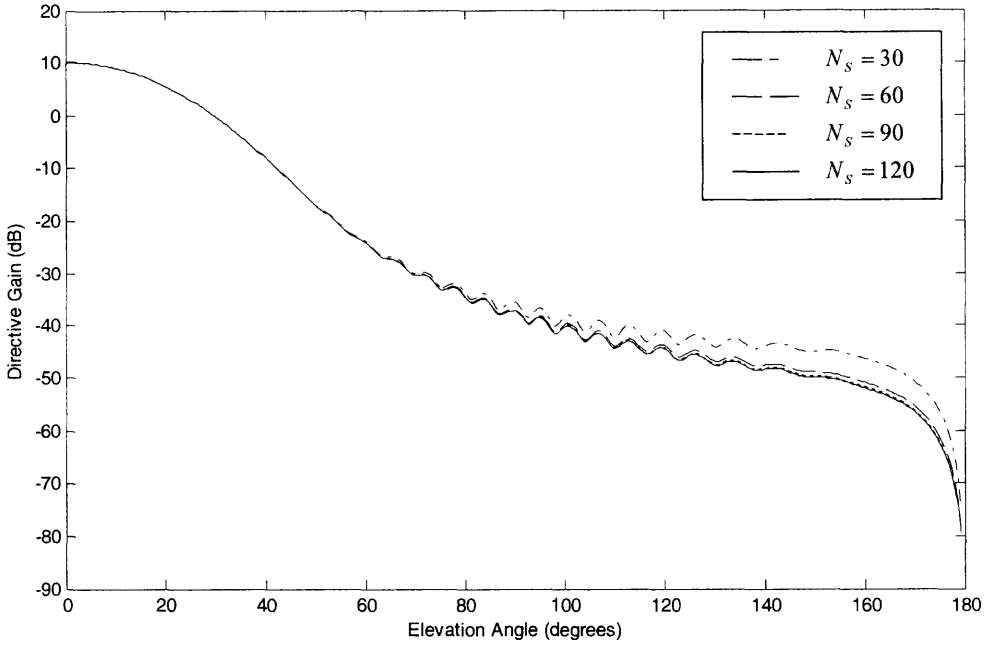

Figure B.9 Directive gain versus elevation angle (θ) of the slab waveguide/wedge antenna for $\varepsilon_r = 2.56$, $D_1/\lambda_0 = 0.2$, $L/\lambda_0 = 10$, for different number of slab segments (N_S), using $u_{\max} = 2k_0$ and $N = 300$ ($N_P = 150$, $N_E = 150$), TE polarization.

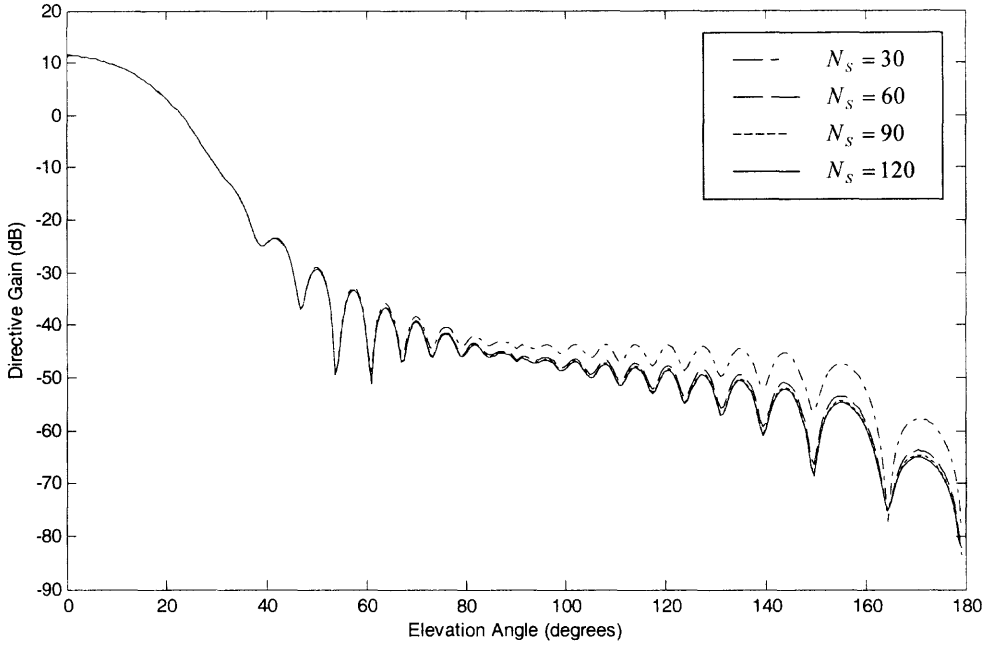

Figure B.10 Directive gain versus elevation angle (θ) of the slab waveguide/wedge antenna for $\varepsilon_r = 2.56$, $D_1/\lambda_0 = 0.2$, $L/\lambda_0 = 10$, for different number of slab segments (N_S), using $u_{\max} = 2k_0$ and $N = 300$ ($N_P = 150$, $N_E = 150$), TM polarization.

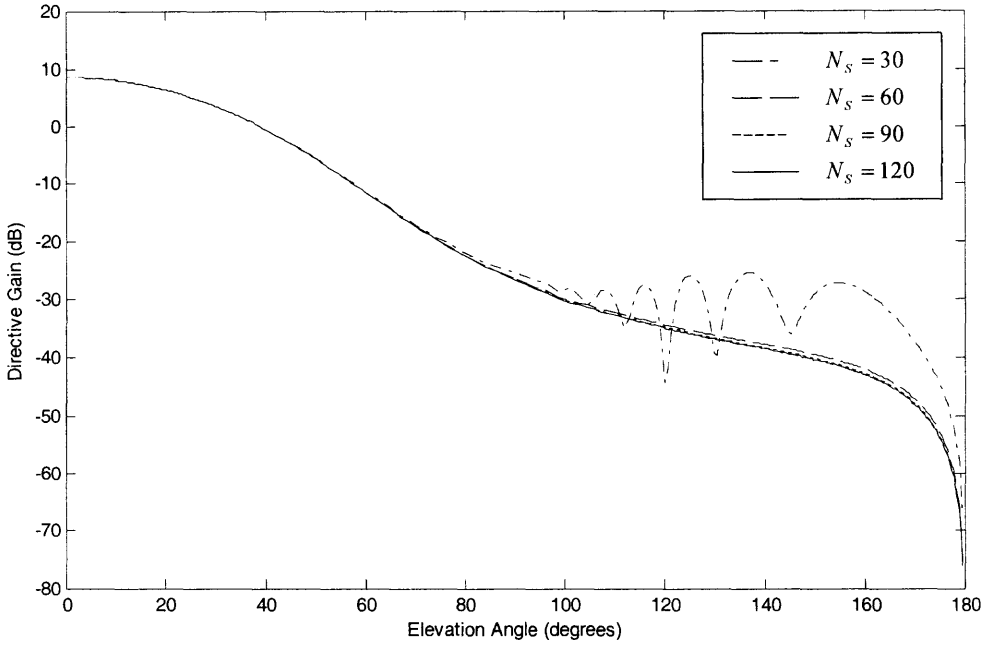

Figure B.11 Directive gain versus elevation angle (θ) of the slab waveguide/wedge antenna for $\varepsilon_r = 12$, $D_1/\lambda_0 = 0.0754$, $L/\lambda_0 = 10$, for different number of slab segments (N_S), using $u_{\max} = 2k_0$ and $N = 300$ ($N_P = 150$, $N_E = 150$), TE polarization.

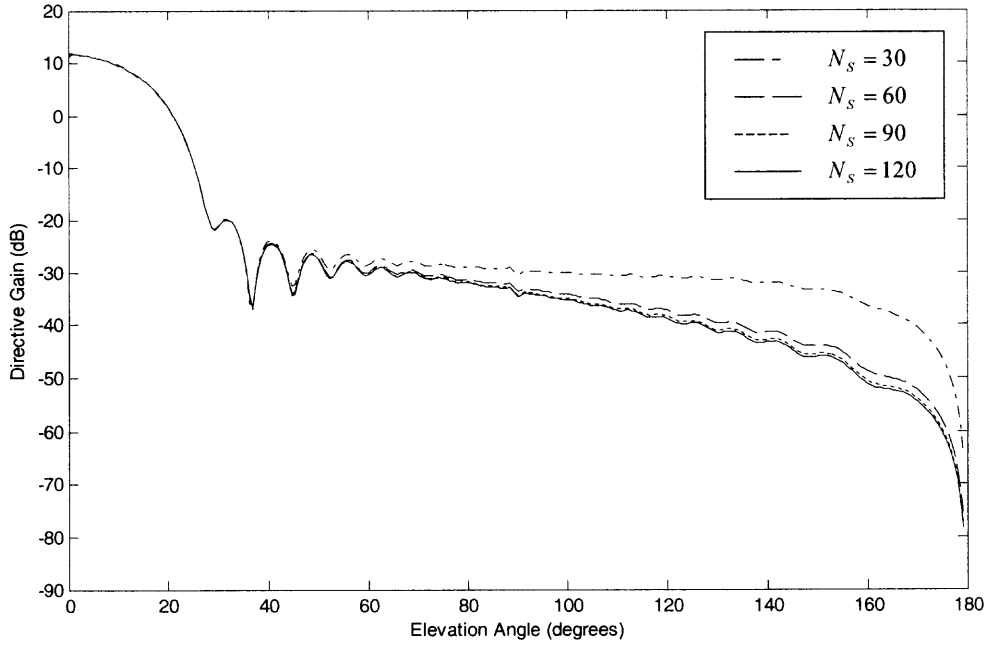

Figure B.12 Directive gain versus elevation angle (θ) of the slab waveguide/wedge antenna for $\varepsilon_r = 12$, $D_1/\lambda_0 = 0.0754$, $L/\lambda_0 = 10$, for different number of slab segments (N_S), using $u_{\max} = 2k_0$ and $N = 300$ ($N_P = 150$, $N_E = 150$), TM polarization.

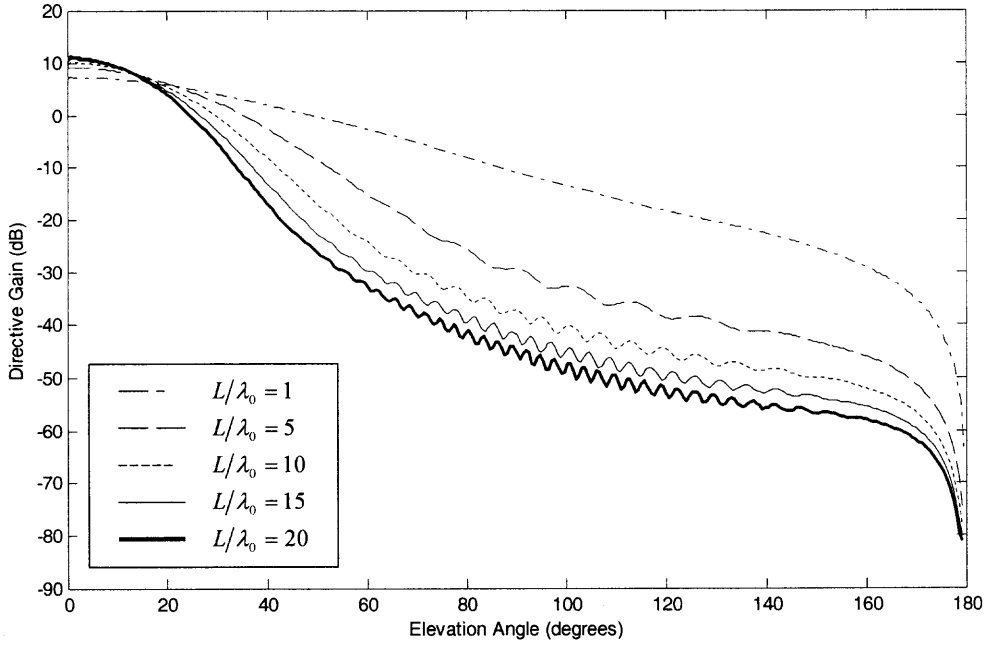

Figure B.13 Directive gain versus elevation angle (θ) of the slab waveguide/wedge antenna for $\varepsilon_r = 2.56$, $D_1/\lambda_0 = 0.2$ and $u_{\max} = 2k_0$, for different L, for $L/\lambda_0 = 1$, 5, 10, 15 and 20 using $N_S = 60$, 90, 120, 150 and 180 respectively, TE polarization.

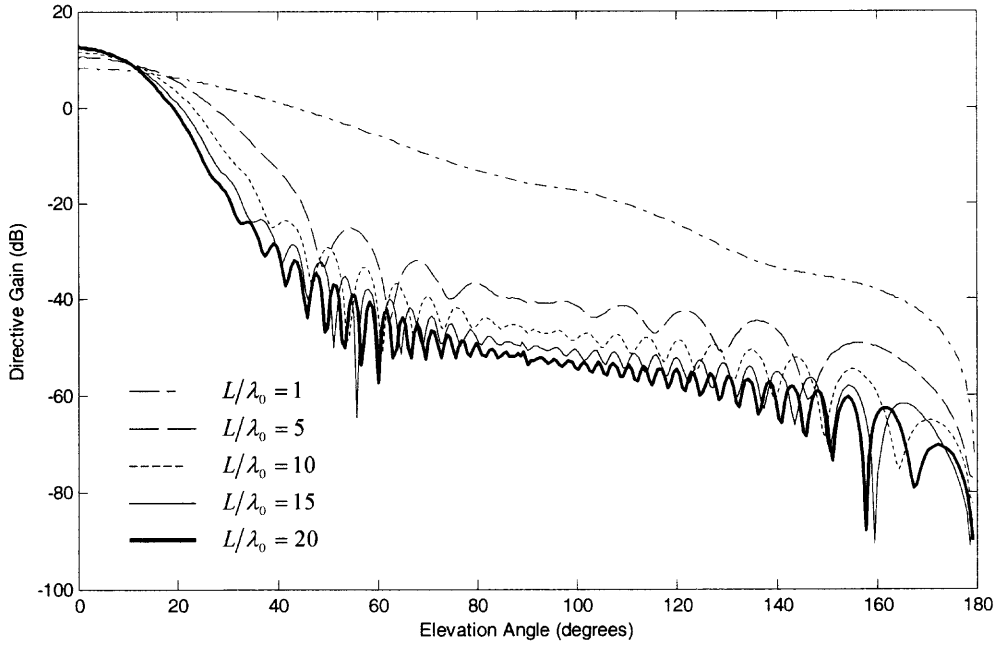

Figure B.14 Directive gain versus elevation angle (θ) of the slab waveguide/wedge antenna for $\varepsilon_r = 2.56$, $D_1/\lambda_0 = 0.2$ and $u_{\max} = 2k_0$, for different L, for $L/\lambda_0 = 1$, 5, 10, 15 and 20 using $N_S = 60$, 90, 120, 150 and 180 respectively, TM polarization.

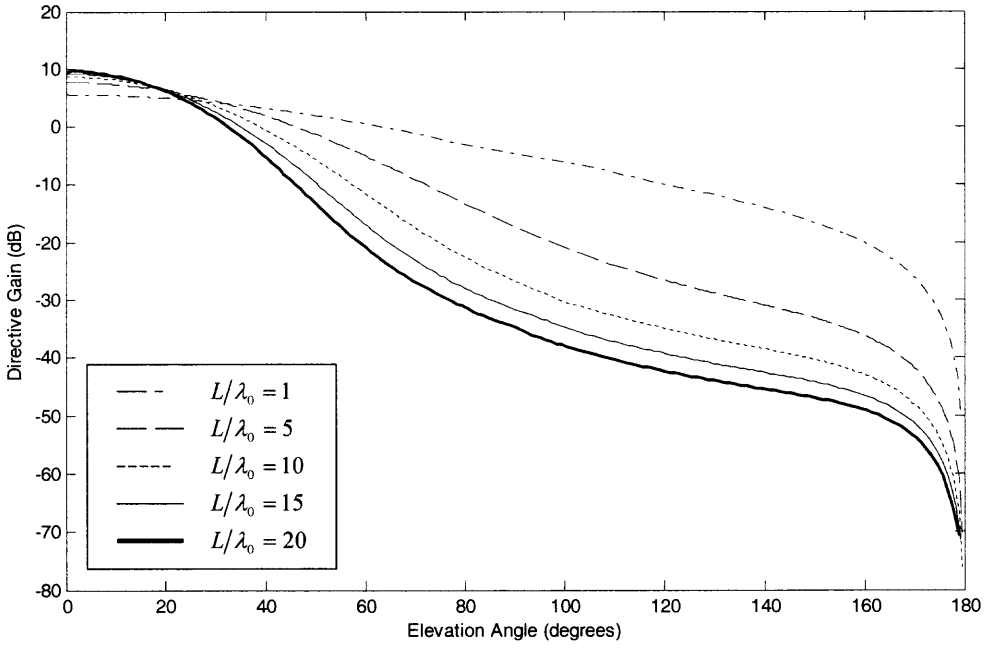

Figure B.15 Directive gain versus elevation angle (θ) of the slab waveguide/wedge antenna for $\varepsilon_r = 12$, $D_1/\lambda_0 = 0.0754$ and $u_{\max} = 2k_0$, for different L, for $L/\lambda_0 = 1$, 5, 10, 15 and 20 using $N_S = 60$, 90, 120, 150 and 180 respectively, TE polarization.

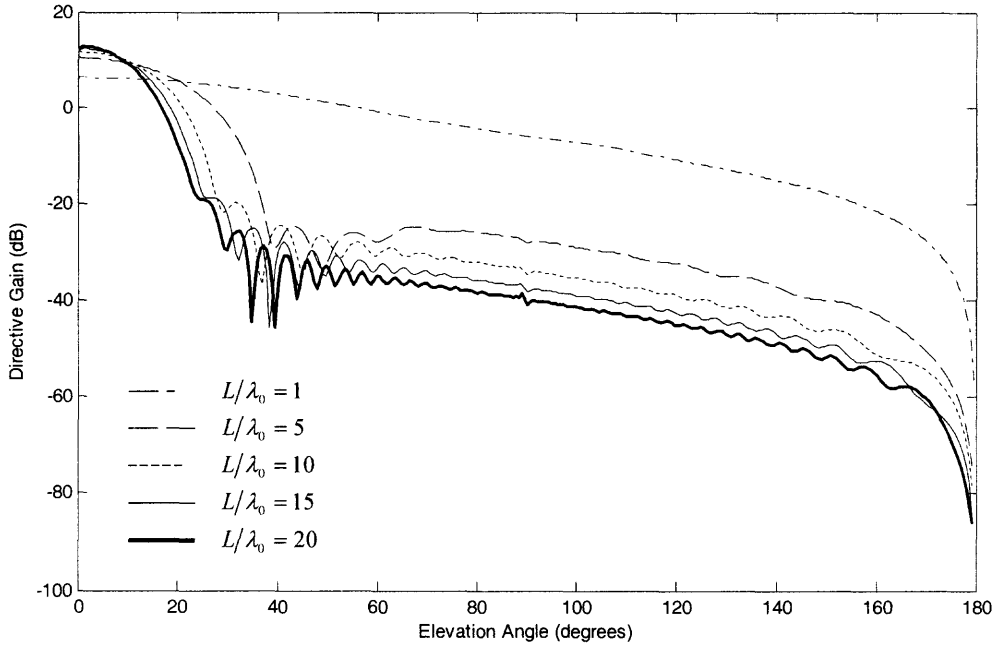

Figure B.16 Directive gain versus elevation angle (θ) of the slab waveguide/wedge antenna for $\varepsilon_r = 12$, $D_1/\lambda_0 = 0.0754$ and $u_{\max} = 2k_0$, for different L, for $L/\lambda_0 = 1$, 5, 10, 15 and 20 using $N_S = 60$, 90, 120, 150 and 180 respectively, TM polarization.

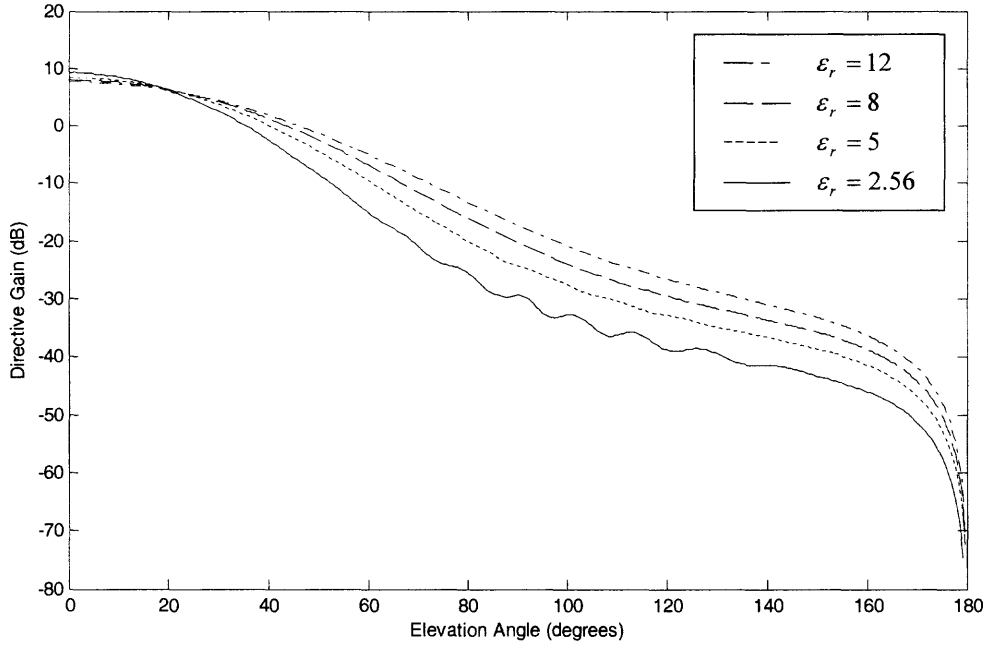

Figure B.17 Directive gain versus elevation angle (θ) of the slab waveguide/wedge antenna for $L/\lambda_0 = 5$ and $\varepsilon_r = 2.56$, 5, 8 and 12 ($D_1/\lambda_0 = 0.2$, 0.125, 0.0945, 0.0754 respectively), using $u_{\max} = 2k_0$ and $N_S = 90$, TE polarization.

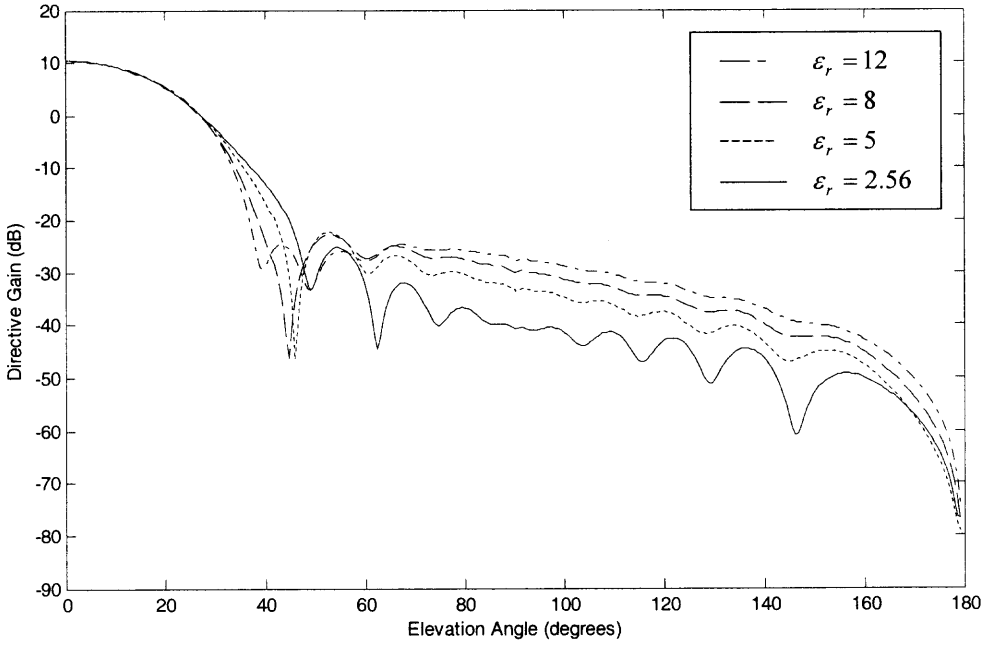

Figure B.18 Directive gain versus elevation angle (θ) of the slab waveguide/wedge antenna for $L/\lambda_0 = 5$ and $\varepsilon_r = 2.56$, 5, 8 and 12 ($D_1/\lambda_0 = 0.2$, 0.125, 0.0945, 0.0754 respectively), using $u_{\max} = 2k_0$ and $N_S = 90$, TM polarization.

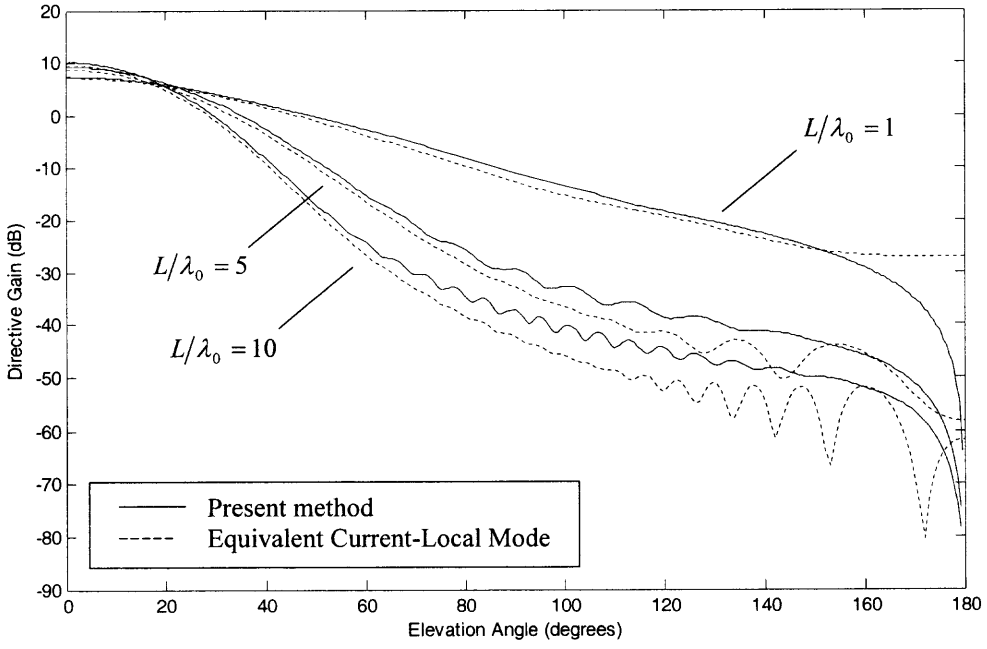

Figure B.19 Directive gain versus elevation angle (θ) of the slab waveguide/wedge antenna for $\varepsilon_r = 2.56$, $D_1/\lambda_0 = 0.2$, $L/\lambda_0 = 1$, 5 and 10, using the equivalent current-local mode and the present method with $u_{\max} = 2k_0$, for $L/\lambda_0 = 1$, 5 and 10 using $N_S = 60$, 90 and 120 respectively, TE polarization.

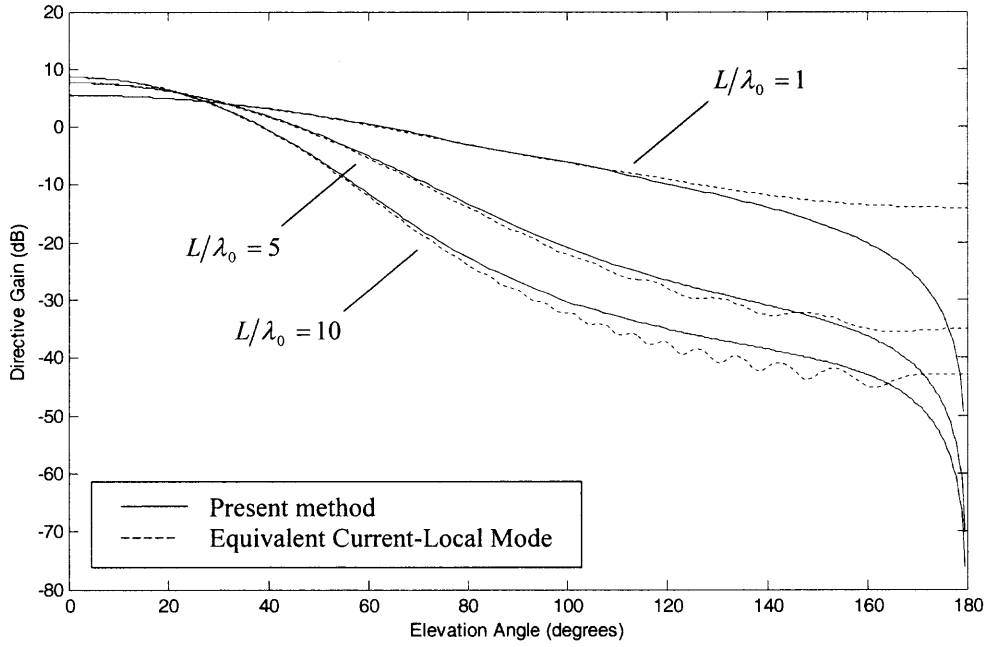

Figure B.20 Directive gain versus elevation angle (θ) of the slab waveguide/wedge antenna for $\varepsilon_r = 12$, $D_1/\lambda_0 = 0.0754$, $L/\lambda_0 = 1$, 5 and 10, using the equivalent current-local mode and the present method with $u_{\max} = 2k_0$, for $L/\lambda_0 = 1$, 5 and 10 using $N_S = 60$, 90 and 120 respectively, TE polarization.

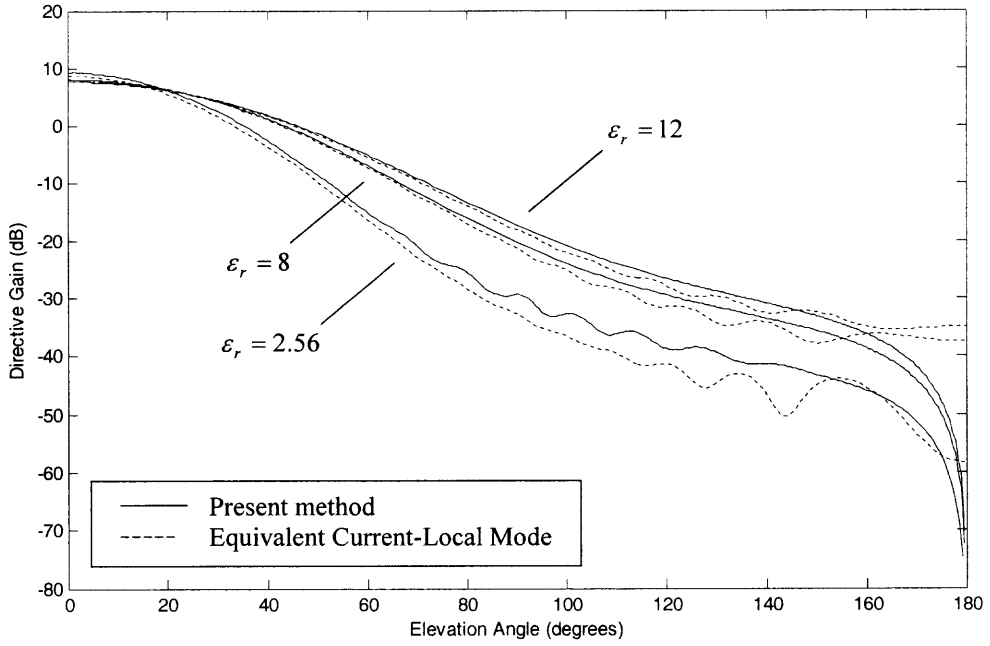

Figure B.21 Directive gain versus elevation angle (θ) of the slab waveguide/wedge antenna for $L/\lambda_0 = 5$, $\varepsilon_r = 2.56$, 8 and 12, using the equivalent current-local mode and the present method with $u_{\max} = 2k_0$ and $N_S = 90$, TE polarization.

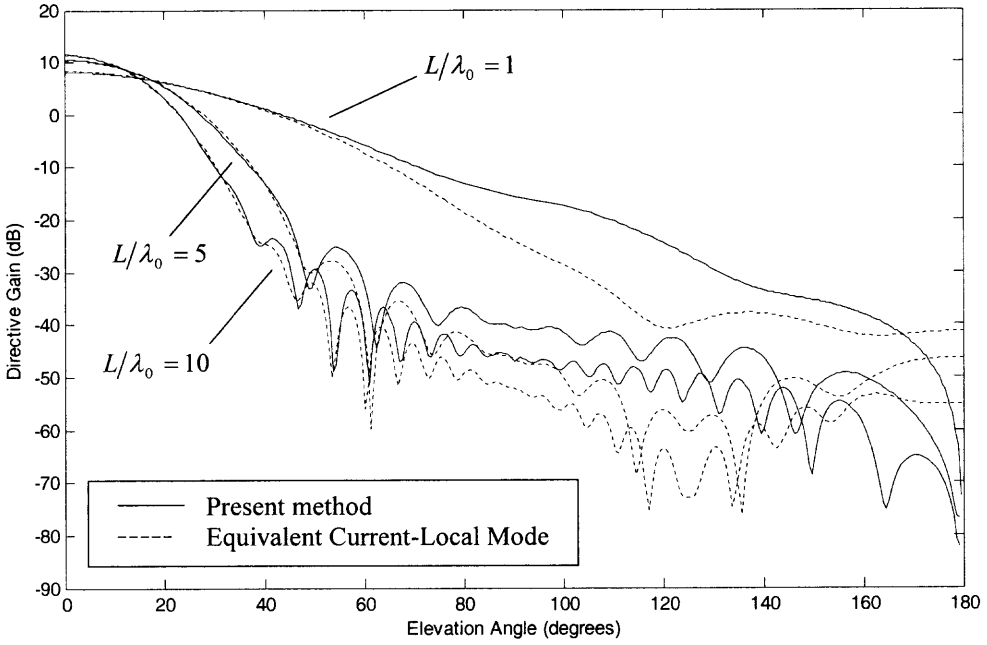

Figure B.22 Directive gain versus elevation angle (θ) of the slab waveguide/wedge antenna for $\varepsilon_r = 2.56$, $D_1/\lambda_0 = 0.2$, $L/\lambda_0 = 1$, 5 and 10, using the equivalent current-local mode and the present method with $u_{\max} = 2k_0$, for $L/\lambda_0 = 1$, 5 and 10 using $N_S = 60$, 90 and 120 respectively, TM polarization.

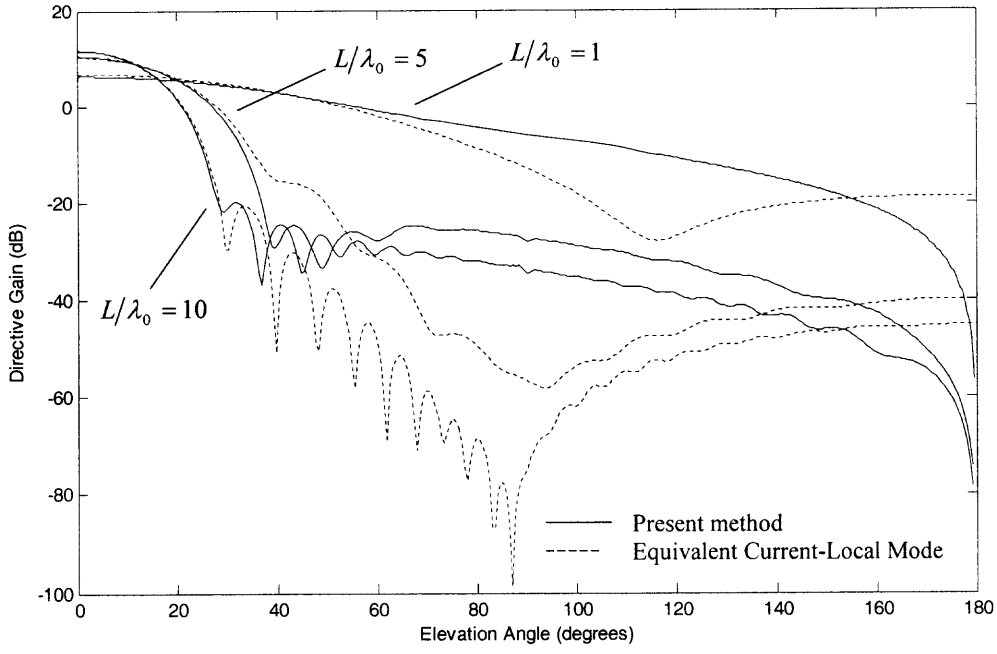

Figure B.23 Directive gain versus elevation angle (θ) of the slab waveguide/wedge antenna for $\varepsilon_r = 12$, $D_1/\lambda_0 = 0.0754$, $L/\lambda_0 = 1$, 5 and 10, using the equivalent current-local mode and the present method with $u_{\max} = 2k_0$, for $L/\lambda_0 = 1$, 5 and 10 using $N_S = 60$, 90 and 120 respectively, TM polarization.

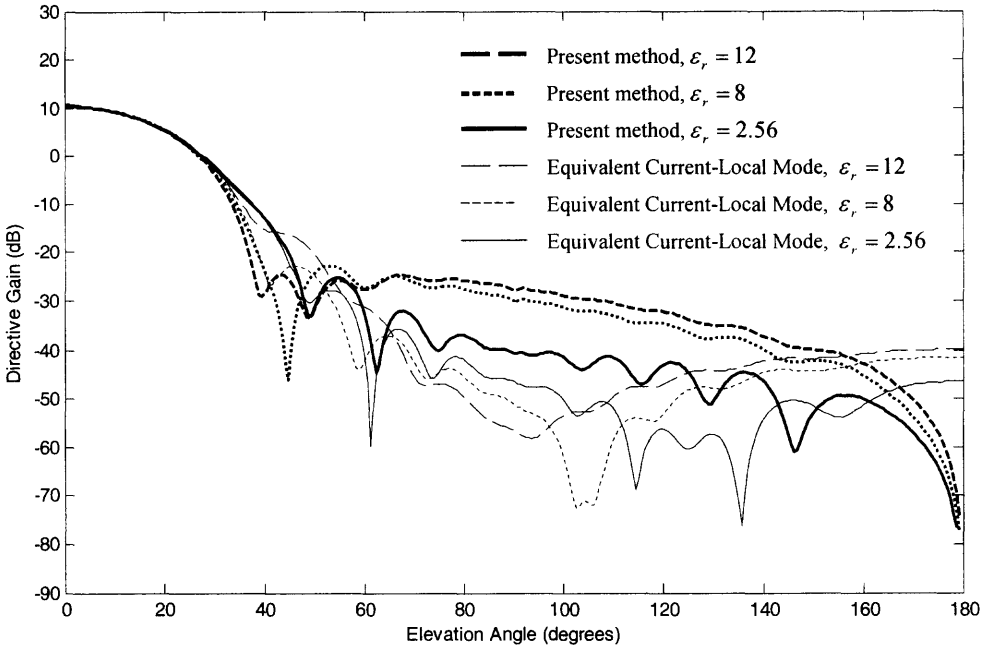

Figure B.24 Directive gain versus elevation angle (θ) of the slab waveguide/wedge antenna for $L/\lambda_0 = 5$, $\varepsilon_r = 2.56$, 8 and 12, using the equivalent current-local mode and the present method with $u_{\max} = 2k_0$ and $N_S = 90$, TM polarization.

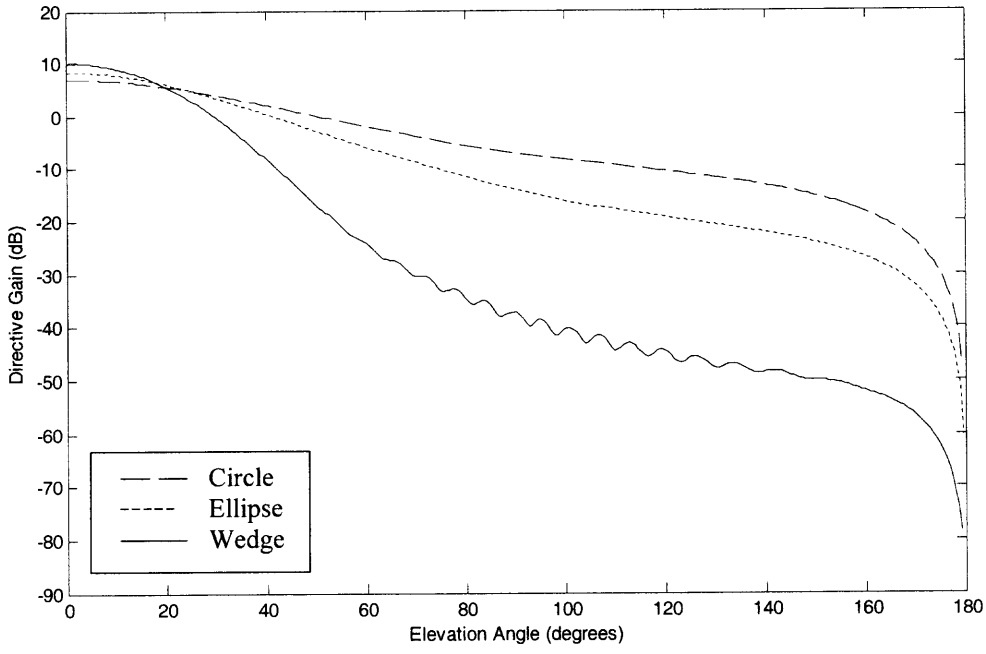

Figure B.25 Directive gain versus elevation angle (θ) for dielectric antennas having profiles described by a circle, an ellipse and a wedge for $\varepsilon_r = 2.56$, $D_1/\lambda_0 = 0.2$, for the circle using $N_S = 10$, for the ellipse and wedge using $L/\lambda_0 = 10$, $N_s = 90$ and 120 respectively, in all cases using $u_{\max} = 2k_0$, TE polarization.

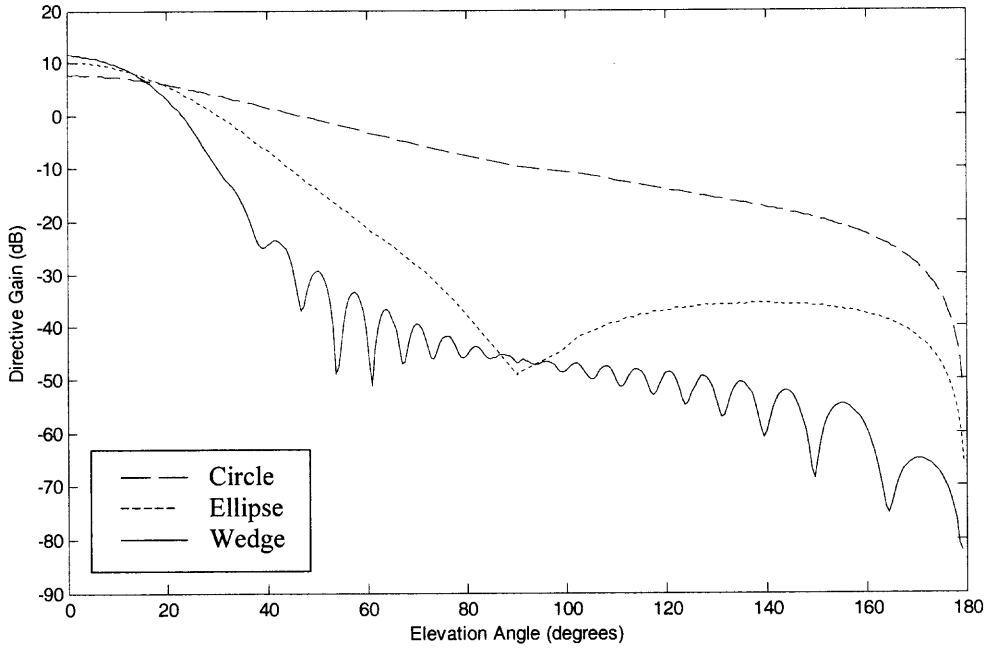

Figure B.26 Directive gain versus elevation angle (θ) for dielectric antennas having profiles described by a circle, an ellipse and a wedge for $\varepsilon_r = 2.56$, $D_1/\lambda_0 = 0.2$, for the circle using $N_S = 10$, for the ellipse and wedge using $L/\lambda_0 = 10$, $N_s = 90$ and 120 respectively, in all cases using $u_{\max} = 2k_0$, TM polarization.

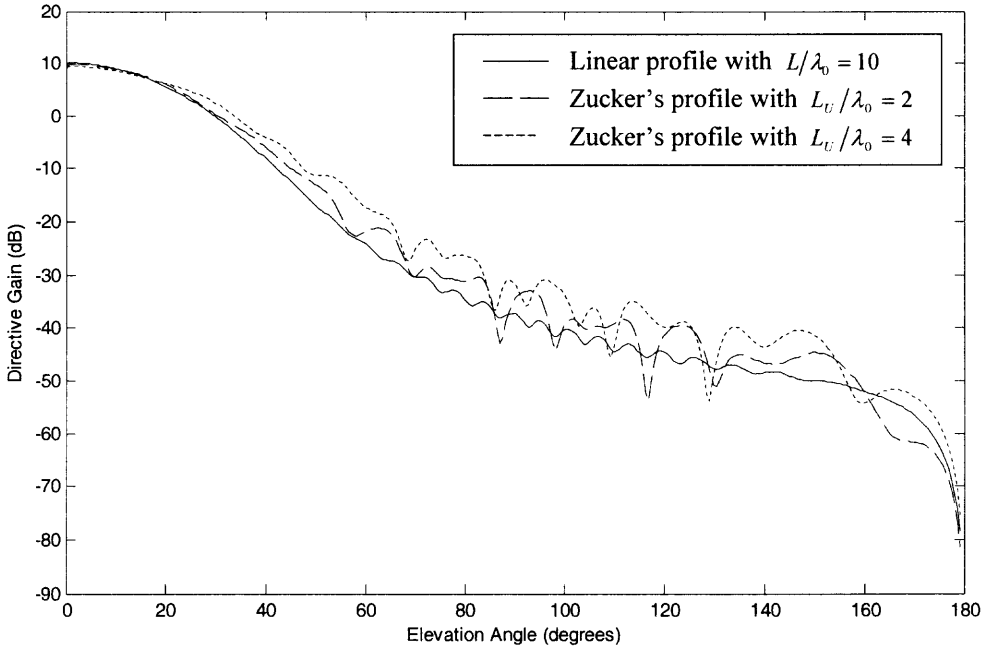

Figure B.27 Directive gain versus elevation angle (θ) of the antennas for $\varepsilon_r = 2.56$, $D_1/\lambda_0 = 0.2$, $L/\lambda_0 = 10$ having linear profile and Zucker's profile with $L_F = L_T$ and $L_U/\lambda_0 = 2$ and 4, for linear case using $N_S = 120$, for Zucker case with $L_U/\lambda_0 = 2$ and 4 using $N_S = 107$ and 95 respectively, TE polarization.

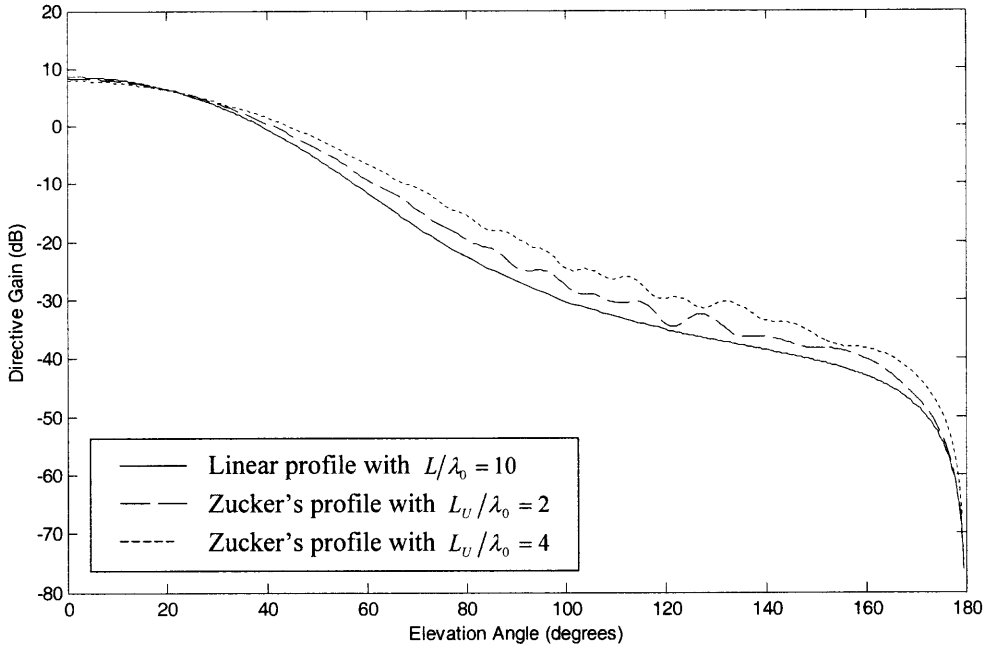

Figure B.28 Directive gain versus elevation angle (θ) of the antennas for $\varepsilon_r = 12$, $D_1/\lambda_0 = 0.0754$, $L/\lambda_0 = 10$ having linear profile and Zucker's profile with $L_F = L_T$ and $L_U/\lambda_0 = 2$ and 4, for linear case using $N_S = 120$, for Zucker case with $L_U/\lambda_0 = 2$ and 4 using $N_S = 107$ and 95 respectively, TE polarization.

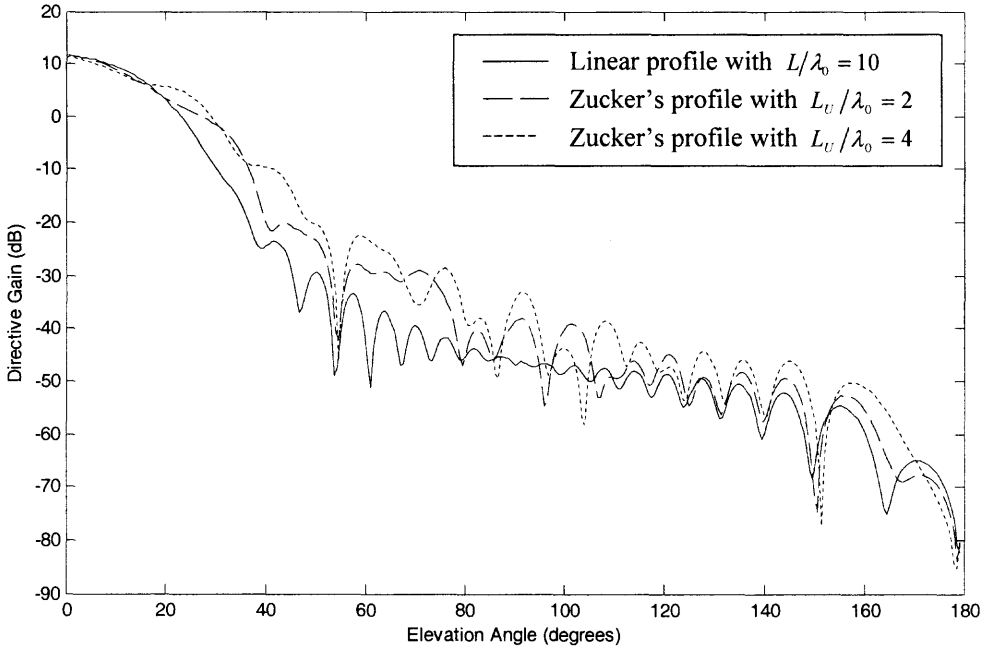

Figure B.29 Directive gain versus elevation angle (θ) of the antennas for $\varepsilon_r = 2.56$, $D_1/\lambda_0 = 0.2$ and $L/\lambda_0 = 10$ having linear profile and Zucker's profile with $L_F = L_T$ and $L_U/\lambda_0 = 2$ and 4, for linear case using $N_S = 120$, for Zucker case with $L_U/\lambda_0 = 2$ and 4 using $N_S = 107$ and 95 respectively, TM polarization.

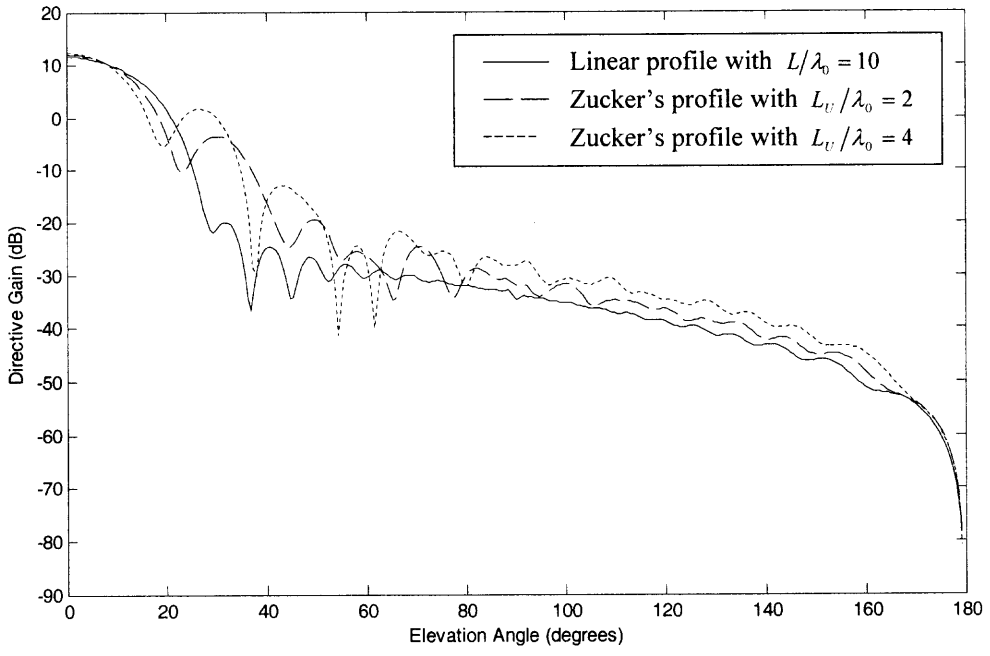

Figure B.30 Directive gain versus elevation angle (θ) of the antennas for $\varepsilon_r = 12$, $D_1/\lambda_0 = 0.0754$, $L/\lambda_0 = 10$ having linear profile and Zucker's profile with $L_F = L_T$ and $L_U/\lambda_0 = 2$ and 4, for linear case using $N_S = 120$, for Zucker case with $L_U/\lambda_0 = 2$ and 4 using $N_S = 107$ and 95 respectively, TM polarization.

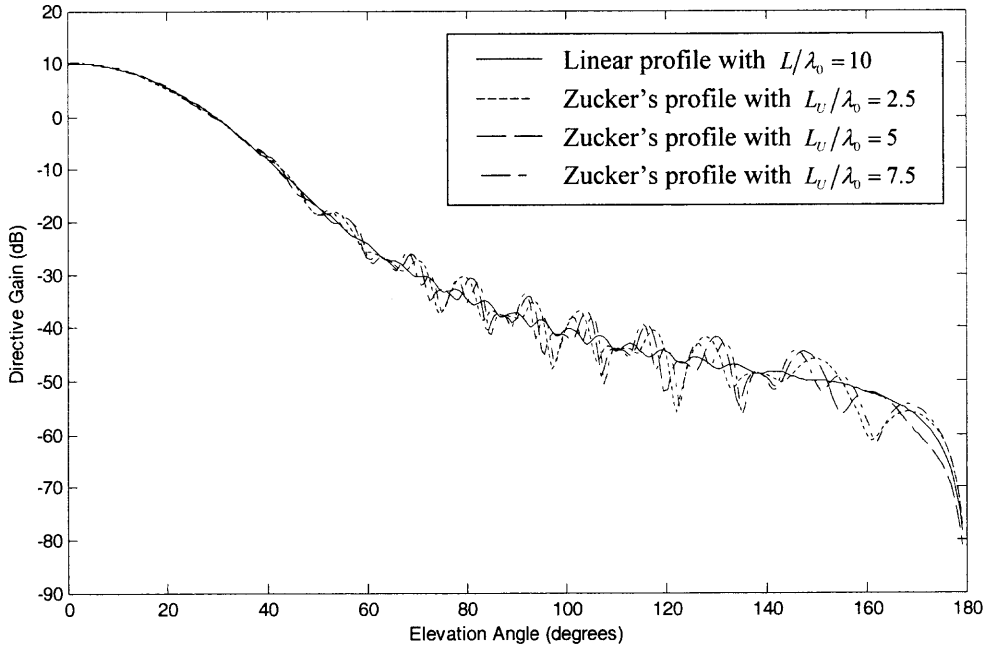

Figure B.31 Directive gain versus elevation angle (θ) of the antennas for $\varepsilon_r = 2.56$, $D_1/\lambda_0 = 0.2$ having linear profile and Zucker's profile with $L_F/\lambda_0 = L_T/\lambda_0 = 5$ and $L_U/\lambda_0 = 2.5$, 5 and 7.5, for linear case using $N_S = 120$, for Zucker case using $N_S = 119$, TE polarization.

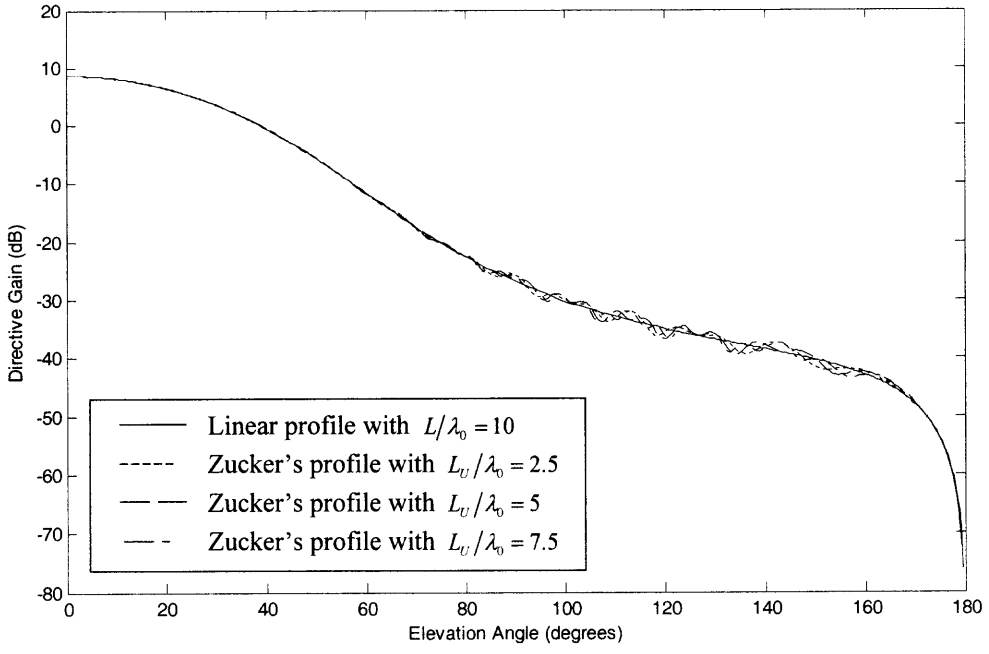

Figure B.32 Directive gain versus elevation angle (θ) of the antennas for $\varepsilon_r = 12$, $D_1/\lambda_0 = 0.0754$ having linear profile and Zucker's profile with $L_F/\lambda_0 = L_T/\lambda_0 = 5$ and $L_U/\lambda_0 = 2.5$, 5 and 7.5, for linear case using $N_S = 120$, for Zucker case using $N_S = 119$, TE polarization.

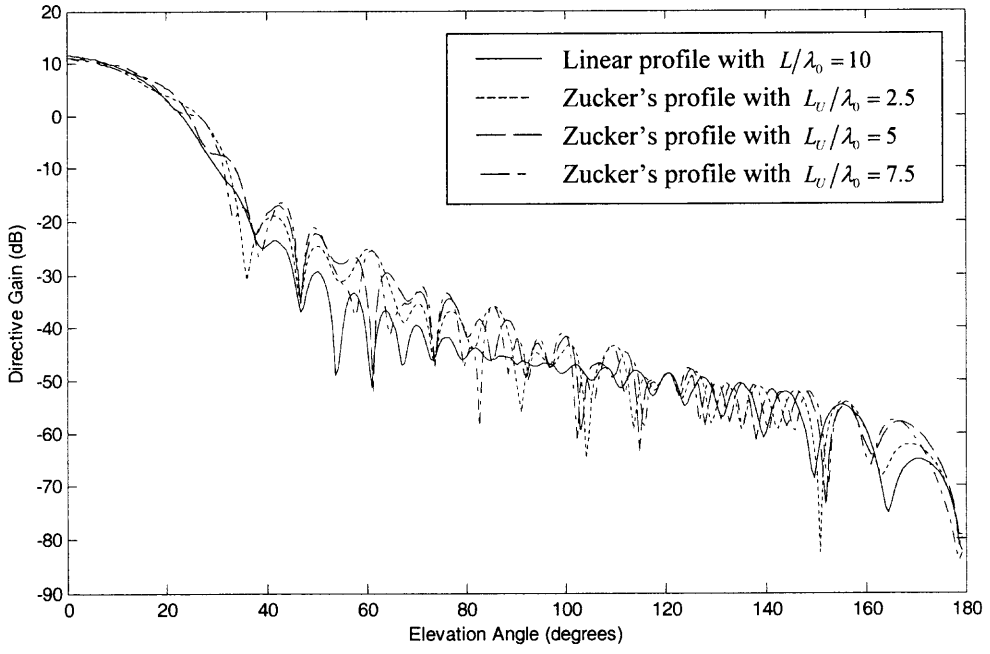

Figure B.33 Directive gain versus elevation angle (θ) of the antennas for $\varepsilon_r = 2.56$, $D_1/\lambda_0 = 0.2$ having linear profile and Zucker's profile with $L_F/\lambda_0 = L_T/\lambda_0 = 5$ and $L_U/\lambda_0 = 2.5$, 5 and 7.5, for linear case using $N_S = 120$, for Zucker case using $N_S = 119$, TM polarization.

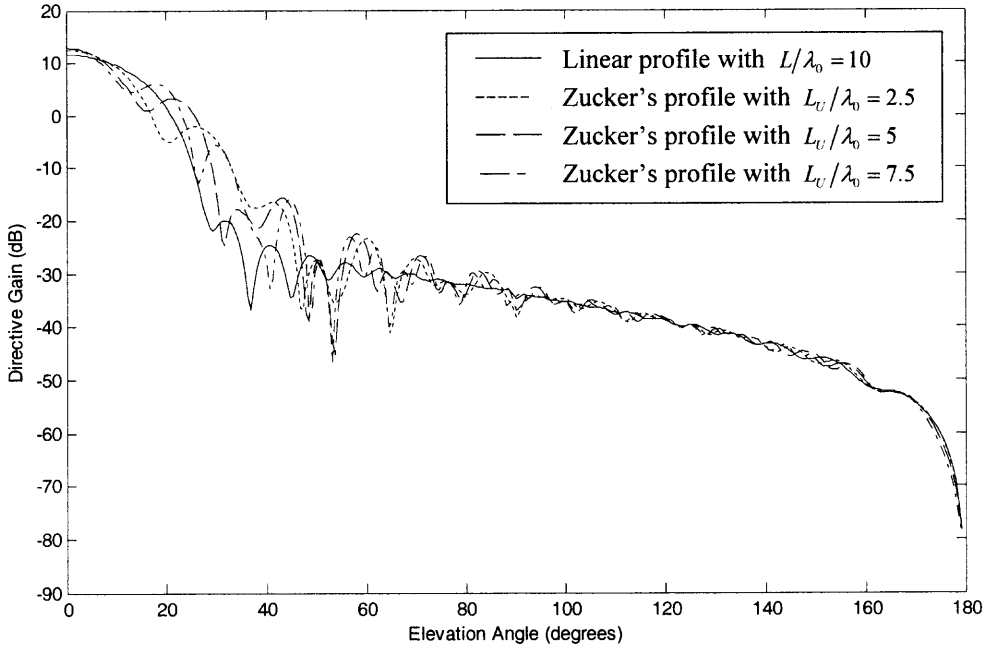

Figure B.34 Directive gain versus elevation angle (θ) of the antennas for $\varepsilon_r = 12$, $D_1/\lambda_0 = 0.0754$ having linear profile and Zucker's profile with $L_F/\lambda_0 = L_T/\lambda_0 = 5$ and $L_U/\lambda_0 = 2.5$, 5 and 7.5, for linear case using $N_S = 120$, for Zucker case using $N_S = 119$, TM polarization.

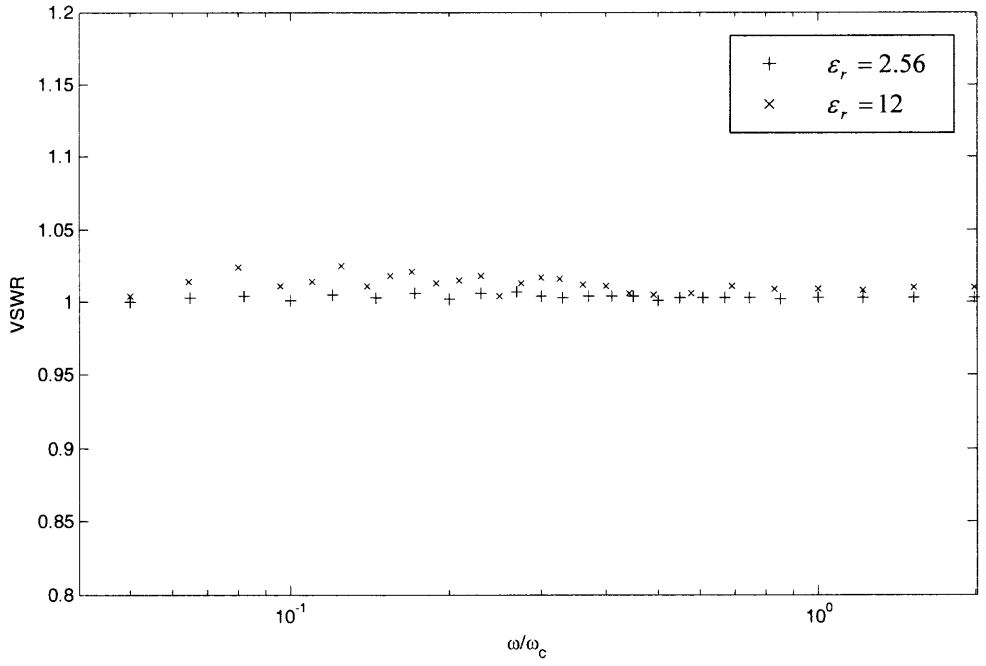

(a) VSWR

Figure B.35 Frequency characteristics of the slab waveguide/wedge antenna for $L = 10\lambda_c$ and $D_1 = 0.25\lambda_c(\varepsilon_r - 1)^{-\frac{1}{2}}$, TE polarization.

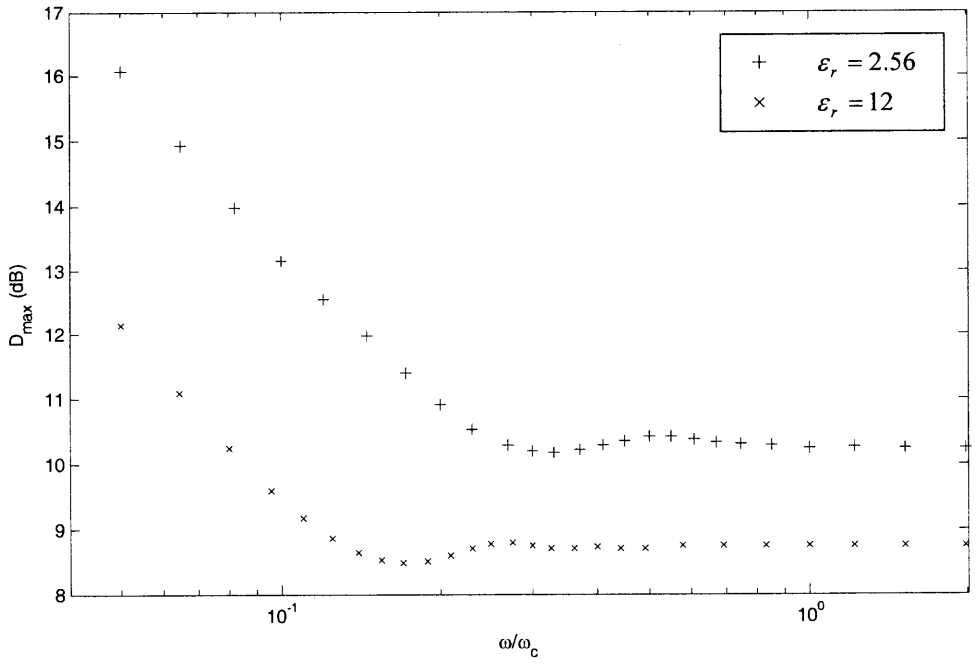

(b) Directivity ($D_{\max}$)

Figure B.35 (Continued) Frequency characteristics of the slab waveguide/wedge antenna for $L = 10\lambda_c$ and $D_1 = 0.25\lambda_c(\varepsilon_r - 1)^{-\frac{1}{2}}$, TE polarization.

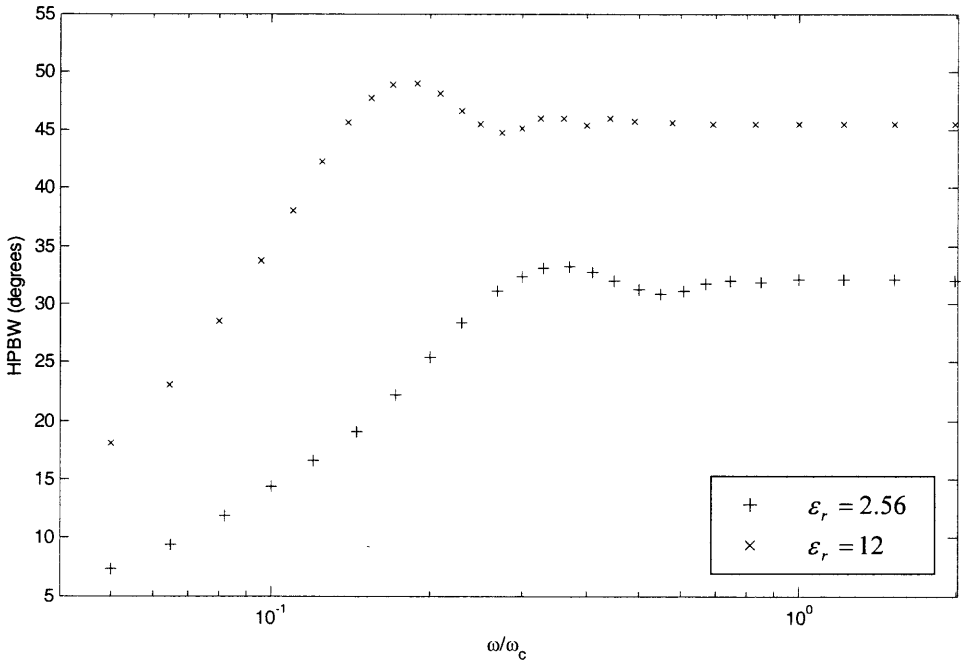

(c) Half-Power Beamwidth (HPBW)

Figure B.35 (Continued) Frequency characteristics of the slab waveguide/wedge antenna for $L = 10\lambda_c$ and $D_1 = 0.25\lambda_c(\varepsilon_r - 1)^{-\frac{1}{2}}$, TE polarization.

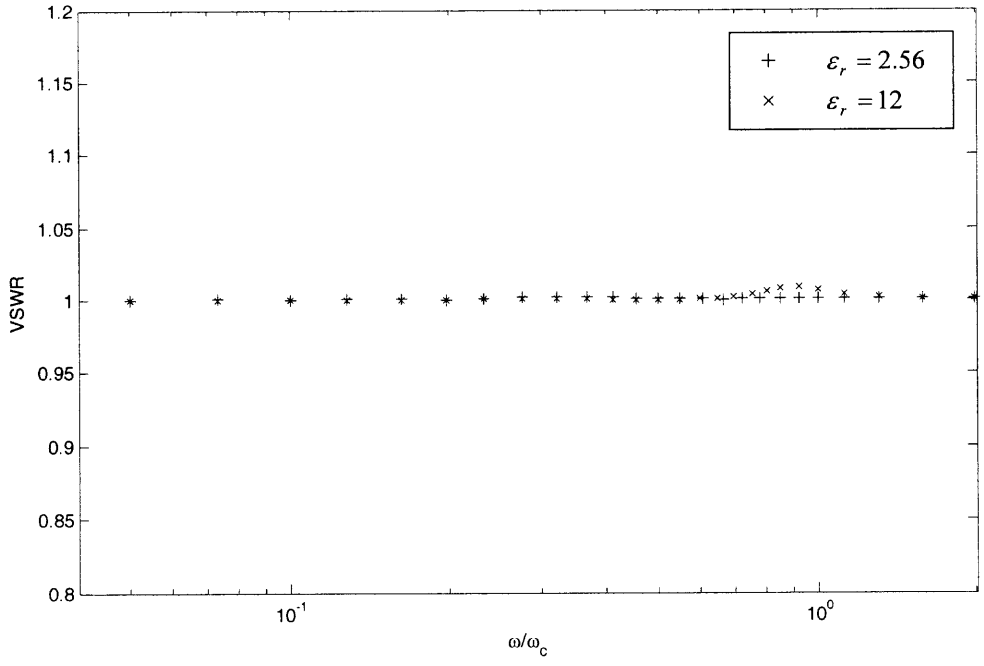

(a) VSWR

Figure B.36 Frequency characteristics of the slab waveguide/wedge antenna for $L = 10\lambda_c$ and $D_1 = 0.25\lambda_c(\varepsilon_r - 1)^{-\frac{1}{2}}$, TM polarization.

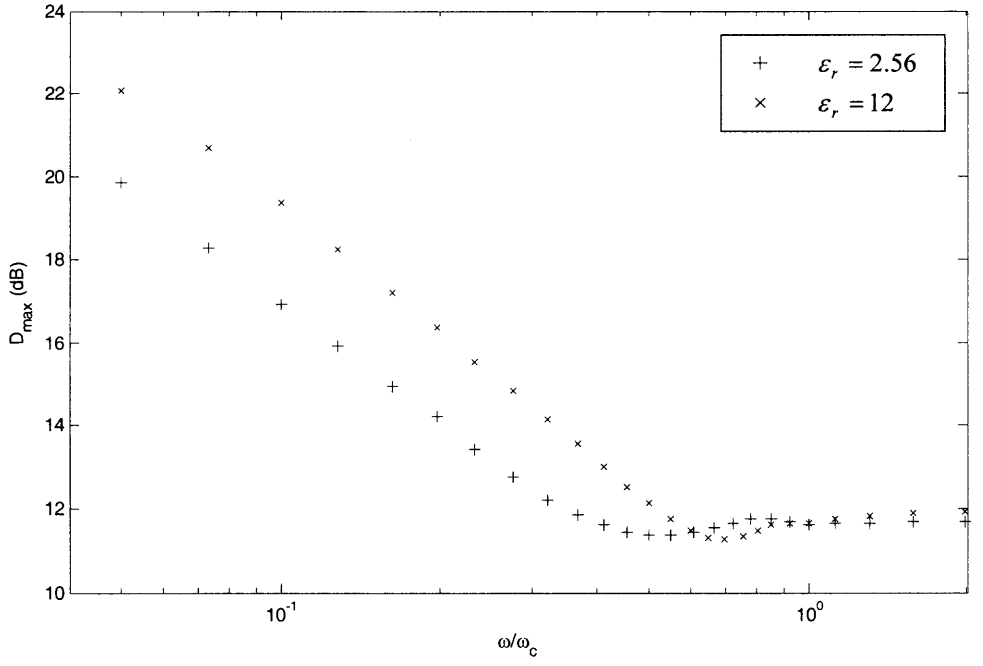

(b) Directivity ($D_{\max}$)

Figure B.36 (Continued) Frequency characteristics of the slab waveguide/wedge antenna for $L = 10\lambda_c$ and $D_1 = 0.25\lambda_c(\varepsilon_r - 1)^{-\frac{1}{2}}$, TM polarization.

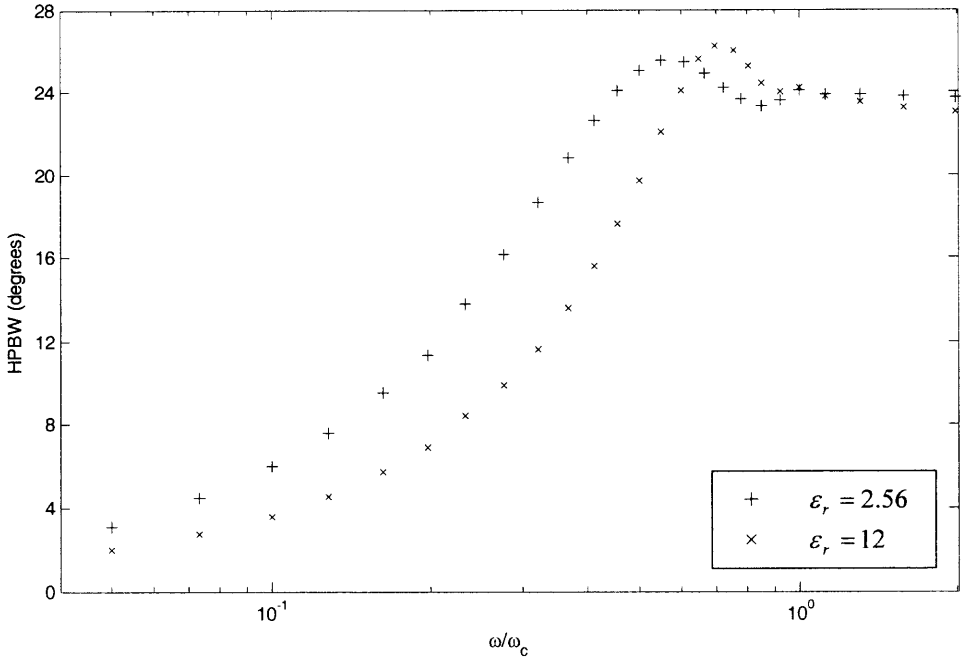

(c) Half-Power Beamwidth (HPBW)

Figure B.36 (Continued) Frequency characteristics of the slab waveguide/wedge antenna for $L = 10\lambda_c$ and $D_1 = 0.25\lambda_c(\varepsilon_r - 1)^{-\frac{1}{2}}$, TM polarization.

APPENDIX C

OVERLAP INTEGRALS FOR TE POLARIZATION

For TE polarization, an overlap integral has as its integrand the product of two mode functions from each of the adjacent waveguides separated by a step transition plane. Four overlap integrals are evaluated in closed form as follows.

C.1 Guided Modes on Both Sides of a Step Transition Plane

The overlap integral for guided modes from region i and region $i+1$, $D_i > D_{i+1}$, takes the form

$$Q_{0,0}(D_i, D_{i+1}) = \int_{x=0}^{\infty} \Phi_{i,0}(x)\Phi_{i+1,0}(x)dx = C_{i,0}C_{i+1,0}[J_1 + J_2 + J_3] \tag{C.1a}$$

where

$$J_1 = \int_{x=0}^{D_{i+1}} \cos(k_{x,i,0}x)\cos(k_{x,i+1,0}x)dx \tag{C.1b}$$

$$= \frac{1}{2}\left\{\frac{\sin[(k_{x,i,0} - k_{x,i+1,0})D_{i+1}]}{k_{x,i,0} - k_{x,i+1,0}} + \frac{\sin[(k_{x,i,0} + k_{x,i+1,0})D_{i+1}]}{k_{x,i,0} + k_{x,i+1,0}}\right\} \tag{C.1c}$$

$$J_2 = \int_{x=D_{i+1}}^{D_i} \cos(k_{x,i,0}x)\cos(k_{x,i+1,0}D_{i+1})e^{-\alpha_{x,i+1,0}(x-D_{i+1})}dx \tag{C.1d}$$

$$= \frac{\cos(k_{x,i+1,0}D_{i+1})}{\alpha_{x,i+1,0}^2 + k_{x,i,0}^2}\left\{e^{-\alpha_{x,i+1,0}(D_i - D_{i+1})}[-\alpha_{x,i+1,0}\cos(k_{x,i,0}D_i) + k_{x,i,0}\sin(k_{x,i,0}D_i)]\right.$$

$$\left. - [-\alpha_{x,i+1,0}\cos(k_{x,i,0}D_{i+1}) + k_{x,i,0}\sin(k_{x,i,0}D_{i+1})]\right\} \tag{C.1e}$$

$$J_3 = \int_{x=D_i}^{\infty} \cos(k_{x,i,0} D_i) e^{-\alpha_{x,i,0}(x-D_i)} \cos(k_{x,i+1,0} D_{i+1}) e^{-\alpha_{x,i+1,0}(x-D_{i+1})} dx \tag{C.1f}$$

$$= \frac{1}{\alpha_{x,i,0} + \alpha_{x,i+1,0}} \cos(k_{x,i,0} D_i) \cos(k_{x,i+1,0} D_{i+1}) e^{-\alpha_{x,i+1,0}(D_i - D_{i+1})} \tag{C.1g}$$

C.2 Guided Mode from Region *i* and Radiation Mode from Region *i* + 1

The overlap integral for guided mode from region i and radiation mode from region $i+1$, $D_i > D_{i+1}$, is expressed as

$$Q_0(u; D_i, D_{i+1}) = \int_{x=0}^{\infty} \Phi_{i,0}(x) \Phi_{i+1}(x,u) dx = C_{i,0} C_{i+1}(u)[J_4 + J_5 + J_6] \tag{C.2a}$$

where

$$J_4 = \int_{x=0}^{D_{i+1}} \cos(k_{x,i,0} x) \cos(vx) dx \tag{C.2b}$$

$$= \frac{1}{2}\left\{ \frac{\sin[(k_{x,i,0} - v) D_{i+1}]}{k_{x,i,0} - v} + \frac{\sin[(k_{x,i,0} + v) D_{i+1}]}{k_{x,i,0} + v} \right\} \tag{C.2c}$$

$$J_5 = \int_{x=D_{i+1}}^{D_i} \cos(k_{x,i,0} x) \left\{ \cos(vD_{i+1}) \cos[u(x - D_{i+1})] - \frac{v}{u} \sin(vD_{i+1}) \sin[u(x - D_{i+1})] \right\} dx \tag{C.2d}$$

$$= \frac{1}{2}[\cos(vD_{i+1}) \cos(uD_{i+1}) + \frac{v}{u} \sin(vD_{i+1}) \sin(uD_{i+1})]$$

$$\times \left\{ \frac{\sin[(k_{x,i,0} - u) D_i] - \sin[(k_{x,i,0} - u) D_{i+1}]}{k_{x,i,0} - u} + \frac{\sin[(k_{x,i,0} + u) D_i] - \sin[(k_{x,i,0} + u) D_{i+1}]}{k_{x,i,0} + u} \right\}$$

$$+ \frac{1}{2}[\cos(vD_{i+1}) \sin(uD_{i+1}) - \frac{v}{u} \sin(vD_{i+1}) \cos(uD_{i+1})]$$

$$\times \left\{ \frac{\cos[(k_{x,i,0} - u) D_i] - \cos[(k_{x,i,0} - u) D_{i+1}]}{k_{x,i,0} - u} - \frac{\cos[(k_{x,i,0} + u) D_i] - \cos[(k_{x,i,0} + u) D_{i+1}]}{k_{x,i,0} + u} \right\}$$

(C.2e)

$$J_6 = \int_{x=D_i}^{\infty} \cos(k_{x,i,0}D_i)e^{-\alpha_{x,i,0}(x-D_i)}\left\{\cos(vD_{i+1})\cos[u(x-D_{i+1})]\right.$$

$$\left. -\frac{v}{u}\sin(vD_{i+1})\sin[u(x-D_{i+1})]\right\}dx \quad \text{(C.2f)}$$

$$= -\frac{\cos(k_{x,i,0}D_i)}{\alpha_{x,i,0}^2+u^2}\left[\cos(vD_{i+1})\{-\alpha_{x,i,0}\cos[u(D_i-D_{i+1})]+u\sin[u(D_i-D_{i+1})]\}\right.$$

$$\left. +\frac{v}{u}\sin(vD_{i+1})\{\alpha_{x,i,0}\sin[u(D_i-D_{i+1})]+u\cos[u(D_i-D_{i+1})]\}\right] \quad \text{(C.2g)}$$

C.3 Radiation Mode from Region *i* and Guided Mode from Region *i* + 1

The overlap integral for radiation mode from region i and guided mode from region $i+1$, $D_i > D_{i+1}$, is given by

$$Q_0'(u;D_i,D_{i+1}) = \int_{x=0}^{\infty}\Phi_i(x,u)\Phi_{i+1,0}(x)dx = C_i(u)C_{i+1,0}[J_7+J_8+J_9] \quad \text{(C.3a)}$$

where

$$J_7 = \int_{x=0}^{D_{i+1}}\cos(vx)\cos(k_{x,i+1,0}x)dx \quad \text{(C.3b)}$$

$$= \frac{1}{2}\left\{\frac{\sin[(v-k_{x,i+1,0})D_{i+1}]}{v-k_{x,i+1,0}}+\frac{\sin[(v+k_{x,i+1,0})D_{i+1}]}{v+k_{x,i+1,0}}\right\} \quad \text{(C.3c)}$$

$$J_8 = \int_{x=D_{i+1}}^{D_i}\cos(vx)\cos(k_{x,i+1,0}D_{i+1})e^{-\alpha_{x,i+1,0}(x-D_{i+1})}dx \quad \text{(C.3d)}$$

$$= \frac{\cos(k_{x,i+1,0}D_{i+1})}{\alpha_{x,i+1,0}^2+v^2}\left\{e^{-\alpha_{x,i+1,0}(D_i-D_{i+1})}[-\alpha_{x,i+1,0}\cos(vD_i)+v\sin(vD_i)]\right.$$

$$\left. -[-\alpha_{x,i+1,0}\cos(vD_{i+1})+v\sin(vD_{i+1})]\right\} \quad \text{(C.3e)}$$

$$J_9 = \int_{x=D_i}^{\infty} \left\{ \cos(vD_i)\cos[u(x-D_i)] - \frac{v}{u}\sin(vD_i)\sin[u(x-D_i)] \right\}$$

$$\times \cos(k_{x,i+1,0}D_{i+1}) e^{-\alpha_{x,i+1,0}(x-D_{i+1})} dx \tag{C.3f}$$

$$= \frac{\cos(k_{x,i+1,0}D_{i+1})}{\alpha_{x,i+1,0}^2 + u^2} [\alpha_{x,i+1,0}\cos(vD_i) - v\sin(vD_i)] e^{-\alpha_{x,i+1,0}(D_i - D_{i+1})} \tag{C.3g}$$

C.4 Radiation Modes from Both Sides of a Step Transition Plane

The overlap integral for radiation modes from region i and region $i+1$, $D_i > D_{i+1}$, is written as

$$Q(u',u;D_i,D_{i+1}) = \int_{x=0}^{\infty} \Phi_i(x,u')\Phi_{i+1}(x,u)dx \tag{C.4a}$$

$$= Q_1(u';D_1,D_2)\delta(u-u') + \frac{Q_2(u',u;D_1,D_2)}{u'^2 - u^2} + Q_3(u',u;D_1,D_2) \tag{C.4b}$$

where

$$Q_1(u';D_i,D_{i+1}) = \frac{\pi}{2} C_i(u')C_{i+1}(u')$$

$$\times \left\{ \cos[u'(D_i - D_{i+1})][\cos(v'D_i)\cos(v'D_{i+1}) + (\frac{v'}{u'})^2 \sin(v'D_i)\sin(v'D_{i+1})] \right.$$

$$\left. + \frac{v'}{u'}\sin[u'(D_i - D_{i+1})]\sin[v'(D_i - D_{i+1})] \right\} \tag{C.4c}$$

$$Q_2(u',u;D_i,D_{i+1}) = C_i(u')C_{i+1}(u)$$

$$\times \left\{ \sin[u(D_i - D_{i+1})][u\cos(v'D_i)\cos(vD_{i+1}) + \frac{v'v}{u}\sin(v'D_i)\sin(vD_{i+1})] \right.$$

$$\left. + \cos[u(D_i - D_{i+1})][v\cos(v'D_i)\sin(vD_{i+1}) - v'\sin(v'D_i)\cos(vD_{i+1})] \right\} \tag{C.4d}$$

$$Q_3(u',u;D_i,D_{i+1}) = \frac{C_i(u')C_{i+1}(u)}{2}\left\{\frac{\sin[(v'-v)D_{i+1}]}{v'-v} + \frac{\sin[(v'+v)D_{i+1}]}{v'+v}\right.$$

$$+[\cos(vD_{i+1})\cos(uD_{i+1}) + \frac{v}{u}\sin(vD_{i+1})\sin(uD_{i+1})]$$

$$\times\left[\frac{\sin[(v'-u)D_i] - \sin[(v'-u)D_{i+1}]}{v'-u} + \frac{\sin[(v'+u)D_i] - \sin[(v'+u)D_{i+1}]}{v'+u}\right]$$

$$+[\cos(vD_{i+1})\sin(uD_{i+1}) - \frac{v}{u}\sin(vD_{i+1})\cos(uD_{i+1})]$$

$$\left.\times\left[\frac{\cos[(v'-u)D_i) - \cos[(v'-u)D_{i+1}]}{v'-u} - \frac{\cos[(v'+u)D_i] - \cos[(v'+u)D_{i+1}]}{v'+u}\right]\right\} \quad \text{(C.4e)}$$

APPENDIX D

OVERLAP INTEGRALS FOR TM POLARIZATION

For TM polarization, an overlap integral has as its integrand the product of two mode functions as in the case of TE polarization, but also includes division by the inhomogeneous dielectric constant of either the medium to the left or to the right of the step transition plane. Four overlap integrals for TM polarization are evaluated in closed form as follows.

D.1 Guided Modes on Both Sides of a Step Transition Plane

The overlap integral for guided modes from region i and region $i+1$, $D_i > D_{i+1}$, takes the forms

$$M_{0,0}^{(i)}(D_i, D_{i+1}) = \int_{x=0}^{\infty} \frac{1}{\varepsilon_{r,i}(x)} \Psi_{i,0}(x)\Psi_{i+1,0}(x)dx = C_{i,0}C_{i+1,0}[\frac{L_1}{\varepsilon_r} + \frac{L_2}{\varepsilon_r} + L_3] \quad \text{(D.1a)}$$

$$M_{0,0}^{(i+1)}(D_i, D_{i+1}) = \int_{x=0}^{\infty} \frac{1}{\varepsilon_{r,i+1}(x)} \Psi_{i,0}(x)\Psi_{i+1,0}(x)dx = C_{i,0}C_{i+1,0}[\frac{L_1}{\varepsilon_r} + L_2 + L] \quad \text{(D.1b)}$$

where

$$L_1 = J_1,\ L_2 = J_2 \text{ and } L_3 = J_3 \quad \text{(D.1c)}$$

D.2 Guided Mode from Region *i* and Radiation Mode from Region *i* + 1

The overlap integral for guided mode from region i and radiation mode from region $i+1$, $D_i > D_{i+1}$, takes the forms

$$M_0^{(i)}(u; D_i, D_{i+1}) = \int_{x=0}^{\infty} \frac{1}{\varepsilon_{r,i}(x)} \Psi_{i,0}(x)\Psi_{i+1}(x,u)dx = C_{i,0}C_{i+1}(u)[\frac{L_4}{\varepsilon_r} + \frac{L_5}{\varepsilon_r} + L_6] \quad \text{(D.2a)}$$

$$M_0^{(i+1)}(u; D_i, D_{i+1}) = \int_{x=0}^{\infty} \frac{1}{\varepsilon_{r,i+1}(x)} \Psi_{i,0}(x)\Psi_{i+1}(x,u)dx = C_{i,0}C_{i+1}(u)[\frac{L_4}{\varepsilon_r} + L_5 + L_6] \quad \text{(D.2b)}$$

where

$$L_4 = J_4 \quad \text{(D.2c)}$$

$$L_5 = \int_{x=D_{i+1}}^{D_i} \cos(k_{x,i,0}x)\left\{\cos(vD_{i+1})\cos[u(x-D_{i+1})] - \frac{v}{\varepsilon_r u}\sin(vD_{i+1})\sin[u(x-D_{i+1})]\right\}dx \quad \text{(D.2d)}$$

$$= \frac{1}{2}[\cos(vD_{i+1})\cos(uD_{i+1}) + \frac{v}{\varepsilon_r u}\sin(vD_{i+1})\sin(uD_{i+1})]$$

$$\times\left\{\frac{\sin[(k_{x,i,0}-u)D_i] - \sin[(k_{x,i,0}-u)D_{i+1}]}{k_{x,i,0}-u} + \frac{\sin[(k_{x,i,0}+u)D_i] - \sin[(k_{x,i,0}+u)D_{i+1}]}{k_{x,i,0}+u}\right\}$$

$$+ \frac{1}{2}[\cos(vD_{i+1})\sin(uD_{i+1}) - \frac{v}{\varepsilon_r u}\sin(vD_{i+1})\cos(uD_{i+1})]$$

$$\times\left\{\frac{\cos[(k_{x,i,0}-u)D_i] - \cos[(k_{x,i,0}-u)D_{i+1}]}{k_{x,i,0}-u} - \frac{\cos[(k_{x,i,0}+u)D_i] - \cos[(k_{x,i,0}+u)D_{i+1}]}{k_{x,i,0}+u}\right\}$$

(D.2e)

$$L_6 = \int_{x=D_i}^{\infty} \cos(k_{x,i,0}D_i)e^{-\alpha_{x,i,0}(x-D_i)}\left\{\cos(vD_{i+1})\cos[u(x-D_{i+1})]\right.$$

$$\left. -\frac{v}{\varepsilon_r u}\sin(vD_{i+1})\sin[u(x-D_{i+1})]\right\}dx \quad \text{(D.2f)}$$

$$= -\frac{\cos(k_{x,i,0}D_i)}{\alpha_{x,i,0}^2+u^2}\left[\cos(vD_{i+1})\{-\alpha_{x,i,0}\cos[u(D_i-D_{i+1})]+u\sin[u(D_i-D_{i+1})]\}\right.$$

$$\left. +\frac{v}{\varepsilon_r u}\sin(vD_{i+1})\{\alpha_{x,i,0}\sin[u(D_i-D_{i+1})]+u\cos[u(D_i-D_{i+1})]\}\right] \quad \text{(D.2g)}$$

D.3 Radiation Mode from Region *i* and Guided Mode from Region *i* + 1

The overlap integral for radiation mode from region i and guided mode from region $i+1$, $D_i > D_{i+1}$, is given by

$$M_0'^{(i)}(u;D_i,D_{i+1}) = \int_{x=0}^{\infty}\frac{1}{\varepsilon_{r,i}(x)}\Psi_i(x,u)\Psi_{i+1,0}(x)dx = C_i(u)C_{i+1,0}[\frac{L_7}{\varepsilon_r}+\frac{L_8}{\varepsilon_r}+L_9] \quad \text{(D.3a)}$$

$$M_0'^{(i+1)}(u;D_i,D_{i+1}) = \int_{x=0}^{\infty}\frac{1}{\varepsilon_{r,i+1}(x)}\Psi_i(x,u)\Psi_{i+1,0}(x)dx = C_i(u)C_{i+1,0}[\frac{L_7}{\varepsilon_r}+L_8+L_9] \quad \text{(D.3b)}$$

where

$$L_7 = J_7,\ L_8 = J_8 \quad \text{(D.3c)}$$

$$L_9 = \int_{x=D_i}^{\infty}\left\{\cos(vD_i)\cos[u(x-D_i)]-\frac{v}{\varepsilon_r u}\sin(vD_i)\sin[u(x-D_i)]\right\}$$

$$\times\cos(k_{x,i+1,0}D_{i+1})e^{-\alpha_{x,i+1,0}(x-D_{i+1})}dx \quad \text{(D.3d)}$$

$$= \frac{\cos(k_{x,i+1,0}D_{i+1})}{\alpha_{x,i+1,0}^2+u^2}[\alpha_{x,i+1,0}\cos(vD_i)-\frac{v}{\varepsilon_r}\sin(vD_i)]e^{-\alpha_{x,i+1,0}(D_i-D_{i+1})} \quad \text{(D.3e)}$$

D.4 Radiation Modes from Both Sides of a Step Transition Plane

The overlap integral for radiation modes from region i and region $i+1$, $D_i > D_{i+1}$, is given by

$$M^{(i)}(u',u;D_i,D_{i+1}) = \int_{x=0}^{\infty} \frac{1}{\varepsilon_{r,i}(x)} \Psi_i(x,u')\Psi_{i+1}(x,u)dx$$

$$= M_1(u';D_i,D_{i+1})\delta(u-u') + \frac{M_2(u',u;D_i,D_{i+1})}{u'^2-u^2} + M_3^{(i)}(u',u;D_i,D_{i+1}) \qquad \text{(D.4b)}$$

$$M^{(i+1)}(u',u;D_i,D_{i+1}) = \int_{x=0}^{\infty} \frac{1}{\varepsilon_{r,i+1}(x)} \Psi_i(x,u')\Psi_{i+1}(x,u)dx$$

$$= M_1(u';D_i,D_{i+1})\delta(u-u') + \frac{M_2(u',u;D_i,D_{i+1})}{u'^2-u^2} + M_3^{(i+1)}(u',u;D_i,D_{i+1}) \qquad \text{(D.4d)}$$

where

$$M_1(u';D_i,D_{i+1}) = \frac{\pi}{2} C_i(u')C_{i+1}(u')$$

$$\times \left\{ \cos[u'(D_i-D_{i+1})][\cos(v'D_i)\cos(v'D_{i+1}) + (\frac{v'}{\varepsilon_r u'})^2 \sin(v'D_i)\sin(v'D_{i+1})] \right.$$

$$\left. + \frac{v'}{\varepsilon_r u'} \sin[u'(D_i-D_{i+1})]\sin[v'(D_i-D_{i+1})] \right\} \qquad \text{(D.4e)}$$

$$M_2(u',u;D_i,D_{i+1}) = C_i(u')C_{i+1}(u)$$

$$\times \left\{ \sin[u(D_i-D_{i+1})][u\cos(v'D_i)\cos(vD_{i+1}) + \frac{v'v}{\varepsilon_r^2 u} \sin(v'D_i)\sin(vD_{i+1})] \right.$$

$$\left. + \cos[u(D_i-D_{i+1})][\frac{v}{\varepsilon_r}\cos(v'D_i)\sin(vD_{i+1}) - \frac{v'}{\varepsilon_r}\sin(v'D_i)\cos(vD_{i+1})] \right\} \qquad \text{(D.4f)}$$

$$M_3^{(i)}(u',u;D_i,D_{i+1}) = \frac{C_i(u')C_{i+1}(u)}{2}\left\{\frac{\sin[(v'-v)D_{i+1}]}{\varepsilon_r(v'-v)} + \frac{\sin[(v'+v)D_{i+1}]}{\varepsilon_r(v'+v)}\right.$$

$$+\frac{1}{\varepsilon_r}[\cos(vD_{i+1})\cos(uD_{i+1}) + \frac{v}{\varepsilon_r u}\sin(vD_{i+1})\sin(uD_{i+1})]$$

$$\times\left[\frac{\sin[(v'-u)D_i]-\sin[(v'-u)D_{i+1}]}{v'-u} + \frac{\sin[(v'+u)D_i]-\sin[(v'+u)D_{i+1}]}{v'+u}\right]$$

$$+\frac{1}{\varepsilon_r}[\cos(vD_{i+1})\sin(uD_{i+1}) - \frac{v}{\varepsilon_r u}\sin(vD_{i+1})\cos(uD_{i+1})]$$

$$\left.\times\left[\frac{\cos[(v'-u)D_i]-\cos[(v'-u)D_{i+1}]}{v'-u} - \frac{\cos[(v'+u)D_i]-\cos[(v'+u)D_{i+1}]}{v'+u}\right]\right\} \quad \text{(D.4g)}$$

$$M_3^{(i+1)}(u',u;D_i,D_{i+1}) = \frac{C_i(u')C_{i+1}(u)}{2}\left\{\frac{\sin[(v'-v)D_{i+1}]}{\varepsilon_r(v'-v)} + \frac{\sin[(v'+v)D_{i+1}]}{\varepsilon_r(v'+v)}\right.$$

$$+[\cos(vD_{i+1})\cos(uD_{i+1}) + \frac{v}{\varepsilon_r u}\sin(vD_{i+1})\sin(uD_{i+1})]$$

$$\times\left[\frac{\sin[(v'-u)D_i]-\sin[(v'-u)D_{i+1}]}{v'-u} + \frac{\sin[(v'+u)D_i]-\sin[(v'+u)D_{i+1}]}{v'+u}\right]$$

$$+[\cos(vD_{i+1})\sin(uD_{i+1}) - \frac{v}{\varepsilon_r u}\sin(vD_{i+1})\cos(uD_{i+1})]$$

$$\left.\times\left[\frac{\cos[(v'-u)D_i]-\cos[(v'-u)D_{i+1}]}{v'-u} - \frac{\cos[(v'+u)D_i]-\cos[(v'+u)D_{i+1}]}{v'+u}\right]\right\} \quad \text{(D.4h)}$$

APPENDIX E

SIMPSON'S ONE-THIRD RULE

Simpson's one-third rule is used to evaluate integrals over ranges of the transverse wavenumber u of the radiation modes away from singularities. The possible ranges of u fall within two parts given by $0 \le u < k_0$ and $k_0 < u \le u_{\max}$. The first part corresponds to the propagating radiation modes and the second one corresponds to the evanescent radiation modes.

To apply Simpson's rule over the u-range of the propagating modes, this range is subdivided into $N'/2$ intervals, each of which is of length $u_{2k} - u_{2k-2}$ as shown in Figure E.1, where k = 1, 2, 3,..., $N'/2$, $u_{N'} = k_0$ and N' is an even integer. Each interval has two segments[9] of equal width, given by h_k in (E.2). The total numbers of intervals (N_P^I) and segments (N_P) in the range of the propagating modes are $N_P^I = N'/2$ and $N_P = N' = 2N_P^I$, respectively.

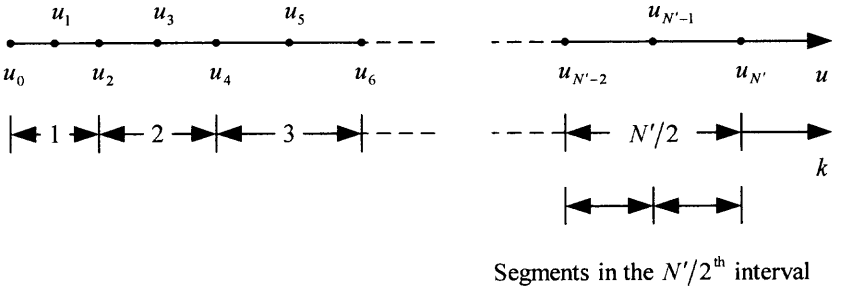

Figure E.1 Discretization of the u-range of the propagating radiation modes into $N'/2$ intervals of length $u_{2k} - u_{2k-2}$.

---

[9] In Simpson's one-third rule, one interval consists of two segments of equal width [54], [55].

The integration of $F(u)$ in (E.1) over the range $[0, k_0]$ can be approximated by the composite Simpson's one-third rule [54], [55]

$$\int_{u=0}^{k_0} F(u)du \cong \frac{1}{3}\sum_{k=1}^{N'/2}[F(u_{2k-2}) + 4F(u_{2k-1}) + F(u_{2k})]h_k \tag{E.1}$$

$$h_k = (u_{2k} - u_{2k-2})/2 \tag{E.2}$$

Similarly, the u-range of the evanescent modes is subdivided into $(N - N')/2$ intervals of length $u_{2k} - u_{2k-2}$ as shown in Figure E.2, where $k = N'/2+1,\ N'/2+2,\ N'/2+3,\ldots,\ N/2$, $u_N = u_{\max}$ with N an even integer. The total numbers of intervals (N_E^I) and segments (N_E) in this range are $N_E^I = (N - N')/2$ and $N_E = N - N'$, respectively.

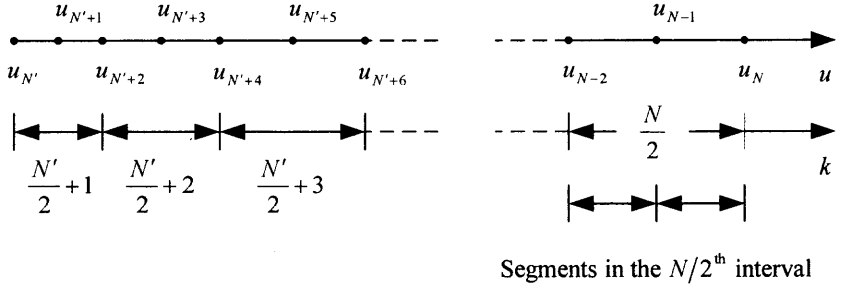

Figure E.2 Discretization of the u-range of evanescent radiation modes into $(N - N')/2$ intervals.

The integration of $F(u)$ over the range $[k_0, u_{\max}]$ is given by

$$\int_{u=k_0}^{u_{\max}} F(u)du \cong \frac{1}{3} \sum_{k=N'/2+1}^{N/2} [F(u_{2k-2}) + 4F(u_{2k-1}) + F(u_{2k})]h_k \tag{E.3}$$

The total numbers of intervals and segments in both ranges are $N_T^I = N/2$ and N, respectively.

APPENDIX F

THE FAR FIELD AND RADIATION INTENSITY

The integral representations for the field in region 1 and M described in Chapter 2 and 3 have in their respective integrands amplitude and phase functions such that the amplitude is slowly varying function while the phase is a rapidly varying function of the variable of integration. Hence, the method of stationary phase is used to find the asymptotic representation of field in far zone, which usually is the region of interest in antenna problems. For TE polarization, the total electric field has only a y-component whose asymptotic form is needed for calculating the radiation intensity. The asymptotic forms (valid in the far field region) of the electric field E_y, to the left of the base of antenna (in region 1) and to the right of the tip of the antenna (in region M), are obtained as follows.

F.1 Far Electric Field to the Left of the Base of the Antenna

The scattered electric field at an arbitrary point $P(x,z)$ in the far field free space region to the left of the base of the antenna, $\pi/2 \le \theta \le \pi$, is given by

$$E_{y,1} = \int_{u=0}^{k_0} \frac{k_0}{\beta(u)} R_b(u) e^{j\beta(u)z} \Phi_1(x,u) du \tag{F.1a}$$

where

$$R_b(u) = R_1^{f1}(u) + \sum_{p=1}^{N_b} T_1^{b,p}(u) \tag{F.1b}$$

Let

$$u = k_0 \sin w,\ \beta(u) = k_0 \cos w,\ z = \rho \cos\theta \tag{F.2a}$$

where

$$0 \le w \le \pi/2,\ \pi/2 \le \theta \le \pi \tag{F.2b}$$

Thus, (F.1) becomes

$$E_{y,1} = \int_{w=0}^{\pi/2} k_0 R_b(k_0 \sin w) e^{jk_0 \rho \cos w \cos\theta} C_1(k_0 \sin w)$$

$$\times \left\{ \cos(vD_1)\cos[u(x-D_1)] - \frac{v}{u}\sin(vD_1)\sin[u(x-D_1)] \right\} dw \tag{F.3a}$$

$$= \frac{k_0}{2} \int_{w=0}^{\pi/2} R_b(k_0 \sin w) C_1(k_0 \sin w) \left\{ [\cos(vD_1) + j\frac{v}{k_0}\frac{\sin(vD_1)}{\sin w}] e^{-jk_0 D_1 \sin w} e^{j\Omega q_1(w)} \right.$$

$$\left. + [\cos(vD_1) - j\frac{v}{k_0}\frac{\sin(vD_1)}{\sin w}] e^{jk_0 D_1 \sin w} e^{j\Omega q_2(w)} \right\} dw \tag{F.3b}$$

where

$$q_1(w) = \cos(\theta - w)\ ,\ q_2(w) = \cos(\theta + w) \text{ and } \Omega = k_0 \rho \tag{F.3c}$$

The parameter ρ in (F.2a) is the cylindrical coordinate radial distance from the origin. Functions $q_1(w)$ and $q_2(w)$ are real. The parameter Ω is large value because ρ extends to the far zone. The first derivative $q_1'(w) = dq_1(w)/dw = \sin(\theta - w)$. Since $0 \le w \le \pi/2$ and $\pi/2 \le \theta \le \pi$, there is no point w in the range $0 < w < \pi/2$ that allows $q_1'(w) = 0$. The exponential factor $e^{j\Omega q_1(w)}$ in the integrand oscillates very rapidly between the values of 1 and -1 for large values of Ω. The contribution to the integral of the highly oscillatory positive and negative values tends to cancel one another [22]. Thus, (F.3b) reduces to

$$E_{y,1} = \frac{k_0}{2} \int_{w=0}^{\pi/2} R_b(k_0 \sin w) C_1(k_0 \sin w) [\cos(vD_1) - j \frac{v}{k_0} \frac{\sin(vD_1)}{\sin w}]$$

$$\times e^{jk_0 D_1 \sin w} e^{j\Omega q_2(w)} dw \tag{F.4}$$

The point $w = w_s$ is found from $q_2'(w)\big|_{w=w_s} = -\sin(w+\theta)\big|_{w=w_s} = 0$, to yield $w_s = \pi - \theta$. The second derivative of $q_2(w)$ at $w = w_s$ equals $-\cos(w+\theta)\big|_{w=w_s} = 1$. The point w_s is located in the range $0 < w_s < \pi/2$ and has the properties that $q_2'(w_s) = 0$ and $q_2''(w_s) \neq 0$. Consequently, $q_2(w)$ and Ω are suitable for evaluation of the integral (F.4) by means of the method of stationary phase. By applying the method to (F.4), the asymptotic expression for the electric field in the far zone to the left of the base of the antenna is obtained as follows:

$$E_{y,1} \sim \sqrt{\frac{2\pi}{k_0 \rho}} \frac{k_0}{2} R_b(k_0 \sin w_s) C_1(k_0 \sin w_s) [\cos(v_s D_1) - j \frac{v_s}{k_0} \frac{\sin(v_s D_1)}{\sin w_s}]$$

$$\times e^{jk_0 D_1 \sin w_s} e^{j[k_0 \rho \cos(\theta + w_s) + \pi/4]} \tag{F.5a}$$

$$= k_0 R_b(k_0 \sin\theta) e^{j\zeta} \frac{e^{-j(k_0\rho - \pi/4)}}{\sqrt{k_0 \rho}} \tag{F.5b}$$

where

$$\zeta = k_0 D_1 \sin\theta - \tan^{-1}\left[\frac{\sqrt{\varepsilon_r - \cos^2\theta}}{\sin\theta} \tan(k_0 \sqrt{\varepsilon_r - \cos^2\theta} D_1)\right] \tag{F.5c}$$

$$v_s = k_0 \sqrt{\varepsilon_r - \cos^2 w_s} \tag{F.5d}$$

The radiation intensity $U_1(\theta)$ to the left of the base of the antenna (backward pattern) is calculated from the far zone electric field (F.5) by [24], [25]

$$U_1(\theta) = \frac{\rho}{2\eta_0}\left|E_{y,1}\right|^2 = \frac{1}{2\eta_0}\left|\sqrt{k_0}R_b(k_0\sin\theta)\right|^2 = \frac{1}{2\eta_0}\left|\overline{R}_b(\sin\theta)\right|^2, \quad \pi/2 \le \theta \le \pi \quad \text{(F.6)}$$

F.2 Far Electric Field to the Right of the Tip of the Antenna

The scattered electric field at an arbitrary point $P(x,z)$ in the far zone to the right of the tip of the antenna, $0 \le \theta \le \pi/2$, takes the form

$$E_{y,M} = \int_{u=0}^{k_0} \frac{k_0}{\beta(u)} T_f(u) e^{-j\beta(u)z} \Phi_M(x,u)\,du \quad \text{(F.7a)}$$

$$= \frac{k_0}{2}\int_{w=0}^{\pi/2} T_f(k_0\sin w) C_M(k_0\sin w)\left\{[\cos(vD_M) + j\frac{v}{k_0}\frac{\sin(vD_M)}{\sin w}]e^{-jk_0D_M\sin w}e^{j\Omega q_3(w)}\right.$$

$$\left. + [\cos(vD_M) - j\frac{v}{k_0}\frac{\sin(vD_M)}{\sin w}]e^{jk_0D_M\sin w}e^{j\Omega q_4(w)}\right\} dw \quad \text{(F.7b)}$$

where

$$T_f(u) = \sum_{p=1}^{N_f} T_{M-1}^{f,p}(u) \quad \text{(F.7c)}$$

$$q_3(w) = \cos(\theta - w)\ ,\ q_4(w) = \cos(\theta + w) \quad \text{(F.7d)}$$

$$u = k_0\sin w,\ \beta(u) = k_0\cos w,\ z = \rho\cos\theta,\ 0 \le w \le \pi/2 \quad \text{(F.7e)}$$

The function $q_4(w)$ has no stationary points in the range $0 < w < \pi/2$. Thus, (F.7b) reduces to

$$E_{y,M} = \frac{k_0}{2}\int_{w=0}^{\pi/2} T_f(k_0 \sin w) C_M(k_0 \sin w)[\cos(vD_M) - j\frac{v}{k_0}\frac{\sin(vD_M)}{\sin w}]$$

$$\times e^{-jk_0 D_M \sin w} e^{j\Omega q_3(w)} dw \tag{F.8}$$

The point $w = w_s$, defined to satisfy $q_3'(w) = 0$, is given by $w_s = \theta$. $q_3''(w)\big|_{w=w_s} = -1$. Thus, the point w_s is located in $0 < w_s < \pi/2$ and has the properties that $q_3'(w_s) = 0$ and $q_3''(w_s) \neq 0$. By applying the method of stationary phase to (F.8), the asymptotic electric field in the far zone to the right of the tip of antenna is obtained as follows:

$$E_{y,M} \sim \sqrt{\frac{2\pi}{k_0\rho}}\frac{k_0}{2} T_f(k_0 \sin w_s) C_M(k_0 \sin w_s)[\cos(v_s D_M) + j\frac{v_s}{k_0}\frac{\sin(v_s D_M)}{\sin w_s}]$$

$$\times e^{-jk_0 D_M \sin w_s} e^{j[k_0\rho\cos(\theta - w_s) - \pi/4]} \tag{F.9a}$$

$$= k_0 T_f(k_0 \sin\theta) e^{-j\zeta} \frac{e^{j(k_0\rho - \pi/4)}}{\sqrt{k_0\rho}} \tag{F.9b}$$

where

$$\zeta = k_0 D_M \sin\theta - \tan^{-1}\left[\frac{\sqrt{\varepsilon_r - \cos^2\theta}}{\sin\theta}\tan(k_0\sqrt{\varepsilon_r - \cos^2\theta} D_M)\right] \tag{F.9c}$$

$$v_s = k_0\sqrt{\varepsilon_r - \cos^2 w_s} \tag{F.9d}$$

The associated radiation intensity to the right of the tip of the antenna (forward pattern) is thus given by

$$U_M(\theta) = \frac{\rho}{2\eta_0}\left|E_{y,M}\right|^2 = \frac{1}{2\eta_0}\left|\sqrt{k_0} T_f(k_0 \sin\theta)\right|^2 = \frac{1}{2\eta_0}\left|\overline{T}_f(\sin\theta)\right|^2, \quad 0 \le \theta \le \pi/2 \tag{F.10}$$

F.3 Far Magnetic Field for TM Polarization

For TM polarization, the y-component of magnetic field is used for calculating the radiation intensity. The asymptotic representation of H_y is obtained by considering the scatted fields to the left of the base of antenna and to the right of the tip of the antenna. By following the same procedure as that for TE polarization, the asymptotic representation of H_y is obtained as follows:

$$H_y \sim \begin{cases} k_0 T_f (k_0 \sin\theta) e^{-j\zeta_f} \dfrac{e^{j(k_0\rho-\pi/4)}}{\sqrt{k_0\rho}}, & 0 \le \theta \le \dfrac{\pi}{2} \\ -k_0 T_b (k_0 \sin\theta) e^{j\zeta_b} \dfrac{e^{-j(k_0\rho-\pi/4)}}{\sqrt{k_0\rho}}, & \dfrac{\pi}{2} \le \theta \le \pi \end{cases} \tag{F.11a}$$

where

$$\zeta_f = k_0 D_M \sin\theta - \tan^{-1}\left[\frac{\sqrt{\varepsilon_r - \cos^2\theta}}{\varepsilon_r \sin\theta} \tan(k_0 \sqrt{\varepsilon_r - \cos^2\theta} D_M)\right] \tag{F.11b}$$

$$\zeta_b = k_0 D_1 \sin\theta - \tan^{-1}\left[\frac{\sqrt{\varepsilon_r - \cos^2\theta}}{\varepsilon_r \sin\theta} \tan(k_0 \sqrt{\varepsilon_r - \cos^2\theta} D_1)\right] \tag{F.11c}$$

REFERENCES

1. H. Jacobs and M. M. Chrepta, "Electronic Phase Shifter for Millimeter-Wave Semiconductor Dielectric Integrated Circuits," *IEEE Trans. Microwave Theory Tech.*, vol. 22, no. 4, pp. 411-417, Apr. 1974.

2. B. J. Levin and J. E. Kietzer, "Hybrid Millimeter-Wave Integrated Circuits," Tech. Dept. ECOM-74-0577-F, Contract DAAB07-74-C-0577, performed for the U.S. Army Electronics Command, Fort Monmouth, NJ, by ITT Research Institute, Chicago, IL, Oct. 1975.

3. R. Baets and P. E. Lagasse, "Calculation of Radiation Loss in Integrated-Optic Tapers and Y-Junctions," *Applied Optics*, vol. 21, no. 11, pp. 1972-1978, June 1982.

4. F. Schwering and A. A. Oliner, "Millimeter-Wave Antennas," in *Antenna Handbook*, Y. T. Lo and S. W. Lee, Eds. New York, NY: Van Nostrand Reinhold, 1988, ch. 17.

5. J. B. Andersen, *Metallic and Dielectric Antennas*. Lyngby: Polyteknisk Forlag, Technical University of Denmark, 1971.

6. J. R. James, "Engineering Approach to the Design of Tapered Dielectric-rod and Horn Antennas," *The Radio and Electronic Engineer*, vol. 42, no. 6, pp. 251-259, June 1972.

7. P. K. Tien, G. Smolinsky, and R. J. Martin, "Radiation Fields of a Tapered Film and a Novel Film-to-Fiber Coupler," *IEEE Trans. Microwave Theory Tech.*, vol. 23, no. 1, pp. 79-85, Jan. 1975.

8. E. Bahar, "Propagation of Radio Waves over Non-Uniform Layered Medium," *Radio Sci.*, vol. 5, no. 7, pp. 1069-1076, July 1970.

9. V. V. Shevchenko, *Continuous Transitions in Open Waveguides*. Boulder, CO: Golem Press, 1971.

10. D. Marcuse, *Theory of Dielectric Optical Waveguides*. San Diego, CA: Academic Press, 1974.

11. D. Marcuse, "Radiation Losses of Tapered Dielectric Slab Waveguides," *Bell Syst. Tech. J.*, vol. 49, no. 2, pp. 273-290, Feb. 1970.

12. D. Marcuse, *Light Transmission Optics*, 2nd ed. New York, NY: Van Nostrand Reinhold, 1982.

13. P. G. Suchoski, Jr. and V. Ramaswamy, "Exact Numerical Technique for the Analysis of Step Discontinuities and Tapers in Optical Dielectric Waveguides," *J. Opt. Soc. Amer. A*, vol. 3, no. 2, pp. 194-203, Feb. 1986.

14. T. E. Rozzi, "Rigorous Analysis of the Step Discontinuity in a Planar Dielectric Waveguide," *IEEE Trans. Microwave Theory Tech.*, vol. 26, no. 10, pp. 738-746, Oct. 1978.

15. K. Hirayama and M. Koshiba, "Analysis of Discontinuities in an Open Dielectric Slab Waveguide by Combination of Finite and Boundary Elements," *IEEE Trans. Microwave Theory Tech.*, vol. 37, no. 4, pp. 761-768, Apr. 1989.

16. K. Hirayama and M. Koshiba, "Numerical Analysis of Arbitrarily Shaped Discontinuities Between Planar Dielectric Waveguides with Different Thicknesses," *IEEE Trans. Microwave Theory Tech.*, vol. 38, no. 3, pp. 260-264, Mar. 1990.

17. G. H. Owyang, *Foundations of Optical Waveguides*. New York, NY: Elsevier Science, 1981.

18. T. Rozzi and M. Mongiardo, *Open Electromagnetic Waveguides*. London, United Kingdom: The Institution of Electrical Engineers, 1997.

19. R. E. Collin, *Field Theory of Guided Waves*, 2nd ed. New York, NY: IEEE Press, 1991.

20. F. Arndt, B. Koch, H. Orlok, and N. Schroder, "Field Theory Design of Rectangular Waveguide Broad-Wall Metal-Insert Slot Couplers for Millimeter-Wave Applications," *IEEE Trans. Microwave Theory Tech.*, vol. 33, no. 2, pp. 95-104, Feb. 1985.

21. T. Itoh, *Numerical Techniques for Microwave and Millimeter-Wave Passive Structures*. Singapore: Wiley, 1989, ch. 10.

22. G. F. Carrier, M. Krook, and C. E. Pearson, *Functions of a Complex Variable Theory and Technique*. Ithaca, NY: Hod Books, 1983.

23. W. C. Chew, *Waves and Fields in Inhomogeneous Media*. New York, NY: IEEE Press, 1995.

24. C. A. Balanis, *Antenna Theory Analysis and Design*, 2nd ed. New York: Wiley, 1997.

25. W. L. Stutzman and G. A. Thiele, *Antenna Theory and Design*, 2nd ed. New York, NY: Wiley, 1998.

26. P. Gelin, M. Petenzi, and J. Citerne, "New Rigorous Analysis of the Step Discontinuity in a Slab Dielectric Waveguide," *Electron. Lett.*, vol. 15, no. 12, pp. 355-356, June 1979.

27. A. Ittipiboon and M. Hamid, "Scattering of Surface Waves at a Slab Waveguide Discontinuity," *Proc. Inst. Elec. Eng.*, vol. 126, no. 9, pp. 798-804, Sept. 1979.

28. T. E. Rozzi and G. H. in't Veld, "Variational Treatment of the Diffraction at the Facet of d.h. Lasers and of Dielectric Millimeter Wave Antennas," *IEEE Trans. Microwave Theory Tech.*, vol. 28, no. 2, pp. 61-73, Feb. 1980.

29. P. Gelin, M. Petenzi, and J. Citerne, "Rigorous Analysis of the Scattering of Surface Waves in an Abruptly Ended Slab Dielectric Waveguide," *IEEE Trans. Microwave Theory Tech.*, vol. 29, no. 2, pp. 107-114, Feb. 1981.

30. P. Gelin, S. Toutain, and J. Citerne, "Scattering of Surface Waves on Transverse Discontinuities in Planar Dielectric Waveguides," *Radio Sci.*, vol. 16, no. 6, pp. 1161-1165, Nov.-Dec. 1981.

31. T. Hosono, T. Hinata, and A. Inoue, "Numerical Analysis of the Discontinuities in Slab Dielectric Waveguides," *Radio Sci.*, vol. 17, no. 1, pp. 75-83, Jan.-Feb. 1982.

32. K. Uchida and K. Aoki, "Scattering of Surface Waves on Transverse Discontinuities in Symmetrical Three-Layer Dielectric Waveguides," *IEEE Trans. Microwave Theory Tech.*, vol. 32, no. 1, pp. 11-19, Jan. 1984.

33. V. Ramaswamy and P. G. Suchoski, Jr., "Power Loss at a Step Discontinuity in an Asymmetrical Dielectric Slab Waveguide," *J. Opt. Soc. Amer. A*, vol. 1, no. 7, pp. 754-759, July 1984.

34. P. G. Suchoski, Jr., "Analysis of Step Discontinuities and Tapers in Optical, Dielectric Waveguides," M.S. thesis, University of Florida, 1985.

35. C. N. Capsalis, J. G. Fikioris, and N. K. Uzunoglu, "Scattering from an Abruptly Terminated Dielectric-Slab Waveguide," *J. Lightwave Technol.*, vol. 3, no. 2, pp. 408-415, Apr. 1985.

36. E. Nishimura, N. Morita, and N. Kumagai, "An Integral Equation Approach to Electromagnetic Scattering from Arbitrary Shaped Junctions Between Multilayered Dielectric Planar Waveguides," *J. Lightwave Technol.*, vol. 3, no. 4, pp. 887-894, Aug. 1985.

37. M. Koshiba and K. Hirayama, "Application of Finite-Element Method to Arbitrarily Shaped Discontinuities in a Dielectric Slab Waveguide," *Proc. IEE Pt. H*, vol. 135, no. 1, pp. 8-12, Feb. 1988.

38. S. Chung and C. H. Chen, "A Partial Variational Approach for Arbitrary Discontinuities in Planar Dielectric Waveguides," *IEEE Trans. Microwave Theory Tech.*, vol. 37, no. 1, pp. 208-214, Jan. 1989.

39. N. Morita, "A Rigorous Analytical Solution to Abrupt Dielectric Waveguide Discontinuities," *IEEE Trans. Microwave Theory Tech.*, vol. 39, no. 8, pp. 1272-1278, Aug. 1991.

40. K. Hirayama and M. Koshiba, "Analysis of Discontinuities in an Asymmetric Dielectric Slab Waveguide by Combination of Finite and Boundary Elements," *IEEE Trans. Microwave Theory Tech.*, vol. 40, no. 4, pp. 686-691, Apr. 1992.

41. C. S. Rocha, "Scattering of Surface Waves at Dielectric Slab Waveguide with Axial Ascending Discontinuity," *IEEE Trans. Magn.*, vol. 34, no. 5, pp. 2720-2723, Sept. 1998.

42. M. Oz and R. R. Krchnavek, "Power Loss Analysis at a Step Discontinuity of a Multimode Optical Waveguide," *J. Lightwave Technol.*, vol. 16, no. 12, pp. 2451-2457, Dec. 1998.

43. J. D. Kraus and R. J. Marhefka, *Antenna for All Applications*, 3rd ed. New York, NY: McGraw-Hill, 2002.

44. S. P. Schlesingor and A. Vigants, "HE_{11} Excited Dielectric Wave Surface Radiators," Techn. Report AFCRC-TN-59-573, Air Force Cambridge Research Center, June 1959.

45. V. C. Smits, "Rear Gain Control of a Dielectric Rod Antenna," *Microwave Journal*, pp. 65-67, Dec. 1968.

46. Y. Shiau, "Dielectric Rod Antennas for Millimeter-Wave Integrated Circuits," *IEEE Trans. Microwave Theory Tech.*, vol. 24, no. 11, pp. 869-872, Nov. 1976.

47. H. Hofmann and B. Rembold, "Dielektrische Antennan in mm-Wellen Bereich," in *Wiss. Ber. AEG-Telefunken 50*, 1977, pp. 73-75.

48. D. W. Brock and R. W. Major, "EHF Polyrod-Array Antenna," NOSC Techn. Report 1301, Dec. 1989.

49. S. Kobayashi, R. Mittra, and R. Lampe, "Dielectric Tapered-Rod Antennas for Millimeter-Wave Applications," *IEEE Trans. Antennas Propagat.*, vol. 30, no. 1, pp. 54-58, Jan. 1982.

50. G. M. Whitman, F. Schwering, W. Chen, A. Triolo, and J. Junnapart, "The Integrated Dielectric Slab Waveguide-Wedge Antenna," in *Directions for the Next Generation of MMIC Devices and Systems*, N. K. Das and H. L. Bertoni, Eds. New York: Plenum Press, 1997, pp. 181-195.

51. G. M. Whitman, C. Pinthong, A. A. Triolo, and F. Schwering, "An Approximate but Accurate Analysis of the Dielectric Wedge Antenna Fed by a Slab Waveguide Using the Local Mode Theory and Schelkunoff Equivalence Principle," *IEEE Trans. Antennas Propagat.*, accepted for publication on Mar. 2005.

52. F. J. Zucker, "Surface and Leaky-Wave Antennas," in *Antenna Engineering Handbook*, H. J. Jasik, Ed. New York: McGraw-Hill, 1961, ch. 16.

53. F. J. Zucker, "Surface-Wave Antennas and Surface-Wave-Excited Arrays," in *Antenna Engineering Handbook*, 2nd ed., R. C. Johnson and H. Jasik, Eds. New York: McGraw-Hill, 1984, ch. 12.

54. M. N. Sadiku, *Numerical Techniques in Electromagnetics*. Boca Raton, FL: CRC Press, 1992.

55. J. H. Mathews and K. D. Fink, *Numerical Methods Using Matlab*, 3rd ed. Upper Saddle River, NJ: Prentice-Hall, 1999.

56. A. D. Yaghjian and E. T. Kornhauser, "A Modal Analysis of the Dielectric Rod Antenna Excited by the HE_{11} Mode," *IEEE Trans. Antennas Propagat.*, vol. 20, no. 2, pp. 122-128, Mar. 1972.

57. S. Kobayashi, R. Lampe, R. Mittra, and S. Ray, "Dielectric Rod Leaky-Wave Antennas for Millimeter-Wave Applications," *IEEE Trans. Antennas Propagat.*, vol. 29, no. 5, pp. 822-825, Sept. 1981.

58. K. Mahdjoubi and C. Terret, "An Analysis of Piecewise Homogeneous Dielectric Rod Antenna," *IEEE Trans. Antennas Propagat.*, vol. 34, no. 4, pp. 598-601, Apr. 1986.

59. S. Chung and C. H. Chen, "Analysis of Irregularities in a Planar Dielectric Waveguide," *IEEE Trans. Microwave Theory Tech.*, vol. 36, no. 9, pp. 1352-1358, Sept. 1988.

60. S. Chung and C. H. Chen, "A Partial Variational Analysis of Planar Dielectric Antennas," *IEEE Trans. Antennas Propagat.*, vol. 39, no. 6, pp. 713-718, June 1991.